

# UC Berkeley

## UC Berkeley Electronic Theses and Dissertations

### Title

Vibration Harvesting using Electromagnetic Transduction

### Permalink

<https://escholarship.org/uc/item/0hg645mt>

### Author

Waterbury, Andrew

### Publication Date

2011

Peer reviewed|Thesis/dissertation

Vibration Harvesting using Electromagnetic Transduction

By

Andrew Cullen Waterbury

A dissertation submitted in partial satisfaction of the  
requirements for the degree of

Doctor of Philosophy

in

Engineering – Mechanical Engineering

in the

Graduate Division

of the

University of California, Berkeley

Committee in charge:

Professor Paul K. Wright, Chair  
Professor Dennis K. Lieu  
Professor Seth R. Sanders

Fall 2011

Vibration Harvesting using Electromagnetic Transduction

Copyright 2011

by

Andrew Cullen Waterbury

## Abstract

### Vibration Harvesting using Electromagnetic Transduction

By

Andrew Cullen Waterbury

Doctor of Philosophy in Engineering – Mechanical Engineering

University of California, Berkeley

Professor Paul K. Wright, Chair

Embedded condition monitoring sensors that eliminate unanticipated failures of critical or high value equipment improve asset utilization while streamlining maintenance and support operations. General Electric and Rolls Royce use embedded sensors on their jet engines that have eliminated failures and allowed maintenance to be performed on an as-needed basis. As a result, airplane utilization increases while enabling the consolidation of maintenance operations. In more traditional industrial settings, condition monitoring of manufacturing and industrial equipment can quickly impact bottom lines through improved productivity and streamlined operations in ways comparable to what is already being realized in the aviation industry.

Wireless sensor nodes provide embedded sensing with little overhead or infrastructure cost as long as appropriate power sources are available to sustain the node over its target lifetime. Energy is the limiting factor for sensor node lifetimes and data streams. Since most manufacturing and industrial equipment have some associated vibration spectrum when operating, transducing the mechanical energy of vibrations to a small amount of electrical energy electromagnetically was explored as a way of powering condition monitoring sensors.

Large pump motors and a machine tool were surveyed to characterize input vibration accelerations associated with manufacturing and industrial operations. Harvestable acceleration peaks occurred below 120 Hz and had magnitudes near or less than 0.1 g. Metal cutting vibrations were characterized and shown to have vibration frequencies proportional to the number of cutting teeth and the spindle RPM. It was also shown that, the 0.4-1.0 g acceleration impulses associated with the rapid axis motion of a machine tool are harvestable.

Simple magnet and coil as well as coreless electromagnetic architectures were pursued using an overall device size constrain of a cube with 2.5 cm sides. That device size was roughly the same as a c-cell battery that is capable of powering a wireless sensor node for five to ten years. The target power for the harvester designs was the time-averaged powers of hundreds of microwatts to single milliwatts required by commercial wireless sensor nodes. Prototype vibration harvesters based on magnet-coil and voice-coil transducer designs were fabricated and evaluated. Both were able to produce about a milliwatt on a vibration platform for an input acceleration amplitude of 0.1 g at



frequencies consistent with those characterized on the pump motors and machine tool. The power densities of the unoptimized proof of concept prototypes were comparable to commercial vibration harvester but at less than one seventh the size.

The voice-coil prototype was installed on several 15–30 kW pump motors running support systems for a microfabrication lab, and unrectified powers of 0.2–1.5 mW were harvested. Similarly, 0.8–1.8 mW was harvested from metal cutting vibrations while facemilling cast iron and stainless steel, showing that powers comparable to commercial sense node requirements could be harvested from industrial settings.

Coreless motor architectures proved to be best suited for industrial settings because the unconstrained magnetic flux of simple magnet-coil designs interacted with the iron and steel mounting surfaces commonly found on large machines. Simulated coreless magnetic circuit designs showed that gap magnetic flux densities approaching one tesla could be possible but were not implemented.

# Table of Contents

---

<b>Chapter 1. Introduction</b>	<b>2</b>
1.1. Motivation	2
1.2. Impact on engineering infrastructure	2
1.3. Wireless sensor nodes	3
1.3.1. Wireless sensor node: system integration	3
1.3.2. Mote energy requirements	3
1.4. Energy harvesting sources	5
1.4.1. Solar	5
1.4.2. Fluid flow	6
1.4.3. Temperature differences	6
1.4.4. Radio Frequencies	6
1.4.5. Vibrations	7
1.5. Vibration transduction	7
1.5.1. Vibration sources	7
1.5.2. Importance of resonant frequency and mass	8
1.5.3. Push for MEMS energy harvesting	9
1.5.4. Transduction mechanisms	9
1.5.4.1. Piezoelectric generators	9
1.5.4.2. Electrostatic generators	10
1.5.4.3. Electromagnetic generators	10
1.6. Electromagnetic systems	10
1.6.1. Relevant Maxwell's equations	11
1.6.2. Equivalent magnetic circuit parameters	11
1.6.2.1. Relationship between magnetic field intensity and magnetic flux density and the importance of permeability	11
1.6.2.2. Equivalent magnetic circuit analogs	12
1.6.2.3. Magnetic flux, $\phi$	12
1.6.2.4. Magnetomotive force, MMF	13
1.6.2.5. Reluctance, $R$	14
1.6.3. Voice-coil architectures	14
<b>Chapter 2. Literature Review</b>	<b>17</b>
2.1. Resonant frequency modification	17
2.2. Established electromagnetic vibration transducer designs	18
<b>Chapter 3. Generalized harvester model</b>	<b>21</b>
3.1. Determining a general equation of motion	21
3.2. Determining the voltage equation	22
3.2.1. Voltage source	22
3.2.2. Self-inductance	23
3.3. Full system of differential equations	24
<b>Chapter 4. Device designs</b>	<b>25</b>
4.1. Mechanical device design constraints	25
4.2. Resonant system	26
4.3. Prototyped designs	29

4.3.1. Open magnetic circuit (OMC)	29
4.3.1.1. General OMC design guide	29
4.3.1.2. OMC design case considerations, simplifications, and analysis for the prototype	31
4.3.1.3. Practical considerations for the prototype within the imposed 2.5 cm cube constraint	35
4.3.2. Voice-coil (VC)	36
4.3.2.1. General VC design guide	37
4.3.2.2. VC design case for the prototype	39
4.4. Additional design constraint: Voltage	41
4.5. Possible improved magnetic circuits	42
4.5.1. Coreless DC motor architecture	42
4.5.2. Halbach array architecture	43
<b>Chapter 5. Device characterization</b>	<b>46</b>
5.1. Vibration platform	46
5.2. Prototype parameters	47
5.2.1. Resonant springs	47
5.2.2. Open magnetic circuit (OMC) prototype	47
5.2.3. Voice-coil (VC) prototype	48
5.3. Vibration platform evaluation of prototypes	49
5.3.1. OMC evaluation	50
5.3.2. VC evaluation	54
5.3.3. Summary of experimental characterization of prototypes	56
<b>Chapter 6. Applications to asset monitoring</b>	<b>58</b>
6.1. Large industrial motor deployment	58
6.1.1. Motor vibration harvesting survey	59
6.1.2. Motor vibration harvesting results	63
6.1.3. Experimental prediction of failure	65
6.2. Machine tool deployment	65
6.2.1. Harvesting metal cutting vibrations	66
6.2.1.1. Facemilling vibrations and harvesting results from cutting cast iron	67
6.2.1.2. Facemilling vibrations and harvesting results from cutting stainless steel	69
6.2.1.3. Facemilling vibrations survey for cutting 6061-T6 aluminum	71
6.2.1.4. Summary of metal cutting vibration harvesting	71
6.2.2. Harvesting machine tool rapid axis motion	72
6.3. Simulated vehicle suspension deployment	76
<b>Chapter 7. Design discussion and future outlook</b>	<b>80</b>
<b>Chapter 8. Conclusions</b>	<b>82</b>
<b>Appendix A. Electromagnetics</b>	<b>85</b>
A.1. Maxwell's equations	85
<b>Appendix B. Cored vibration harvester designs</b>	<b>87</b>
<b>References</b>	<b>92</b>

# Acknowledgements

---

I am indebted to a great number of people for their aid over the course of my graduate studies. I would like to thank my advisor, professor Paul Wright, for accepting me into his research group and watching over me the last five years. I would also like to thank professors Seth Sanders and Dennis Lieu for their help answering my research questions and agreeing to be members of my thesis committee.

I would also like to thank all my labmates over these many years for their help, guidance, and revelry. I won't attempt to name them all for fear of leaving one out.

I am very appreciative of all the help and hard work of the four undergraduate research helpers, Brian Mahlstedt, Mikhail Podust, Doug Fabini, and Spencer Lin, who contributed to my project. I must give a special thanks to Spencer for his efforts in creating a comprehensive vibration testing platform control system.

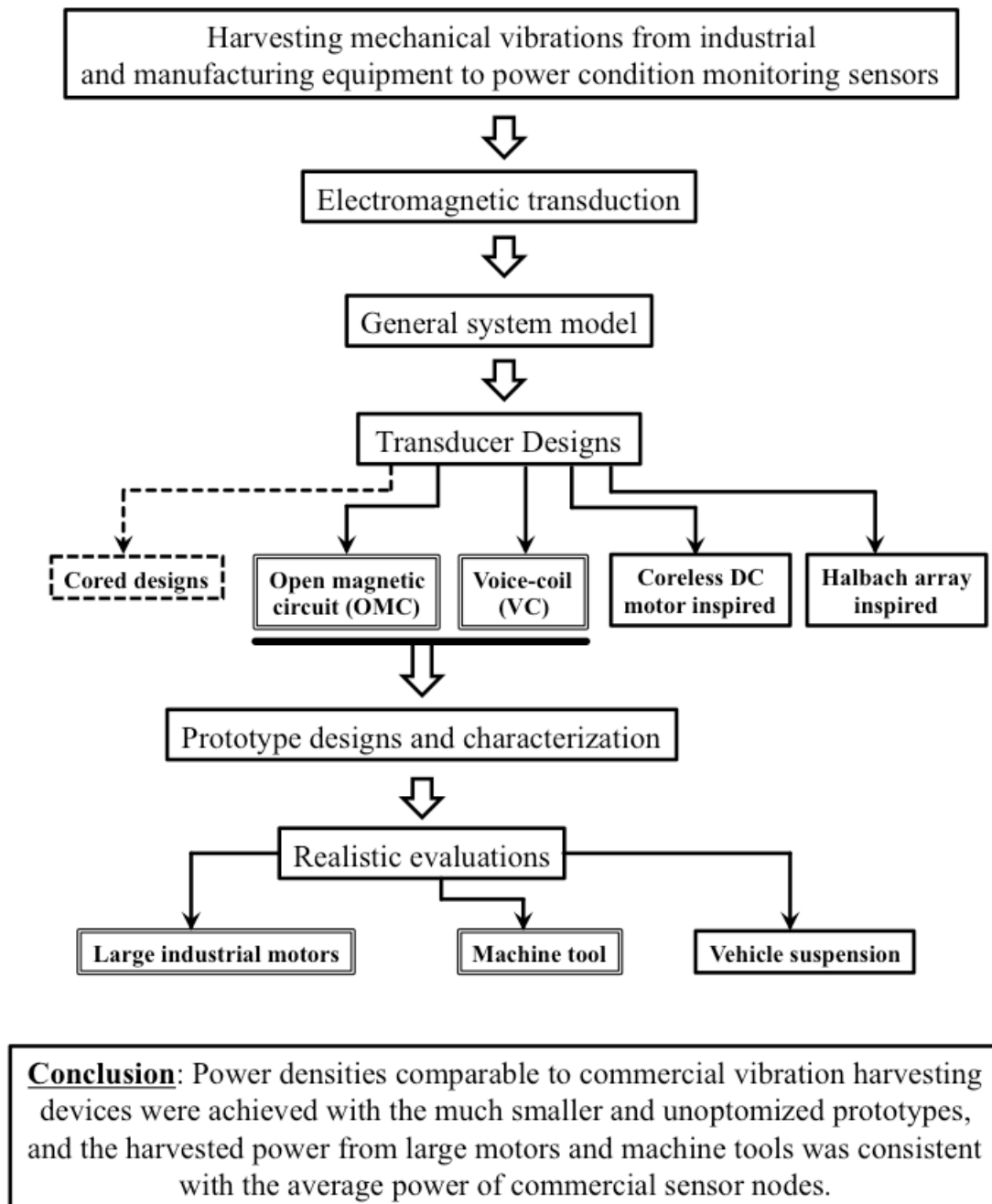
Finally, I would like to thank my parents, Dr. John Waterbury and Vicky Cullen, and brother, Matt Waterbury, for supporting me throughout.

# Nomenclature

---

$A$	Area normal to a magnetic flux path
$B$	Magnetic flux density
$B_r$	Remnant magnetization
$BEMF$	Back electromotive force
$D$	Electric flux density
$d$	Damping coefficient
$\delta$	Displacement
$E$ (electrical)	Electric field intensity
$E$ (mechanical)	Young's modulus
$F$	Force
$G$	Shear modulus
$g$	Gap distance
$H$ (magnetic)	Magnetic field intensity
$H$ (mechanical)	Height
$I_x$	Moment of inertia
$i$	Current
$J$ (electrical/magnetic)	Current density
$J$ (mechanical)	Torsion constant
$k$	Stiffness
$L$ (magnetic)	Inductance
$L$ (mechanical)	Length
$l, l_w$	conductor or length in a magnetic field
$l_{xxx}$	Flux path length through material xxx
$M$	Moment
$MMF$	Magnetomotive force
$m$	Mass
$\mu$	Permeability
$\mu_0$	Permeability of free space
$\mu_r$	Relative permeability
$N$	Number of coil turns
$\omega_0$	Resonant frequency
$\omega_y$	Base input frequency
$p$	Center platform side length
$\varphi$	Magnetic flux
$\phi_0$	Rotation on guided end of a beam
$Q$	Amplification factor
$R$ (electrical)	Resistance
$R$ (magnetic)	Reluctance
$r$	Radius
$\rho$	Charge density
$T$	Torque
$t$	time
$t$ (mechanical)	thickness
$\theta_0$	Tilt on guided end of a beam

$U$	Torsional strain energy
$V$	Voltage
$v$	Velocity
$w$	Width
$x$	X-axis coordinate
$\xi$	Mechanical strain
$Y$	Base motion amplitude
$y$	Y-axis coordinate
$y_w$	Y-axis coordinate position of a coil turn
$z$	Z-axis coordinate
$\zeta$	Damping ratio



# Chapter 1. Introduction

---

## 1.1. Motivation

The impetus for this research was to explore and evaluate the designs of electromagnetic transducers specifically intended to harvest mechanical vibrations by converting the mechanical energy of vibrations to small amounts of electrical energy as a means of enabling ubiquitous long lasting wireless sensor nodes. The results of this research include vibration harvester design considerations at a high level and at the detailed mechanical level, evaluation of prototype designs, and realistic proof of concept deployments for enabling wireless condition monitoring sensors. The target applications that drove this work centered around industrial equipment and asset monitoring where there was the potential for high added value from a wireless sensor assessing the health of a system. The added value of a condition monitoring sensor includes performing maintenance only as needed, eliminating unscheduled down time, and the associated improved productivity, but wireless sensors also add value by lowering the cost of additional or retrofitted sensing. Wireless sensors eliminate the burdensome and often prohibitive overhead costs of running wires to sensor locations, but in order to be viable, wireless sensors should be self-sustaining for decades, placing stringent demands on power sources for a sensor node. Replacing batteries periodically becomes untenable as the number of sensors becomes large, and batteries don't have the shelf life and power capacity to last decades while remaining a reasonable physical size. Thus, harvesting a small amount of energy from the environment surrounding the sensor to continuously charge a small battery or capacitor becomes an enabling technology for wireless sensors with long lifetimes.

## 1.2. Impact on engineering infrastructure

Embedded sensors that continuously monitor and predict the need for maintenance of critical equipment have the potential to add tremendous value to not only equipment users but also equipment suppliers. Condition monitoring sensors with low infrastructure and overhead costs can quickly impact bottom lines through improved productivity and the streamlining of supply chains by eliminating unanticipated failures.

General Electric and Rolls Royce use embedded sensors on their jet engines to predict failure and only perform maintenance when necessary [1][2]. This not only minimizes the amount of time spent maintaining planes but also allows airlines to perform upkeep and repairs at only a few allocated airports. Thus, simple sensors can have a cascading impact on an entire industry.

Small scale energy harvesting, like the harvesting of mechanical vibrations as addressed by this work, is an enabling technology for long lasting embedded wireless sensors that have small capital cost and require almost no infrastructure. Harvesting vibrational energy from high value industrial and manufacturing equipment in conjunction with other small scale energy sources to power condition monitoring sensors



has the potential to improve productivity and impact manufacturing operations in ways that are already being realized by the aviation industry.

### 1.3. Wireless sensor nodes

#### 1.3.1. Wireless sensor node: system integration

Wireless sensor nodes or motes are a combination of sensing, power, and integrated circuitry [3][4][5]. The integrated circuits encompass data storage, computation, communication, and power management. Though most wireless nodes communicate with the outside world through a radio transmitter and receiver, optical communication has also been demonstrated [6]. The typical power source is a battery, but nodes powered by energy harvesting in conjunction with a battery have been created [4] [7]. Figure 1.1 shows the major components of a mote (wireless sensor node) that has energy harvesting as a power source.

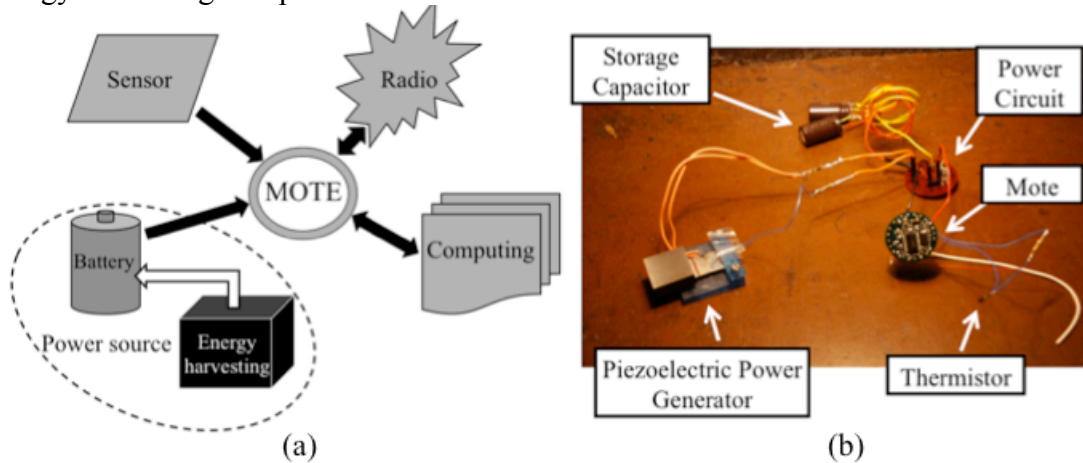


**Figure 1.1.** (a) Block diagram of the major component of a wireless sensor node also know as a mote. (b) Previous work in authors laboratory showing the integration of radio, computing, harvesting, storage, and temperature sensors. The mote is a Crossbow.

The research presented in this work focuses on an energy harvesting technology aimed at powering stand-alone motes for decades. Before considering the energy harvesting technology, the power requirements of the sensor, radio, and computing that make up the mote need to be understood so that the designer of the energy harvester knows the benchmarks that define a viable harvesting system.

#### 1.3.2. Mote energy requirements

Beyond a sensor, the major components determining the energy requirements of a mote are a microprocessor, data storage, and a radio. To explore and define energy use, a commercially available Dust Networks Smartmesh DN6000/M600x mote-on-chip wireless node will be used as a reference for typical power levels within the industry [8]. Generally, the component of a wireless sensor node with the greatest power draw is the radio. The Dust node operates in the 2.4GHz RF band. The radio power use when transmitting is about 31 mW, but the peak operating power for the node of 108 mW

occurs if it's transmitting, writing to flash memory, and the microprocessor is fully utilized. Further power state numbers are shown in table 1.1. The transmitting and peak node powers provide benchmark power requirements for any energy harvester or power source to keep the node fully operational at all times. However, sensor applications almost never need continuous data streams. This is especially true for condition monitoring applications. If continuous data isn't necessary the wireless sensor node can be duty cycled, or turned on and off on some schedule, to save power.

The duty cycle is typically determined by a power and lifetime constraint or a data interval requirement from the application, but in either case, the duty cycling lowers the time averaged power required by the node. Since it is impractical both from power and size perspectives to install large harvesters in industrial settings that could service the peak power of the node, the time averaged power sets the power target for energy harvesting. While typical duty cycles are 1% or less [5], nodes and data streams are constrained by power [9], so providing a time averaged power that is roughly 1% of the standard peak power draw for the node becomes the benchmark for energy harvesting. Providing greater power than that allows the flexibility of higher data flows or extended node lifetime.

**Table 1.1.** Power states and magnitudes for a Dust Networks Smartmesh DN6000/M600x mote-on-chip. Supply voltage is typically 3.6V [8].

State or function	Power [mW]
Peak operating power: System operating at 14.7MHz, Radio TX, and flash write	108
Doze: RAM on, data and state retained, reference clock active	0.0043
Radio TX, transmit	31.3
Radio RX, receive	12.6
Active: peripherals off, system operating at 7.37MHz	12.6
Flash write	10.8

For the condition monitoring applications driving this work, a typical sensor would be a MEMS accelerometer with reasonable sensitivity and a 1 kHz bandwidth or greater. An example is an STMicroelectronics LIS3L02AS4, which needs about 2.8 mW of power [10]. Including the accelerometer, the absolute maximum power draw for the Dust chip would be about 111 mW, but its typical peak power draw is likely closer to the level associated with being active and transmitting. In that case, the peak power would be about 44 mW. In either case, this provides a target time-averaged power range for a harvester of 0.44-1.11 mW, assuming a 1% duty cycle. So, independent of sensor the node manufacturer, *harvesters should approach generated powers of hundreds of microwatts or several milliwatts to allow duty cycles as high as 1% for wireless nodes that are currently available.*

A more detailed look at what determines a duty cycle and the state of the sensor node is worth exploring because an active node may not be near the peak power use values chosen to define the benchmark power range for a harvester, depending on the application. For condition monitoring, the node may only transmit information when the sensor has detected certain conditions, so without regular transmissions, the time

averaged power could be significantly lower. Figure 1.2 is a rough illustration of a possible active-events sequence for a sensor node after waking up from its low power doze state.

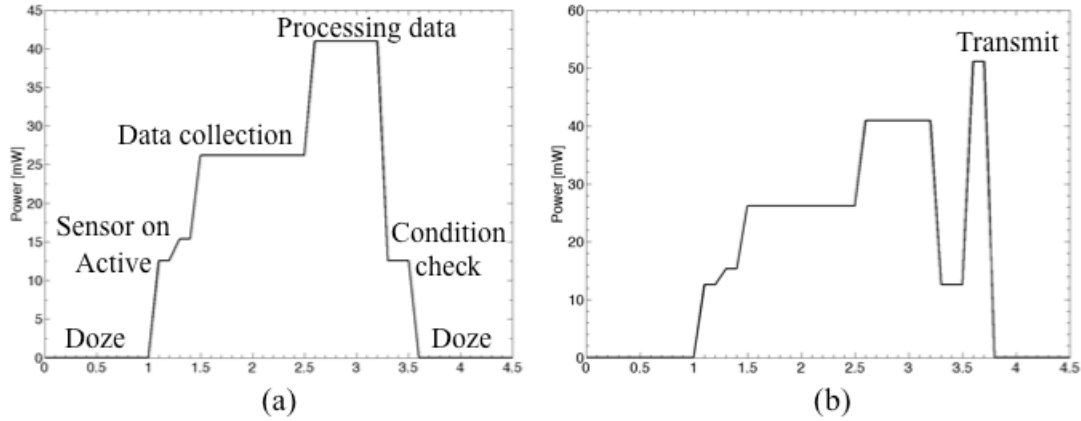


**Figure 1.2.** Illustration of a condition monitoring active sequence for a sensor node. (a) Condition not met, and (b) condition met and necessary action gets transmitted.

The roughly 0.4-1 mW target time average power for a harvester for commercial wireless sensors is high compared to what has been achieved in research settings where time averaged powers of microwatts have been demonstrated [7]. While node power consumptions continue to decrease even though sensor node performance shows a trend similar to Moore's law [11], energy continues to be the most valuable resource for a sensor node and network [12], making energy harvesting technologies a critical component to realizing ubiquitous long lasting wireless sensors.

## 1.4. Energy harvesting sources

Energy can be harvested from a wide variety of sources at all manner of scales. Solar and wind are capable of providing power grid scale harvested energy, but for wireless sensor nodes, only a small amount of power on the order of microwatts to milliwatts is needed to sustain a node. Thus, smaller scale sources of harvestable energy such as temperature differences, radio waves, and mechanical vibrations can also be considered for deriving the small amount of useful electrical energy required by wireless sensors.

### 1.4.1. Solar

There are two well established ways of converting light to electrical energy on a large scale. Solar thermal processes concentrate the radiation from the sun to heat a working fluid that is used to drive a traditional generator like a gas turbine. Alternatively, the energy of a photon can be used to elevate the energy state of an electron in a semiconductor material from the valance electron band to the conduction band allowing current flow [13]. The energy from photons enabling current flow in semiconductor materials is the operating principle behind photovoltaic cells. While solar thermal energy production is not well suited for small scale energy harvesting because concentrating a

large area of solar radiation is necessary, photovoltaic cells have been used on a small scale to power calculators from indoor lighting and as a source of harvested energy for wireless sensor nodes [4][14]. However light sources both indoors and outdoors are only available about 50% of the time. Furthermore, with the growing societal commitment to energy efficiency and savings, unnecessary indoor lighting is being turned off. As a result, harvestable light sources for powering wireless sensors may be scarce in industrial and factory settings.

#### 1.4.2. Fluid flow

At large scales, windmills and waterwheels have been used for centuries. Airflow energy harvesting has become universal, and large wind turbines convert the kinetic energy of wind into electrical energy for the power grid all around the world. Smaller scale harvesting from HVAC ducts and similarly sized flows has been explored as a way to power building health and control system wireless sensors. These small scale flow harvesters could use traditional turbine architectures [15][16], piezoelectric turbines [17], and von Kármán vortex street effects from blunt objects [18]. While good performance has been demonstrated, the applications are limited to ductwork or environments where flow rates greater than  $2 \text{ ms}^{-1}$  are found.

#### 1.4.3. Temperature differences

Temperature differences from waste heat sources can also be exploited to harvest relatively small amounts of energy. The Seebeck effect, which causes a voltage to arise due a temperature difference across a material in conjunction with a Peltier element, can be used to directly convert a temperature difference into electricity. The performance and electrical output is proportional to the temperature difference that can be maintained across a thermoelectric device. In recent years, a large amount of research has focused on new nanoscale thermoelectric materials [19], and sensor nodes have been powered by thermoelectric generators [20][21]. While the performance of new thermoelectric materials and thermoelectric generator designs is promising, practical designs still require temperature differences of  $5\text{--}10^\circ\text{C}$  to be viable.

#### 1.4.4. Radio Frequencies

Harvesting stray radio frequency energy, especially in dense urban areas where there are signals from cell phone networks, TV transmitters, and satellites, has gained some traction. Generally, a broadband approach where a large part of the frequency spectrum is harvested may yield significant energy, but narrow band harvesting has been shown to work for certain situations [22][23]. The broadband approach is necessary for a more general solution because the power in the RF signals corresponds to the far-field Friis transmission equation, where the power in the signal is inversely proportional to the square of the distance from the source. A wireless sensor node powered from stray RF signals in urban areas with a broadband approach has been developed [24].

RF power transmission is a similar concept that has been commercialized by companies like WiTricity where coupled resonant high Q inductive coils transfer power

at efficiencies as high as 95% over short distances on the order of a meter. This type of RF power transmission is not energy harvesting as much as it is inductive charging, but it could be applicable for periodically charging a sensor node that cannot exploit other power sources. One such system used this technique to power a system intended to be implanted in a person's brain. The node could be periodically charged through the skull inductively [25]. RF power transfer has limited applications for powering ubiquitous wireless sensors, and harvesting stray RF signals may only be applicable to extremely low power applications unless the deployment environment allows for a very large antenna.

#### 1.4.5. Vibrations

While solar, fluid flow, thermal, and RF harvesting are all capable of powering wireless sensors, the source of interest for this research is mechanical vibrations, particularly those associated with industrial equipment like large pumps and machine tools. Mechanical vibrations can be converted to electrical energy through an inertial transducer where the transduction mechanism is typically electromagnetic, piezoelectric, or electrostatic. Using vibrations as a source of energy for wireless sensors was originally investigated by Williams et al. [26] and expanded on by Roundy [27], and commercial vibration harvesters are available from Perpetuum and Ferro-Solutions. While vibrations have been shown to be viable sources of energy for wireless sensors, low power densities, among other issues, continue to limit the potential impact of the technology in furthering the vision of pervasive wireless sensor systems.

There is no one energy harvesting answer for powering wireless sensors. The best harvesting solution depends on the environment where the system will be deployed and the power requirements of the sensor application. Ultimately, a hybrid approach that incorporates several energy harvesting sources to power a sensor node may make the most sense. Industrial settings with large electrical motors and fabrication operations such as metal cutting are environments saturated with low level vibration sources and that have equipment or processes that could benefit from condition monitoring. Further investigation into characterizing industrial vibration sources is needed, as well as appropriate vibration harvester designs.

### 1.5. Vibration transduction

#### 1.5.1. Vibration sources

Low level ambient vibrations can be found throughout the world. Appliances and building structures have been considered as possible sources for vibration harvesting [27], and vibrations from body motion [28], aeronautical systems [29], and vehicle traffic [30], among many others, have been explored. Vibrations from industrial and manufacturing settings are of the greatest interest for condition and process monitoring applications. Table 1.2 contains basic characterizations of vibration sources that this author has measured in industrial and manufacturing settings (see chapter six), and it serves as a benchmark for realistic inputs for vibration transducers.

**Table 1.2.** Industrial and manufacturing vibrations

Source	Frequency [Hz]	Acceleration [g's]
<b>Large pump motors</b>		
30 kW motor	30	0.08
30 kW motor	60	0.06
15 kW motor	50	0.17
15 kW motor	120	0.06
<b>Haas VF-0 15kW machine tool</b>		
Facemilling cast iron	108	0.08
Facemilling stainless steel	116	0.06
Facemilling aluminum	489	0.06
Rapid-stop motion	Impulse	0.4-1.0

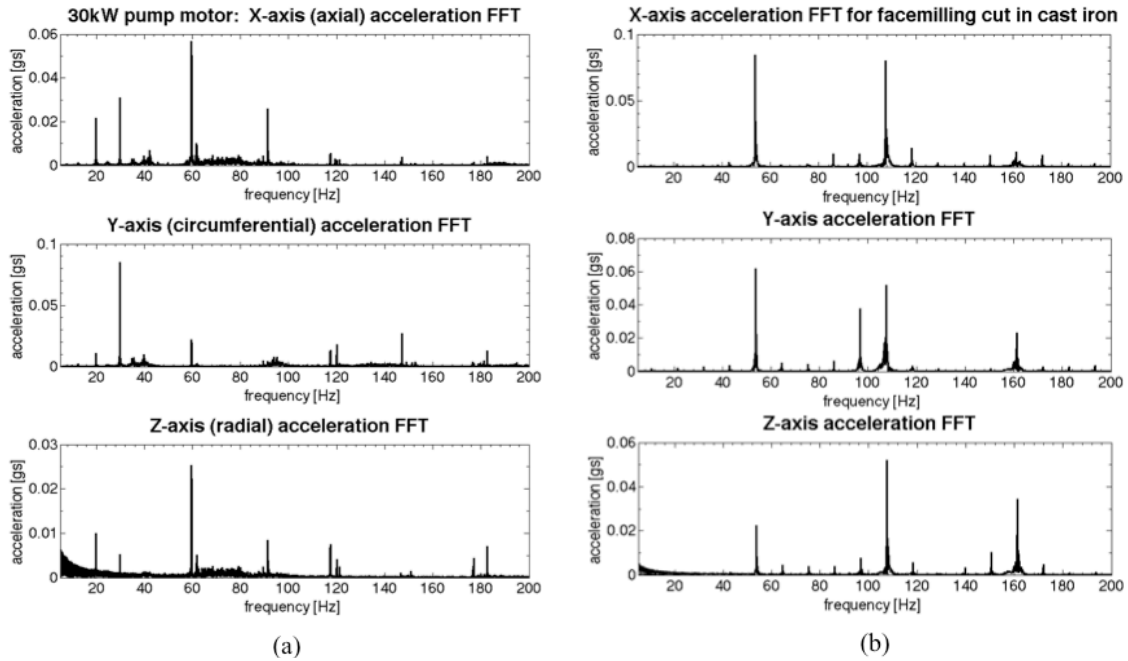


**Figure 1.3.** Acceleration frequency spectra for (a) a 30 kW water pump motor, and (b) vibration accelerations from facemilling gray cast iron on a Haas machine tool. For (b), the axes correspond to the axes of the machine tool.

As seen in table 1.2 and figure 1.3, the input acceleration magnitudes are very small and almost always below 0.2 g for continuous vibrations.

### 1.5.2. Importance of resonant frequency and mass

Vibration transduction is accomplished with an inertial device that can be modeled as a mass, spring, and damper system for a linear device [26]. The inertial structure is needed to produce some relative motion to drive the transduction mechanism. For a linear inertial device with sinusoidal base excitation, the maximum relative motion between the mass and base occurs when the frequency of the base excitation equals the

resonant frequency of the device. Thus, the first concern for practical vibration harvesting requires that the resonant frequency of the transducer match the vibration frequency because inertial structures typically have narrow bandwidths of a few hertz. Even a slight mismatch of 5Hz between the resonant frequency and the vibration frequency results in severely limited or no relative motion [26][31].

The small input acceleration magnitudes presented in the previous section require that the functional or inertial mass of the transducer be reasonably large because, fundamentally, the power in the transducer is the inertial mass multiplied by the input acceleration multiplied by the relative velocity of the functional mass. Thus, the electrical power extracted by the transducer will always be proportional to the moving mass of the device.

### 1.5.3. Push for MEMS energy harvesting

Microelectromechanical systems (MEMS) are small devices with feature sizes or length scales measured in micrometers, and they are usually created using semiconductor fabrication techniques. The largest overall size MEMS devices are typically about a square centimeter. The small size of MEMS harvesters limits their potential power generation capabilities, making it difficult to generate microwatt level power for the low input accelerations of typical vibration sources. The most compelling argument for MEMS devices is driving device costs lower with economy of scale arguments similar to those of the integrated circuit industry, but vibration harvesting is difficult to extrapolate to the millions or tens of millions of devices sold annually to achieve those cost savings. Because the harvester frequency must match the vibration frequency, it is difficult to find a universal vibration source that would allow fabrication of millions of devices with the same geometry.

### 1.5.4. Transduction mechanisms

#### *1.5.4.1. Piezoelectric generators*

Piezoelectric materials have crystal structures that change their electric polarization when subjected to a mechanical strain. The same effect causes a mechanical strain if the material is subjected to an appropriate electric field. The piezoelectric phenomenon can be exploited in a vibration harvester by using the movement of an inertial mass to strain a piezoelectric material that is often incorporated into the spring structure of the transducer. That strain induces a voltage that can be used to drive an external electrical load.

The potential of piezoelectric transduction of vibrations was demonstrated for centimeter scale devices by Roundy in [27], but the complication with piezoelectric materials is that those with high piezoelectric coefficients that efficiently convert strain to voltage, such as lead zirconate titanate (PZT) and aluminum nitride, tend to be brittle. Since vibration harvesters are resonant devices with desired lifetimes of decades, piezoelectric-based harvesters are in a fundamental sense caught in a trade-off between generated power and fatigue life. Higher stresses generate high power output, but the higher stress results in a short fatigue life.

#### *1.5.4.2. Electrostatic generators*

Electrostatic generators are variable capacitor structures where the capacitance is modified by the motion of the inertial mass. There are two classes of electrostatic generators: constant voltage and constant charge. The energy conversion processes for both classes are derived in [32]. In the constant voltage case, the variable capacitor is charged to a peak voltage when the capacitance is at its maximum value. That peak voltage is then maintained as the movement of the inertial mass lowers the capacitance. At the minimum capacitance, the remaining charge is siphoned off. Extra energy is created as a result of the mechanical work associated with lowering the capacitance. The capacitance is returned to its maximum value before the cycle restarts. In the constant charge case, the capacitance is modified from its maximum to minimum value by the movement of the inertial mass while the capacitor is at a peak charge. At the minimum capacitance value, the charge gets siphoned off, and the mechanical work associated with widening the gap between the capacitor plates generates extra electrical energy.

To avoid needing very large bias voltages, very small gaps between capacitor plates is necessary, but higher bias voltages are always desirable because the energy in a capacitive system is proportional to the square of the voltage. The small gaps generally lead to MEMS structures that limit the size of the inertial mass. Electrostatic vibration harvesters with overall length scales ranging from several centimeters and above [33][34] to millimeters and below [35][32] have demonstrated the ability to generate small amounts of power. Recent results from [36] are promising in terms of power and achieving a low resonant frequency for a MEMS device. The effectiveness of electrostatic generators is limited by the desire for large bias voltages in conjunction with small gaps in the capacitor structure and the complexity of the power management circuitry.

#### *1.5.4.3. Electromagnetic generators*

Electromagnetic generators operate according to Faraday's law, which describes voltage arising due to a time varying magnetic flux. In more practical terms, a voltage arises in a conductor when it is exposed to a time varying magnetic field or there is some relative velocity between the conductor and the magnetic field acting on it. Energy harvesters use permanent magnets to create the necessary magnetic fields because magnetic fields created with coils and seed currents would require inputting electrical energy, which is the most precious resource for sensor nodes and small scale energy harvesters. Even though harvesters that require power to generate power can work, such systems would be challenging and complex at the scale appropriate for vibration harvesting.

## **1.6. Electromagnetic systems**

This section introduces the equations, concepts, and principles associated with practical electromagnetic devices. The focus is tailored toward permanent magnet linear motors or generators. The aim is to provide enough knowledge for a reader to understand magnetic equivalent circuits, as well as the magnetic forces and induced voltages and



currents associated with generator designs. For more complete discussions and derivations, refer to resources such as [37][38].

### 1.6.1. Relevant Maxwell's equations

For magnetic devices where there is no external electric field, the integral form of the set of relevant Maxwell's equations is made up of Ampere's law, Gauss' law for magnetism, and Faraday's law. Respectively, the equations are

$$\oint_c \vec{H} \cdot d\vec{l} = \int_s \vec{J} \cdot d\vec{a}, \quad (1.1)$$

$$\oint_s \vec{B} \cdot d\vec{a} = 0, \quad (1.2)$$

$$\oint_c \vec{E} \cdot d\vec{l} = -\frac{\partial}{\partial t} \int_s \vec{B} \cdot d\vec{a}, \quad (1.3)$$

where  $\mathbf{H}$  is the magnetic field intensity,  $\mathbf{J}$  is the current density,  $c$  is the loop enclosing surface  $s$ ,  $\mathbf{B}$  is the magnetic flux density, and  $\mathbf{E}$  is the electric field intensity. Refer to Appendix A for the derivation of equations 1.1–1.3 from the full set of Maxwell's equations.

The integral form of Ampere's law, equation 1.1, essentially relates the magnetic field intensity to the current in a conductor enclosed by the bounding loops and areas that are generally well defined for practical situations. Gauss' law for magnetism, equation 1.2, in practical terms means that magnetic flux is conserved, or, in other words, that the flux entering a bounding volume must equal the flux leaving that volume [38]. Thus, Gauss' law applied to magnetic circuits is analogous to Kirchhoff's current law for electrical circuits. Faraday's law, equation 1.3, is particularly interesting because it determines the voltage developed by a charge in a time varying magnetic field and/or a charge moving in a magnetic field [37]. Since wires normally carry electrical charges, the left-hand side of equation 1.3 simplifies because the direction of the electric field is the axis of the wire, and the path, vector  $d\vec{l}$ , is along the wire. Thus the left-hand side of equation 1.3 becomes voltage. The right-hand side of equation 1.3 is simplified for most situations because the enclosed surface is designed to be normal to the direction of magnetic flux [38]. The result is the elimination of the integral on the right-hand side. Hence, the practical form of Faraday's law is

$$V = -\frac{\partial}{\partial t} \int_s \vec{B} \cdot d\vec{a} = -\frac{\partial B}{\partial t} A = -\frac{\partial \phi}{\partial t}, \quad (1.4)$$

where  $\phi$  is the enclosed magnetic flux and  $A$  is the area of the enclosed surface, generally the area normal to the magnetic flux path.

### 1.6.2. Equivalent magnetic circuit parameters

#### 1.6.2.1. Relationship between magnetic field intensity and magnetic flux density and the importance of permeability

Before introducing equivalent magnetic circuit parameters, the constitutive relationship between magnetic flux density,  $\mathbf{B}$ , and magnetic field intensity,  $\mathbf{H}$ , as well as

the influence of material properties must be introduced. Magnetic field intensity and magnetic flux density are related by

$$\vec{B} = \mu_0 \mu_r \vec{H} = \mu \vec{H}, \quad (1.5)$$

where  $\mu_0$  is the permeability of free space,  $\mu_r$  is the relative permeability of a material, and  $\mu$  is the permeability of a material. The simple relationship in equation 1.10 reveals the importance of material permeability. Generally, large magnitude flux densities are desirable for engineering purposes, so high permeability materials are desirable. Ferromagnetic materials, such as iron, cobalt, and nickel, are common in magnetic devices because a higher permeability material conducts magnetic flux much more efficiently. The low carbon steels, AISI 1010 or 1018, that were used in the designs for this research generally have a permeability that is two or three orders of magnitude higher than that of air below the saturation point of the material. As the magnetic flux density in a ferromagnetic material increases, the permeability of the material decreases, and eventually a high enough magnetic flux density will saturate the material, meaning its permeability is essentially that of air. For the low carbon steels used in this work, saturation generally occurs between one and two Tesla, the SI unit of magnetic flux density [37]. Equivalent magnetic circuit analysis is only accurate when the system being analyzed has no saturation because linear or constant permeability is assumed for all the materials.

#### 1.6.2.2. Equivalent magnetic circuit analogs

Equivalent magnetic circuits are analogous to simple electrical circuits with only resistances and voltage or current sources. The table below summarizes the analogs between electrical and magnetic systems.

Electrical	Voltage	Current	Resistance
Magnetic	MMF, magnetomotive force	Flux, $\phi$	Reluctance

**Table 1.3.** Analogs between simple electrical and equivalent magnetic circuits.

#### 1.6.2.3. Magnetic flux, $\phi$

With a sufficient magnetic field, there will be an associated flux. Assuming there is a uniform magnetic field through a material, the flux is

$$\phi = BA, \quad (1.6)$$

where A is the cross-sectional area of the flux carrying material.

Before continuing further with interpretations and representations of equivalent magnetic circuit systems, it is worth noting that there are two sources of magnetic flux, and thereby two sources of magnetic flux density, B, and magnetic intensity, H. The two sources are coils carrying a current and permanent magnetic material. Ampere's law describes these two sources of magnetic fields. A current carrying conductor develops a corresponding magnetic field intensity, and a permanent magnetic material has a magnetic field intensity associated with it even though no current is present. The magnetic intensity for each flux source determines the associated magnetomotive force.

#### 1.6.2.4. Magnetomotive force, MMF

To better understand the sources of magnetomotive force, consider the two simple magnetic circuits in figure 1.4 where steel is the high permeability material defining the magnetic flux path.

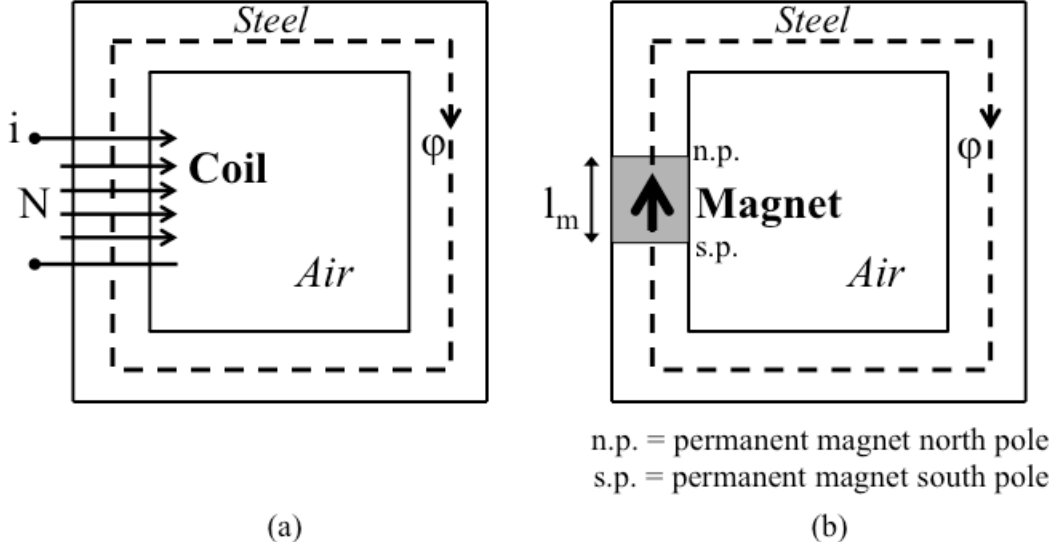


**Figure 1.4.** Simple magnetic circuits with (a) a coil and (b) a permanent magnet as the source of magnetic flux, illustrating the derivation of magnetomotive force for each case.

The current in the  $N$ -turn coil creates a magnetic intensity in the steel. Also, due to the high permeability of the steel compared to the surrounding air, there is a large flux density in the steel, causing flux to flow. The magnetomotive force for the coil comes from Ampere's law as

$$MMF = \oint_c \vec{H} \cdot d\vec{l} = i_{enclosed} = Ni, \quad (1.7)$$

where the contour loop and surface for the integrals is basically defined by the dashed flux loop in figure 1.4(a). For the permanent magnet circuit depicted in figure 1.4(b), it is not quite as straightforward as the coil situation since there is no current present and the magnet and steel have different material properties. Ampere's law then gives

$$0 = \oint_c \vec{H} \cdot d\vec{l} = H_m l_m + H_s l_s, \quad (1.8)$$

where  $l_m$  and  $l_s$  are the length of the path through the magnet and steel, respectively. Since the magnet is the source of magnetomotive force, the  $H_m l_m$  term defines that MMF, so determining the value of  $H_m$  is the next step. Using equation 1.5, the MMF for the magnet can be calculated using the remnant magnetization,  $B_r$ , and the permeability of the magnet. So an ideal permanent magnet MMF source is described by

$$MMF = H_m l_m = \frac{B_r}{\mu} l_m. \quad (1.9)$$

Unlike the coil circuit in figure 1.4, where the flux path is a continuous piece of steel, the permanent magnet circuit has a flux path through the magnet and steel, so there is a change in material properties and a possible associated loss. The loss arises because most magnets have a low permeability that is equivalent to air or free space. Thus, in

permanent magnet circuits, the magnet essentially looks like an air gap. The losses in magnetic circuits are referred to as reluctances.

#### 1.6.2.5. Reluctance, $R$

Reluctances capture the loss along a flux path due to geometry and material properties. Assuming that the magnetic field is uniform through the material along the flux path, reluctance terms have the form

$$R = \frac{l}{\mu A}, \quad (1.10)$$

where  $l$  is the length of the flux path through the material or section of interest,  $A$  is the cross-sectional area of the flux path, and  $\mu$  is the permeability of the material carrying the magnetic flux. Having been defined, the equivalent circuits to those shown in figure 1.4 can be generated.

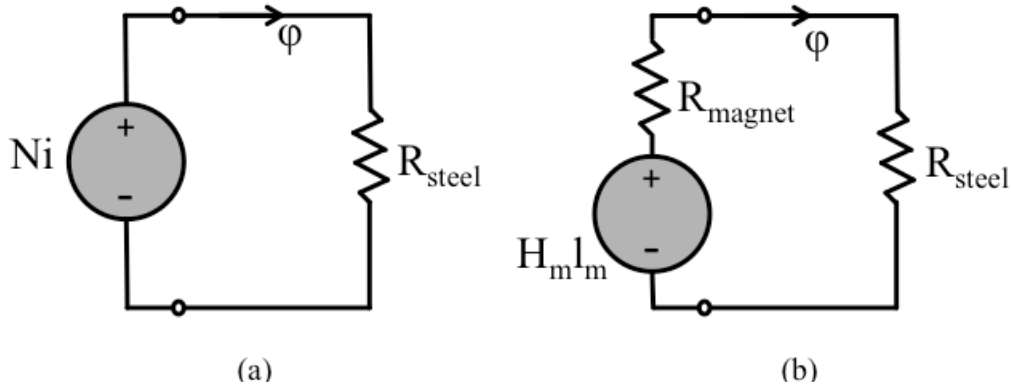


**Figure 1.5.** Simple equivalent magnetic circuits corresponding to the (a) coil and (b) permanent magnet circuits depicted in figure 1.4

Note that the permanent magnet circuit has the reluctance of magnet or MMF source reluctance included. These circuits could be given real dimensions and values and analyzed or solved using the equivalents of Ohm's law, Kirchhoff's laws, superposition, and the like for simple electrical circuits.

Except in transformers, it is generally necessary for practical devices such as motors or actuators to have an air gap in the magnetic circuit that allows for relative motion or space for coils to be wound. Ideally these gaps are kept small, or the length of the flux path through air is kept short, in an effort to minimize the associated reluctance and flux loss. Another way of thinking about it is that the low reluctance ferromagnetic materials can be used to concentrate the magnetic flux to where it is most useful, which is typically at air gaps or coils so that it can be used to generate forces, torques, or voltages.

#### 1.6.3. Voice-coil architectures

All the designs presented in this work are based on or related to voice-coil architectures. The general structure, operation, and equivalent magnetic circuit for a voice-coil system is presented below. Voice-coil designs are linear actuators or generators that were often used in speakers, hence the origin of the name. Figure 1.6 is a cross-sectional view depicting the basic mechanical structure of a voice-coil system.

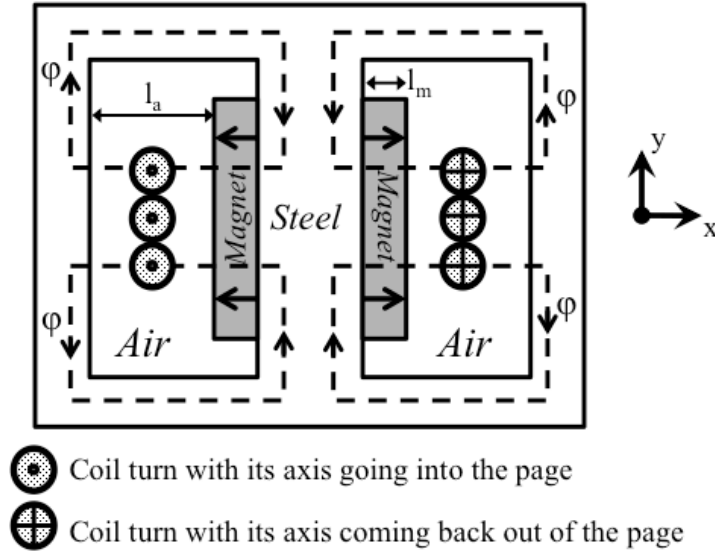


**Figure 1.6.** Mechanical cross-sectional view of a voice-coil system and the magnetic flux paths of the permanent magnets.

Figure 1.6 shows a great deal of symmetry, so it is only necessary to fully analyze one of the four flux path loops. For this analysis, the coil will be ignored even though it will be a source of magnetic flux during the operation of the device and would need to be included along with its self-inductance for completeness. To gain basic understanding of voice-coil systems, it is only necessary to analyze the magnetic circuit associated with the permanent magnet. Ultimately, the design goal is to concentrate the flux through the coil in the x-direction on the right side of the drawing in figure 1.6 and in the  $-x$ -direction on the left side. The equivalent magnetic circuit is shown in figure 1.7.

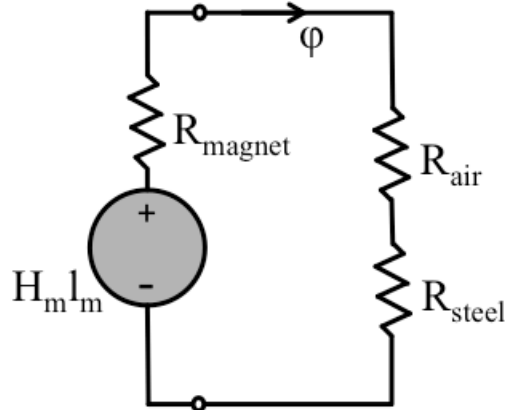


**Figure 1.7.** Equivalent magnetic circuit for one of the four flux loops of the voice-coil system in figure 1.6

The unknown in the circuit is the flux flowing through it, but an expression for the flux can be determined using the equivalent of Ohm's law for magnetic circuits.

$$\phi = \frac{H_m l_m}{R_{magnet} + R_{air} + R_{steel}} = \frac{\frac{B_r}{\mu_0} l_m}{\frac{l_m}{\mu_0 A_m} + \frac{l_a}{\mu_0 A_a} + \frac{l_s}{\mu_s A_s}}, \quad (1.11)$$

where  $l_s$ ,  $l_a$ , and  $l_m$  are the flux path lengths through the steel, air gap, and magnet, respectively.  $A_m$  is the magnet area normal to the flux path, so one dimension of this area is into the page in figure 1.6. The other dimension of  $A_m$  is half the y-dimension of the magnet because of symmetry.  $A_a$  is the area normal to the path for the air gap, and for this simplified analysis it can be assumed equal to  $A_m$ . Similarly,  $A_s$  is the area normal to the path through the steel. Note that the permeability of the magnet and air is approximated as equal to that of free space.

Ultimately, the magnetic flux density in the air gap,  $B_a$ , is the parameter that is most useful to know since it is used to calculate force and induced voltage. From equations 1.6 and 1.11,

$$B_a = \frac{\varphi}{A_a} = \frac{1}{A_a} \cdot \frac{\frac{B_r}{\mu_0} l_m}{\frac{l_m}{\mu_0 A_m} + \frac{l_a}{\mu_0 A_a} + \frac{l_s}{\mu_s A_s}}. \quad (1.12)$$

With the gap flux density known, it is possible to calculate the force developed by the voice-coil when there is a current flowing in the coil. Lorentz's law describes the force a charge feels in a magnetic field. For a current carrying conductor, the expression for this force is

$$\vec{F} = i \vec{l}_w \times \vec{B}, \quad (1.13)$$

where  $l_w$  is the length of the wire or conductor in the magnetic field. In the case of the voice-coil, the length vector of the coil and the magnetic flux density are perpendicular, and the cross product disappears. The Lorentz force becomes useful if the steel and permanent magnet structure in figure 1.6 are fixed and the coil is allowed to move in the y-direction as this allows actuation to happen.

Once there is motion between the coil and the magnet structure, it means that there are charges moving in a magnetic field, so according to Faraday's law, this motion induces a voltage in the coil. For a single coil turn, the induced voltage is given by equation 1.4 as

$$V = -\frac{\partial \varphi}{\partial t} = \frac{\partial}{\partial t}(BA) = B \frac{\partial A}{\partial t} = B l_w \frac{\partial y}{\partial t} = B l_w v, \quad (1.14)$$

where  $A$  is the area for the coil turn normal to the flux density. The length of the coil in the in the magnetic field is  $l_w$ , so referring back to figure 1.6, it is the length into the page. In figure 1.6,  $y$  is the vertical dimension and  $v$  is velocity. Since there is generally more than one coil turn, the length of the conductor in the field scales with the number of coil turns,  $N$ . Thus, the expressions in equations 1.18 and 1.19 are generally seen multiplied by  $N$ .

From equations 1.13 and 1.14, the voice-coil can be designed to be an actuator by applying a current to the coil and causing motion, or it can be designed to be a generator where the motion between the coil and the steel-magnet structure induces a voltage and current in the coil. In either case, both a force and induced voltage will be present. For this work, voice-coil architectures were used as generators.

## Chapter 2. Literature Review

---

Vibration harvesting work can be broken into two major categories that overlap, but the contributions from previous research often fall into one of two categories, resonant frequency modification or transducer design. Having harvester designs that can change their resonant frequency easily or that effectively harvest a wide range of input frequencies addresses the issue of matching the harvester resonant frequency to the input vibration frequency without significantly modifying the geometry of a device. A broadband or tunable frequency response enables a “one size fits all” harvester. Vibration transducer design research focuses more on the transduction mechanism rather than the frequency response of the inertial system in an effort to improve power outputs and power densities.

### 2.1. Resonant frequency modification

The resonant frequency of a system is defined by the system’s stiffness,  $k$ , and mass,  $m$ , and is described by the equation

$$\omega_0 = \sqrt{\frac{k}{m}}, \quad (2.1)$$

where  $\omega_0$  is the resonant frequency in radians per second. Thus, to modify the resonant system requires modifying either the mass or stiffness. Practically, it is difficult to modify the mass significantly once a device has been built, and modifying it dynamically once it is deployed would be very difficult. As a result, research has focused on changing the stiffness of a system by introducing nonlinearities in an effort to make the system less sensitive to the input vibration frequency.

In [39], changing the resonant frequency of a fixed-fixed piezoelectric beam with a proof mass at the center of the beam was accomplished by adding a buckling preload on the length axis of the beam. It was shown that the addition of preload adjusted the resonant frequency, modifying it by almost 20% with a preload of 60 N. The power output remained effectively the same over the range of modified resonant frequencies. Adjusting resonance with preload is attractive because it allows the device to be quickly tuned with the turn of a knob, but it may be limited to simple spring or beam geometries.

Another way to design a device that can harvest over a wide bandwidth of input vibration frequencies is to provide several harvester structures with overlapping resonant frequencies packaged together as investigated in [40]. In a system like this, the overall device can harvest a wide range of input frequencies, but the power density of the device is very low because only a few of the transducers will actually be harvesting power from a given vibration source at one time. Similarly, if all the overlapping resonant structures were made with the same resonant frequency, the generated power would be much higher when excited by the correct input vibration frequency, so it is a trade-off between bandwidth and power.

Another approach is to introduce forces into the resonant system that result in a nonlinear stiffness. Several works use the attractive and repulsive forces between

permanent magnets to impose a nonlinearity. In [41], small magnets on the end of a piezoelectric cantilever and corresponding magnets in the enclosure were used to harden or soften the device stiffness, and power bandwidths of 10 Hz were demonstrated. Using a very similar device architecture but adding a dynamic frequency sweep resulted in further bandwidth improvements in [42]. These improvements may be difficult to achieve in practice since a dynamic up or down sweep in frequency is necessary to fully realize the enhancements.

The other nonlinearity that has been investigated is inherent beam or spring hardening or softening that can be exploited under certain conditions to improve harvester bandwidths. In [43], the spring hardening nonlinearity that arises from large deflections in cantilever and fixed-fixed beam systems was shown to be capable of increasing resonant frequency bandwidth. Large input acceleration of 1 g or more were required to obtain the necessary large deflections. It also required that the input frequency be progressively increased, so it would require a situation where a machine was starting or ramping up in order for the effect to be realized. Along the same lines, a softening effect was characterized in [44].

While all the methods discussed above manage to modify or broaden the bandwidth of the resonant frequency of a device, they often add complexity to the mechanical system while limiting the spring structures to relatively simple geometries. Also, the input parameters in terms of input accelerations and frequency sweeps are generally not attributes of natural vibration sources.

## 2.2. Established electromagnetic vibration transducer designs

Only some of the designs created over the years will be addressed to show the highlights of what has been attempted and accomplished. For more comprehensive historical reviews of vibration harvesting transducers, refer to [45][46][28]. Electromagnetic transducer designs from previous work can be broken down into two categories. The first category is what will be called open magnetic circuit (OMC) systems that are just a permanent magnet and coils translating relative to one another. The other category is made up of systems that include some low reluctance material for flux concentration.

An early OMC device proposed in [47] consisted of a permanent magnet fixed at the base of the device and a coil suspended by a coil spring. The overall device was about  $24 \text{ cm}^3$  and produced 0.4 mW for a 0.3 g input acceleration at 2 Hz, trying to simulate human motion. The transducer was represented as a simple inertial system model with little consideration given to the magnet-coil system. In [48], a smaller OMC system was created that was  $7.3 \text{ cm}^3$  and generated 0.83 mW at 85 Hz for a 4.3 g input acceleration. The system was an N42 neodymium magnet at the center of a planar spiral spring with coils wound below the magnet-spring path of travel. The voltage from the magnet-coil system was approximated as proportional to the average measured flux density of 0.36 T, the length of the copper coil, input amplitude, and resonant frequency, and it was inversely proportional to the total damping factor for the lumped inertial system. The basic idea in [49] was the same as in [48], with a disc magnet suspended at the center of a planar spiral spring and a planar coil wound under the magnet. A very fine wire was used



to make the coils, and the number of coil turns reported were 8000 and 15000 for the two prototypes discussed. A modified form of Faraday's law was presented as the model for the voltage, but it was not in a practical form. No modeled results or analysis were presented. A rectified power of 1.2 mW was reported for a prototype that was 27 cm<sup>3</sup> for an RMS input acceleration of 0.1 g at a frequency somewhere between 50 Hz and 60 Hz. In [50], an analytic model of a magnet and coil system was presented that was based on curve fits of finite element simulations of the magnet. The model and analysis of the transducer was thorough and includes the Lorentz force from the coil. The self-inductance was ignored because the resonant frequency of the device was only 9 Hz. The device was a magnet translating in a Teflon tube with a coil wrapped around the center of the tube. Magnets at either end of the tube were oriented such that similar poles of the end magnets and translating magnet faced one another, effectively creating magnetic springs. The prototype was about 17.6 cm<sup>3</sup>, and it was evaluated using a 1.0 g input acceleration. No power was reported, but near resonance it was claimed that the presented model accurately predicted voltage and power to within 7%. OMC transducers are common, but the analysis of the magnet-coil system is usually done with a very rough approximation or left unaddressed.

The flux concentrating designs all use architectures similar to coreless motors. In [51], the cross-section of the transducer was a U-shaped steel core sitting on the end of a cantilever beam. On the inside of the vertical portions of the U were magnets oriented appropriately to create a flux loop. The coil was wound through the U-shaped core and back around on the outside of the core beyond the end of the cantilever beam. A finite element simulation was used to determine the gap magnetic flux density, but the self-inductance of the device was ignored. The device was 0.84 cm<sup>3</sup> and generated 0.04 mW at 322 Hz for a 5 g input acceleration. Along the same lines, a four pole flux loop was created in [52] with a cross-sectional structure like that of a DC coreless motor. The structure was like the U-shaped core device, but only the vertical section of the core remained, and on each were two magnets energized in opposite directions, creating a flux loop through the four magnets and two cores. The coil was wound through the top half of the flux loop and back around through the bottom half of the flux loop. Again, the magnetic circuit sat atop the end of a cantilever beam, and the overall device size was 0.06 cm<sup>3</sup>. It generated 0.003 mW at 350 Hz for a 0.3 g input acceleration. Other devices with essentially the same structure have been created in [53][54]. In each case, the self-inductance of the device was ignored, and the magnetic circuit was not presented as a major design issue.

Two commercial vibration harvesters are available that use electromagnetic transducers. Perpetuum located in the United Kingdom makes one of the commercial devices. The company spawned from work done at the University of Southampton. The overall device size is 131 cm<sup>3</sup>, and it generates 3.5 mW at 100 Hz for a 0.1 g input acceleration [28]. The other commercial device is by Ferro-solutions. The Ferro-solutions device is 133 cm<sup>3</sup> and generates 10.8 mW at 60Hz for a 0.1 g input acceleration [28]. Specifics for the internal transducer designs are unknown.

Table 2.1 summarizes the achievements of the major works on vibration harvesters that use electromagnetic transduction. It provides points of comparison for evaluating designs. Many of the numbers were taken from [46] and [28]. In the case of the Perpetuum and Ferro-solutions devices, the power densities were based on rectified

powers whereas the power densities of the other devices were based on the power dissipated in an optimal load resistance.

**Table 2.1.** Table of normalized power for vibration harvesters using electromagnetic transduction

Author, Reference	Frequency [Hz]	Acceleration [g]	Size [cm <sup>3</sup> ]	Power density [mW•cm <sup>-3</sup> •g <sup>-2</sup> ]
Amirtharajah, [47]	2	0.3	24	0.19
Lee, [48]	85	4.3	7.3	0.0061
Waters, [49]	50-60	0.1	27	4.44
El-hami, [51]	322	5.0	0.84	0.0019
Beeby, [52]	350	0.3	0.06	0.56
Perpetuum, [28]	100	0.1	131	2.67
Ferro-solutions, [28]	60	0.1	133	8.12

## Chapter 3. Generalized harvester model

### 3.1. Determining a general equation of motion

The general model for the vibration harvester designs discussed in this work has one mechanical degree of freedom and one electrical degree of freedom. A single lumped mechanical degree of freedom is appropriate because the resonant mass of the magnetic circuit is much larger than the mass of the beams of the springs, and the mass of the magnetic circuit is essentially a point load on the end of the beams that make up the spring. Furthermore, the springs constrain the motion to a single axis, and with a proper spring design, the translation amplitudes are not large enough with typical vibration inputs for mechanical hardening of the springs to occur. Thus, the mechanical system is molded as a simple mass, spring, and damper system with the vibration acting as a forcing function [31].

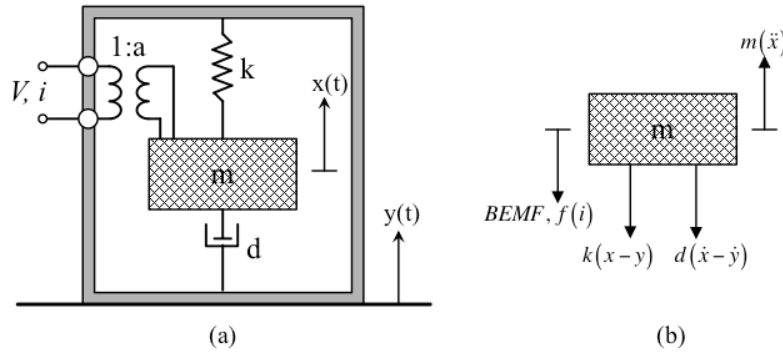


**Figure 3.1.** (a) The mechanical system, and (b) the forces present. The base or input motion is  $y(t)$ , and  $x(t)$  is the motion of the resonant mass,  $m$ . The spring stiffness is  $k$ , and  $d$  is the mechanical damping. The transducer is represented by  $1:a$ .  $V$  is the induced voltage, and  $i$  is the induced current. BEMF is the force due to transduction and is a function of the induced current.

The mechanical and electrical degrees of freedom are coupled through the transducer, so the force balance and equation of motion has an electrical term, the BEMF force in figure 3.1(b). That term is a Lorentz force associated with current induced in the coil, and it is essentially a back EMF term. The system can be represented by an equivalent electrical circuit.

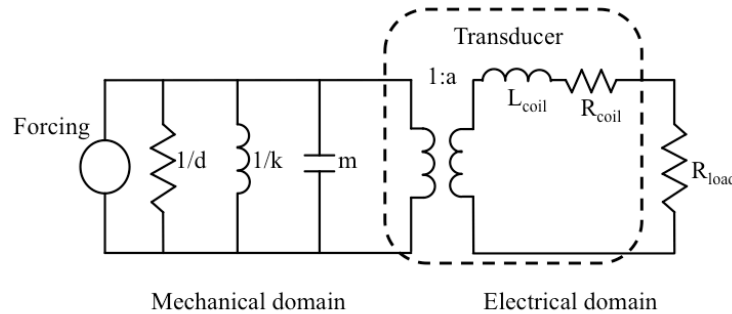


**Figure 3.2.** Equivalent circuit for an electromechanical harvester system with an electromagnetic transducer, with  $d$  representing the mechanical damping,  $k$  the spring stiffness, and  $m$  the resonant mass.  $L_{\text{coil}}$  and  $R_{\text{coil}}$  are the inductance and resistance, respectively, of the coil in the magnetic circuit. The electrical load is simply a resistor,  $R_{\text{load}}$ .

From figure 3.1(b), the force balance is

$$m\ddot{x} = -d(\dot{x} - \dot{y}) - k(x - y) - BEMF(i) . \quad (3.1)$$

With the addition of the term  $m\ddot{y}$  for some forcing function on the base, the force balance becomes

$$m\ddot{x} = -d(\dot{x} - \dot{y}) - k(x - y) - BEMF(i) + m\ddot{y} . \quad (3.2)$$

Since the relative motion between the base and resonant mass is the point of interest, the relative distance is defined as  $z(t) = x(t) - y(t)$ . Substituting the relative motion parameter into equation 3.2 and dividing by the mass yields a form typical for an equation of motion.

$$\ddot{z} + 2\omega_0\zeta\dot{z} + \omega_0^2z + \frac{1}{m}BEMF(i) = \ddot{y} , \quad (3.3)$$

where

$$\omega_0 = \sqrt{\frac{k}{m}} , \text{ and } \zeta = \frac{d}{2m\omega_0} .$$

It is typical for the base motion to be modeled as simple harmonic motion, so the acceleration is described by

$$\ddot{y} = Y\omega_y^2 \cos(\omega_y t) , \quad (3.4)$$

where  $Y$  is the amplitude of the motion.  $\omega_y$  is the angular frequency, and  $t$  is time. Finally, the BEMF term typically has a form similar to the general Lorentz force equation, but the cross product is not necessary because of the device geometry. For a voice-coil device, the BEMF term is

$$BEMF(i) = NBl_w i , \quad (3.5)$$

where  $N$  is the number of coil turns,  $B$  is the air gap flux density, and  $l_w$  is the length of a coil turn in the magnetic field.

Some authors transform the Lorentz force term into a mechanical damping term so that the whole system can be simplified to a single mechanical degree of freedom system [51][55][54]. However, this ignores the self-inductance of the coil. For electrical loads more sophisticated than a resistor, i.e., rectification circuitry, such a simplification does not work.

## 3.2. Determining the voltage equation

### 3.2.1. Voltage source

As shown in figure 3.2, the electrical circuit for the transducer is simple because all the power generated is dissipated in a load resistor. The voltage source for the simple RL circuit is the induced voltage from Faraday's law.

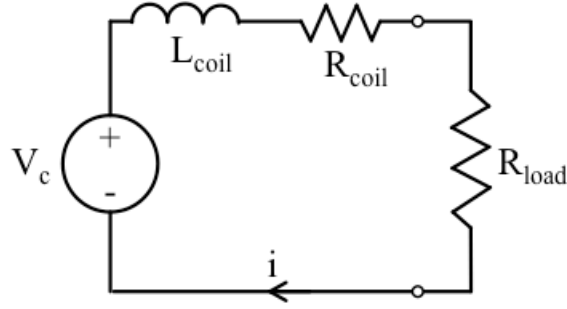


**Figure 3.3.** Electrical circuit for the transducer

The voltage equation for the circuit in figure 3.3 is

$$V = (R_{coil} + R_{load})i + L_{coil} \frac{di}{dt} + V_c, \quad (3.6)$$

where  $V_c$  is the induced voltage. Equation 1.19 describes the induced voltage, and for a voice-coil, it typically has the form

$$V_c = NBL_w v, \quad (3.7)$$

where  $v$  is the relative velocity between the coil and the magnetic field.

### 3.2.2. Self-inductance

All the devices presented in this work have a single coil, so a single inductance, the self-inductance, needs to be determined. For a coil with a well defined low reluctance path, the self-inductance is given by [37][38]

$$L = \frac{N^2}{R}, \quad (3.8)$$

where  $N$  is the number of coil turns, and  $R$  is the reluctance of the flux path for the coil. For the general voice-coil system presented at the end of chapter 1, the low reluctance path, ignoring leakage, is through the steel in the flux loops shown in figure 3.4(a).

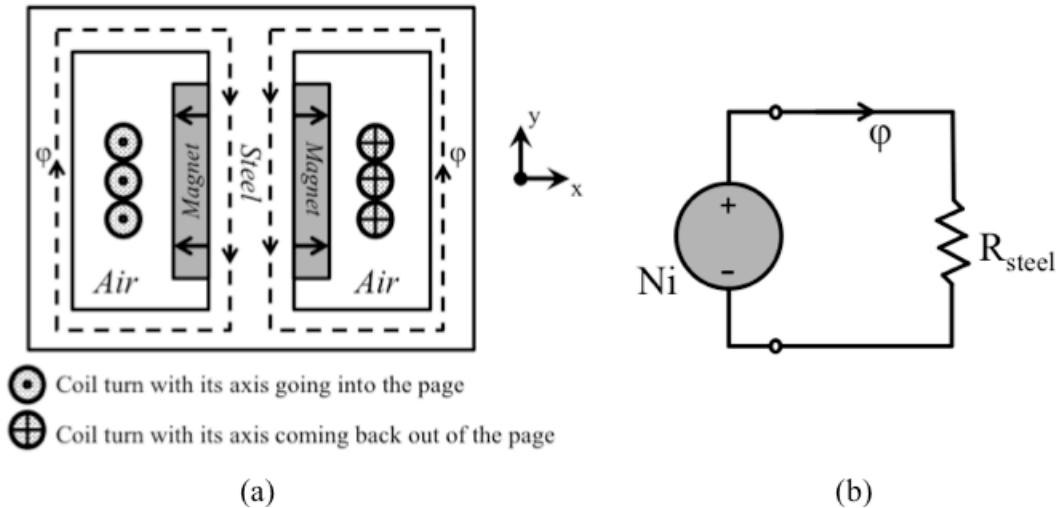


**Figure 3.4.** (a) Mechanical structure cross-section showing self-inductance flux loops. (b) Equivalent magnetic circuit for the self-inductance flux loops.

From figure 3.4, the R in equation 3.8 can be approximated as the reluctance of the steel for both flux paths, so the areas and lengths of path must be properly accounted for in reluctance calculation.

Several of the designs contain coil configurations that have no low reluctance path, so the above method of calculating the self-inductance is not valid. The self-inductance of these air core coil configurations can be approximated with equations developed for radio coils in works such as [56] and [57]. A simple approximation for the self-inductance of a solenoid is

$$L = 4\pi N^2 \frac{\text{Area of cross section}}{\text{Length}} \Theta, \quad (3.9)$$

where  $\Theta$  is a geometry factor that is tabulated in [56].

For modeling prototypes or physical systems, the inductance can be directly measured with a multimeter and used in calculations.

### 3.3. Full system of differential equations

The full set of differential equations describing the motion and electrical output of the generator define the velocity and acceleration of the resonant mass in the mechanical domain as well as the current induced in the electrical domain. For a general voice-coil system, the magnitude of the flux density field is approximately constant for every coil turn, so induced voltage and Lorentz force terms can be multiplied by the number of coil turns, N. With harmonic base motion, the velocity equation, the equation of motion, and the voltage equation can be rearranged and put into matrix form [37][38].

$$\frac{d}{dt} \begin{bmatrix} z \\ v \\ i \end{bmatrix} = \begin{bmatrix} 0 & 0 & 0 \\ Y\omega_y^2 \cos(\omega_y t) & 0 & 0 \\ 0 & 0 & 0 \end{bmatrix} - \begin{bmatrix} 0 & -1 & 0 \\ \omega_0^2 & 2\omega_0\zeta & -\frac{1}{m}NBl_w \\ 0 & \frac{NBl_w}{L} & \frac{R_{coil} + R_{load}}{L} \end{bmatrix} \begin{bmatrix} z \\ v \\ i \end{bmatrix}. \quad (3.10)$$

In the abbreviated matrix form, equation 3.10 is simply

$$\frac{dZ}{dt} = F - CZ. \quad (3.11)$$

Some of the designs that will be presented do not have a constant gap magnetic flux density. In those cases, the terms in equation 3.10 with B in them become summations over the number of coil turns, N, that need to be calculated at each time step.

## Chapter 4. Device designs

---

Cored and coreless linear generator designs were considered for converting mechanical vibrational energy to useful electrical energy. Cored designs use coils wrapped around low reluctance material and have very short flux path lengths through air. The cored designs explored were variable reluctance devices that will be discussed in Appendix B, because they proved unsuitable for the desired application. Coreless devices have larger air gaps in the flux path typically to accommodate coils with air cores, making them less magnetically efficient, but simpler. Therefore, after it was determined that cored designs were not suitable for harvesting low level vibrations because of their complexity and large magnetic forces, the design focus shifted to simple coreless architectures like voice-coils. The two simplest coreless structures, an open magnetic circuit and a voice-coil, were analyzed, prototyped and tested. Two other coreless structures similar to those of coreless permanent magnet pancake motors were also analyzed as possible improved designs with higher gap magnetic flux densities. This chapter introduces and presents the basic analysis of the resonant spring design and the four coreless transducer designs that were considered.

### 4.1. Mechanical device design constraints

The target size for the vibration harvesters was a cube with side lengths of 2.5 cm because that is roughly the size of a C-cell battery, which is a battery size that potentially stores enough energy to power a wireless sensor node for a decade. The target resonant frequency range was 20-120 Hz. This frequency range compares well with the vibrations of industrial and manufacturing equipment as seen in section 1.4.1. The resonant frequency was to be adjustable with different interchangeable spring geometries. The amplification of the input vibration due to resonance was expected to be a factor of 25–100 based on impulse ring-down tests on large spring structures of similar design. Assuming sinusoidal vibrational motion, the resonant mass translational amplitude was expected to be about 2 mm for a 0.2 g input vibration acceleration at 25 Hz with an amplification of 100, so the maximum allowable translational amplitude was set at 2.5 mm. With the rough size, frequency, and translational amplitude bounded, the last design constraint was to use readily available magnet sizes for practical reasons. With these constraints, the task was then how best to fill the volume of the harvester with electromagnetic generator designs.

**Table 4.1.** Design goals and constraints

Parameter	Value
Overall size L x W x H [cm]	2.5 x 2.5 x 2.5
Frequency range [Hz]	20–120
Input acceleration [g]	$\leq 0.2$
Power target [mW]	$> 0.4$
Max. translation amplitude [mm]	2.5

## 4.2. Resonant system

The resonant system for the vibration harvester designs consisted of a planar spiral beam structure that governed the stiffness,  $k$ , of the system, and the magnetic circuit dominated the mass of the system. Generally, the smaller the structure the higher its resonant frequency, so the challenge for vibration harvesters is to get small structures to have low resonant frequencies. For industrial, commercial, and residential applications, resonant frequencies below 150 Hz are desirable. Beam structures are desirable springs because they are compact and can exhibit low out-of-plane stiffness along with comparably higher in-plane stiffness. Thus, the beams can allow out-of-plane motion while resisting in-plane motion. The resonant frequency of a structure is

$$\omega_0 = \sqrt{\frac{k}{m}}, \quad (4.1)$$

where  $m$  is the mass of the resonant system. The greatest freedom for modifying the resonant frequency of a system as a designer lies in the stiffness term. Starting with the stiffness of a simple cantilever beam, it is clear that the thickness,  $t$ , and length,  $L$ , are the dominant terms.

$$k_{cantilever} = \frac{Ewt^3}{4L^3}, \quad (4.2)$$

where  $E$  is the Young's modulus and  $w$  is the width of the beam. Clearly, achieving lower resonant frequencies requires longer and thinner beams. Practically, there is a limit to how thin a beam can be, but longer beams can be made using multiturn or spiral patterns as shown in figure 4.1. Many multiturn beam geometries were evaluated in [58]. A spiral, crab-leg, structure was the planar structure with the lowest out-of-plane stiffness, allowing a lower resonant frequency for a given area.

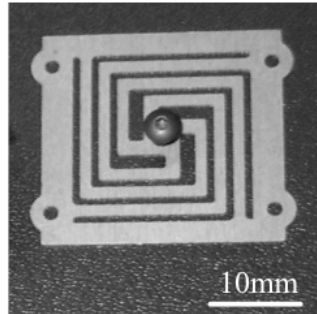


**Figure 4.1.** Stainless steel spring using a spiral beam structure.

Since the resonant frequency of the harvester needs to be designed to match that of the target vibration, it is helpful to have an analytic equation that can be used to quickly modify the beam dimensions to get to a desired resonant frequency. This can save considerable time over iterating geometry through a finite element frequency analysis. The basic analysis for calculating an analytic formulation for a multiturn beam was done for a two beam crab-leg structure in [58]. Drawing from that basic analysis, the stiffness for a three-beam spiral was found. The procedure can be expanded to any number of turns.



The stiffness,  $k_z$ , for the suspension is calculated by assuming some force ( $F_z$ ) on the end of the beam and solving for the resulting displacement ( $\delta_z$ ).

$$k_z = \frac{F_z}{\delta_z}. \quad (4.3)$$

The vertical displacement of the beam is determined by using the strain energy from torsion ( $U$ ), the free body diagram (figure 4.2) moment and torque balances, the boundary conditions on the guided ended of the beam for tilt ( $\theta_0$ ) and rotation ( $\phi_0$ ), and, finally, Castigliano's theorem.

$$U = \int_0^L \left( \frac{M^2}{2EI_x} + \frac{T^2}{2GJ} \right) d\xi, \quad (4.4)$$

where  $\xi$  denotes strain,  $G$  is the shear modulus of the material,  $M$  is the moment,  $T$  is the torsion,  $I_x$  is the moment of inertia, and  $J$  is the torsion constant for a rectangular cross-section beam.

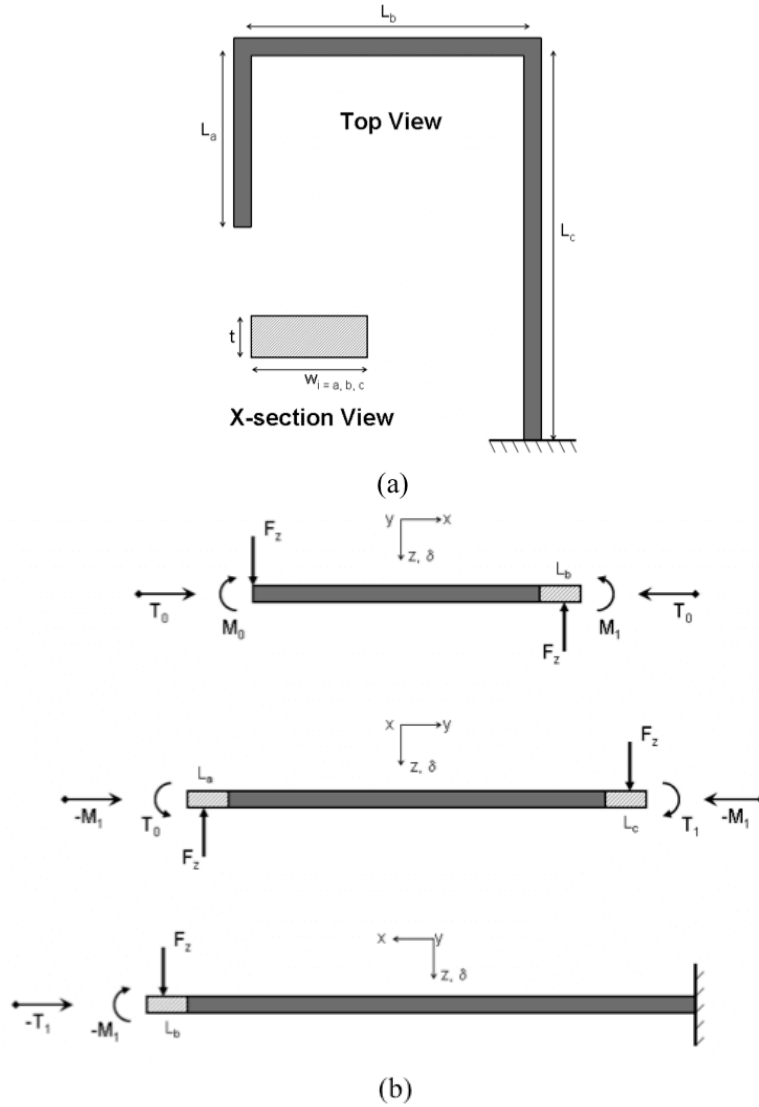


**Figure 4.2.** (a) Top view of the 3-beam spiral structure, and (b) the free body diagrams of the 3 links of the spring.

The guided end conditions are given by

$$\theta_0 = \sum_{i=a}^c \int_0^{L_i} \left( \frac{M_i}{EI_{x,i}} \frac{\partial M_i}{\partial M_0} + \frac{T_i}{GJ_i} \frac{\partial T_i}{\partial M_0} \right) d\xi, \quad (4.5)$$

$$\phi_0 = \sum_{i=a}^c \int_0^{L_i} \left( \frac{M_i}{EI_{x,i}} \frac{\partial M_i}{\partial T_0} + \frac{T_i}{GJ_i} \frac{\partial T_i}{\partial T_0} \right) d\xi, \quad (4.6)$$

where  $M_0$  and  $T_0$  are the unknowns in the moment and torsion balances. Finally, applying Castigliano's theorem provides an expression for the vertical displacement.

$$\delta_z = \sum_{i=a}^c \int_0^{L_i} \left( \frac{M_i}{EI_{x,i}} \frac{\partial M_i}{\partial F_z} + \frac{T_i}{GJ_i} \frac{\partial T_i}{\partial F_z} \right) d\xi. \quad (4.7)$$

Additional terms can be added or subtracted from the summations in equations 4.5–4.7 as the number of beam segments increases or decreases. The resulting stiffness equation is very lengthy, especially when the three beam segments have different widths, but it is quite tractable and useful.

The general case for the spiral structure has beams with constant and equal widths,  $w$ , and equal gap spacing,  $g$ , as shown below.

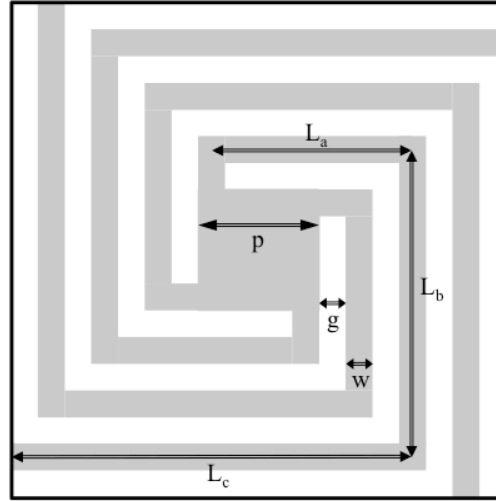


**Figure 4.3.** Simplest case three-beam spiral spring structure with equal beam widths,  $w$ , and equal gap spacing,  $g$ .

In this basic case, the beam lengths can be calculated as

$$L_a = p + 2g + w, \quad (4.8)$$

$$L_b = p + 6g + 3w, \quad (4.9)$$

$$L_c = p + 8g + 4.5w, \quad (4.10)$$

where  $p$  is the side length of the square center platform. Equations 4.8–4.10 can be useful during initial analysis and mechanical modeling.

## 4.3. Prototyped designs

### 4.3.1. Open magnetic circuit (OMC)

The simplest electromagnetic transducer is an open magnetic circuit system where there is no low reluctance flux path or flux concentration, hence the “open circuit” designation. It is just permanent magnetic material translating relative to coils. Therefore the only volume trade-off for a generator is between the magnetic material and the coils. Cylindrical axially magnetized magnets were used because of the convenience for winding coils. Using axially magnetized magnets was the most practical for the prototype because such magnets are readily available. Radial magnetizations are hard to make and find, and diametrical magnetizations have magnetic fields such that the induced voltages and forces described by equations 1.13 and 1.14 cancel on either side of the axis of the magnet because of the vector interactions, making it a poor choice for a generator. Figure 4.4 shows the basic layout of the OMC system, but it does not show any of the support structures like frames or attachment mechanisms to the springs for the resonant system.

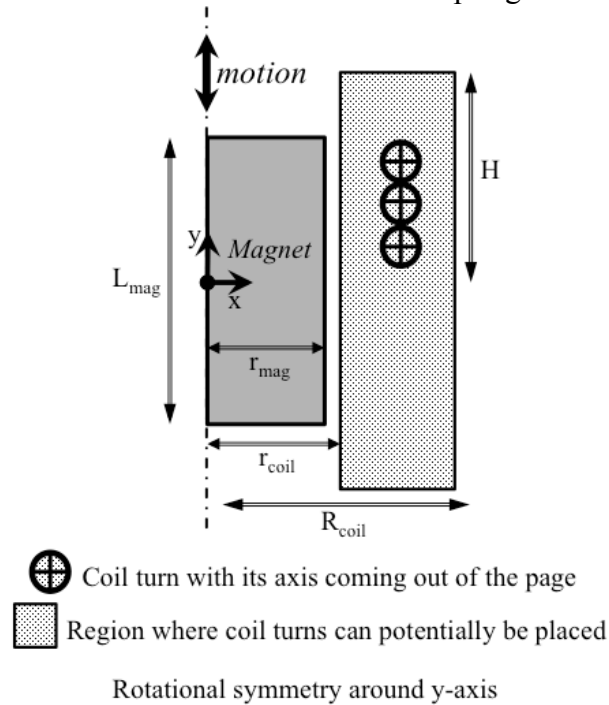


**Figure 4.4.** Cross-section and half symmetry of OMC system showing the basic dimensional parameters that need to be determined for physical bounds that constrain the design analysis.

#### 4.3.1.1. General OMC design guide

##### 1) Environment:

- a. The environment may impact the choice of magnetic material and the design of the support structure or enclosure. High and low temperatures can be problematic for various magnetic materials. Ideally, the support structure and enclosure would be non conductive so that eddy currents are not induced by the moving magnet.

- b. Mounting the device on or near enough to a steel or iron structure will causing restricted or no motion of the resonant system because the magnet will be attracted to the mounting surface. Mounting on iron surfaces is better suited to flux concentrated transducer designs.

2) **Dimensional constraints:**

- a. **Overall size:** For a custom solution, the overall device size and expected motion will be determined by the environment, vibration source, power requirements of the application, and mounting. Ideally, the design target is a universal solution of compact size and high power output.
- b. **Support structure:** After settling on an overall size, the general support structure for the springs and housing should be defined because it may further restrict the size of the OMC magnet-coil system.
- c. **Assembly:** Consideration should also be given to assembly of the overall device as that may also define the size of the OMC system.
- d. **Translation amplitude:** Determine the maximum translation amplitude so that proper offsets are built into the design to allow for the expected motion. The impact on the OMC system is that coil turns cannot occupy space that will be swept by the springs during normal operation. The translation amplitude further restricts the region where potential coil turns can be placed.
- e. **Tolerances and gaps:** Incorporate appropriate gap tolerances so that there are no interferences during device assembly and there is space to allow for the relative motion between the magnet and coils.

3) **Magnet size:**

- a. Custom magnet dimensions: Skip to 4.
- b. Standard magnet sizes: Determine the set of magnets in terms of length and diameter that satisfy the dimensional constraints that define the space available for the OMC system.

4) **Evaluate the set of possible magnet-coil configurations:**

The optimal coil solution may not fully fill the region available for coil turns and potentially has a strange cross sectional profile that is impractical to manufacture. This set of odd potential solutions can be eliminated by requiring a coil with a rectangular cross sectional profile. The implication is that during the construction and evaluation of simulated coil configurations, layers of coils are progressively added rather than individual coil turns. Also, coil configurations should be judged based on their power generation potential. Determine whether or not the power contributed by a layer of coils worth its additional resistance.

- a. **Flux density field:** Using a finite element package, simulate the flux density field for the magnet dimensions to be evaluated. Discretize the field with a spatial step size equal to the diameter of the magnet wire to be used for the coil.
- b. **Coil configurations:** Build the set of possible coil configurations given the magnet size being evaluated.
- c. **Evaluation:** Evaluate the coil configurations by assuming simple harmonic motion of the magnet of an appropriate amplitude and frequency. Implementing the full system of differential equations that

model the device is not necessary for evaluating the coil-magnet configurations since the only interest is finding the configuration with the highest power production potential. Calculate the induced voltages and evaluate the power potentials for the set of coil configurations as described in the design case.

- d. **Iteration:** Iterate through steps 4a to 4c for all the magnet sizes or range of magnet dimensions of interest, and pick the best magnet-coil configuration from the set.

5) **Refinement:**

- a. Add a non-ideal coil packing efficiency, generally 50-75%, and estimate the other parameters necessary to implement the full system of differential equations in section 3.3 so that realistic expected voltage and power outputs can be simulated.

4.3.1.2. *OMC design case considerations, simplifications, and analysis for the prototype*

Figure 4.5 shows a finite element analysis (FEA) of the magnetic flux density field for a neodymium N42 rare earth magnet. The arrows show the orientation of the field. Clearly, the field orientation and magnitude are changing spatially. Due to the symmetry of the field, it is not necessary to analyze the whole magnet.

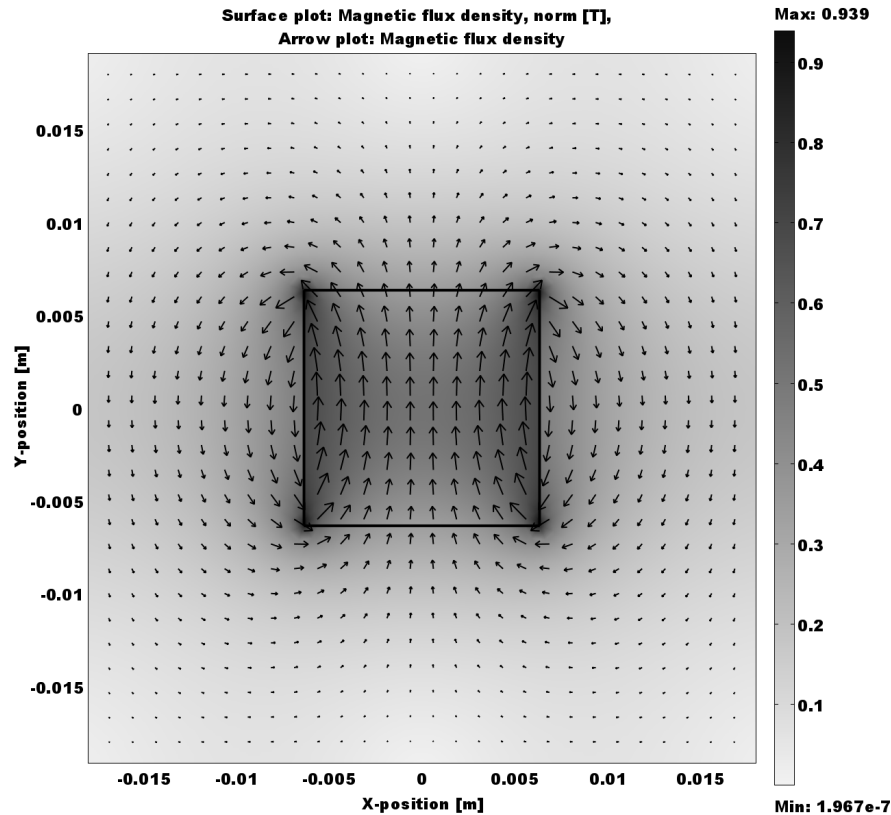


**Figure 4.5.** FEA of a cylindrical neodymium N42 magnet with its axis and magnetization along the y-axis sitting in air. The magnet is 12.7 mm in diameter and 12.7 mm long. The surface plot color map corresponds to the magnitude of the magnetic flux density field, and the arrow plot depicts the flux density field orientation. The arrow size is proportional to the magnitude of the field at the tail end of the arrow.

Since the magnet is part of the mass of the resonant system, it will be moving while the coils are fixed to the base mounted to the vibrating surface. The axis of motion is the same as the axis of the magnet, so coils cannot be placed along the top or bottom of the magnet inside its radius. The task is then to determine the best places to put coils circumferentially around the magnet.

Before placing coils and running through a rigorous analysis and calculation, it is worth taking closer examination of the flux density field associated with the magnet while considering the motion and forces that will arise. If a single circumferential coil turn around the magnet and the Lorentz force on that turn are considered, only the x-axis or radial component of the flux density field results in a net force because of the cross-product relationship between the magnetic field and the current in the coil. Similarly, the induced voltage in the coil turn due to the relative motion between the magnet and coil is proportional to the x-component of the flux density field. Therefore, considering only the x-component of the field shown in figure 4.6 should show the best regions to place coils.

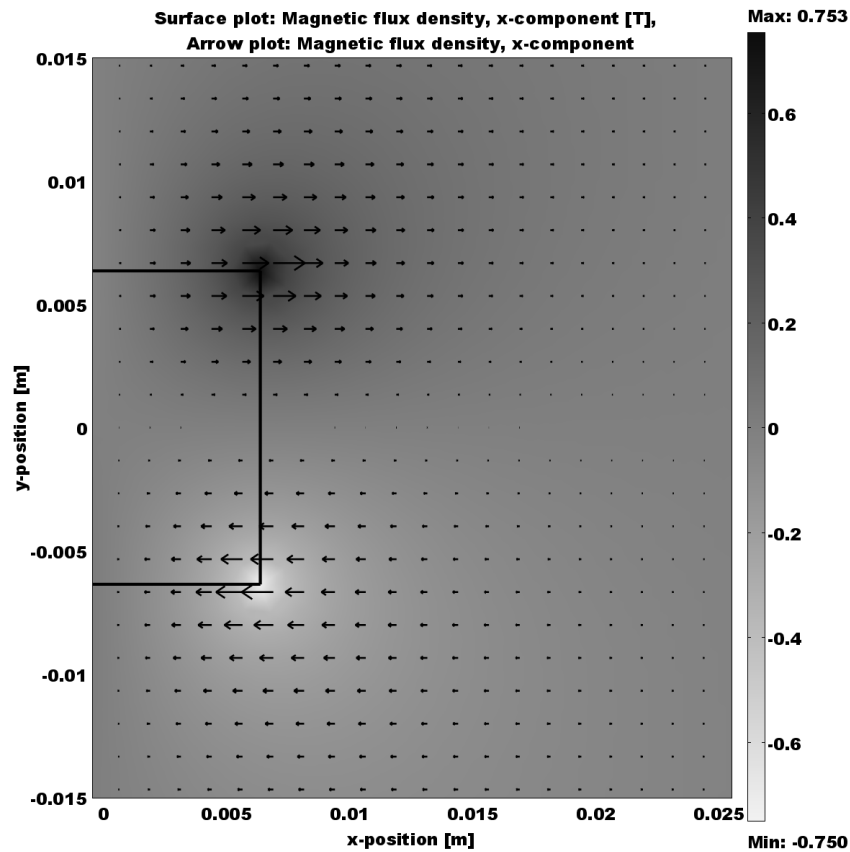


**Figure 4.6.** FEA of the right half of the magnet in figure 4.5. The surface plot color map corresponds to the magnitude of the x-component of the magnetic flux density field, and the arrow plot depicts the x-component of the flux density field. The size of the arrow is proportional to the magnitude of the field at the tail end of the arrow.

From figure 4.6, it is clear that the x-component of the magnetic field “flips” from the positive x-direction for the top half of the magnet to the negative x-direction for the bottom half. The field’s change in direction means that there will be a cancelling effect for a multiturn coil that is symmetric about the radial plane from the midpoint of the axis

of the magnet. This cancelling effect, where the induced voltages from the top half of the coil cancel the induced voltages from the bottom half, is only problematic for small relative motion translation amplitudes, which is the case for harvesting vibrations. A small relative motion amplitude might be considered an amplitude that is less than half the length of the magnet. Full analysis with respect to translation amplitude was not carried out, so the definition of small amplitude motion is based on intuition. The same analysis holds for any motion amplitude, so an optimum solution can be calculated for any given situation.

For the small translation amplitudes of less than 2.5 mm associated with the vibration harvester, it is clear that having independent coils for the top and bottom halves of the magnets would be the best solution. By symmetry, the optimum coil configuration would be the same for the top and bottom halves of the magnet, but the induced voltage would be 180 degrees out of phase. The symmetry simplifies the analysis to a single quadrant of the magnet.

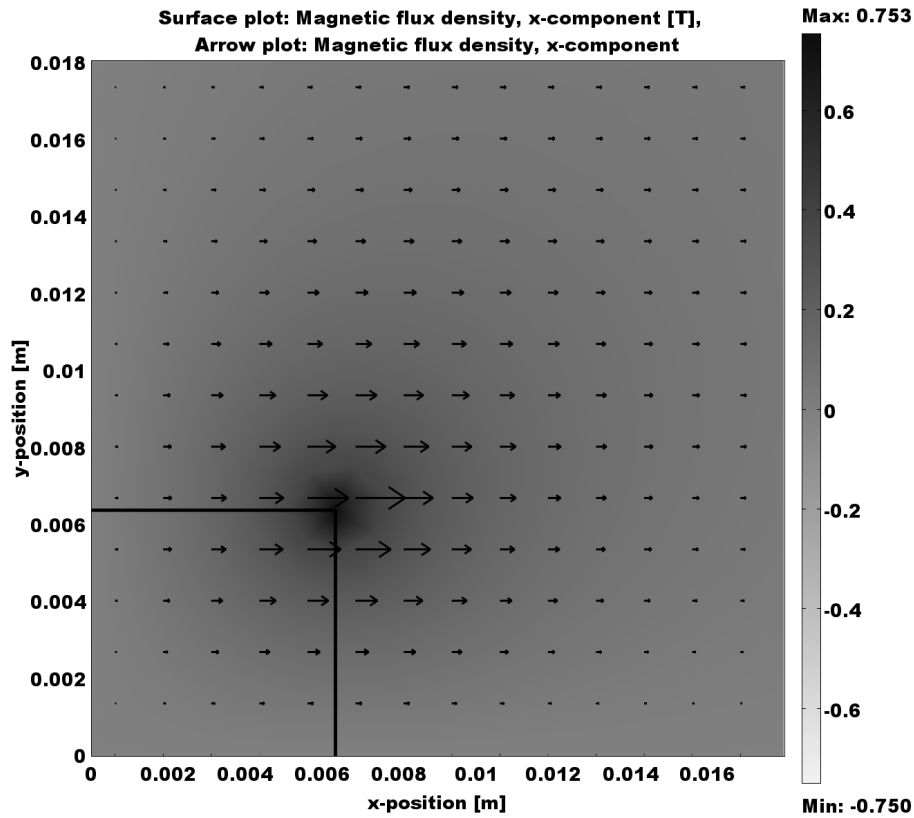


**Figure 4.7.** FEA of the upper right-hand quadrant of the magnet shown in figure 4.5. The surface plot color map corresponds to the magnitude of the x-component of the magnetic flux density field, and the arrow plot depicts the x-component of the flux density field. The size of the arrow is proportional to the magnitude of the field at the tail end of the arrow.

The analysis involves placing coil turns around the magnet using the mechanical constraints that bound the overall size of the coil. The induced voltage in each individual coil turn can then be calculated using 1.14, but since the magnitude of the flux density field cannot be approximated as constant, a summation over the coil turns is required to get the full induced voltage for the coil instead of simply multiplying by the number of

coil turns. A set of discretized finite element simulations of a quadrant for each of the magnets to be evaluated was used to get the necessary flux density values for the voltage calculations. The full induced voltage,  $V_c$  in the voltage equation of the general model, is given by

$$V_{total} = V_c = \sum_1^N Bl_w v = \sum_1^N B_x(x, y, y_w) \cdot 2\pi x \cdot \frac{dy}{dt} \quad (4.11)$$

where the  $B_x$  term is the x-component of the magnetic flux density field at the position of the coil turn. The complication is that the magnitude of the field changes as the position of the magnet changes along its travel, and that is why the  $y_w$  dependence is included to account for the changing relative position between the magnet and coil turn. Basically, for any given coil turn, the magnitude of the flux density field is spatially and temporally dependent. Note that this same summation without the velocity term is what needs to be done to calculate the terms in equation 3.10 that contain B.

$$NBl_w \text{ terms get replaced by } \sum_1^N B_x(x, y, y_w) \cdot 2\pi x.$$

The next step is to build the set of possible coil layers based on the discretization and physical bounds.

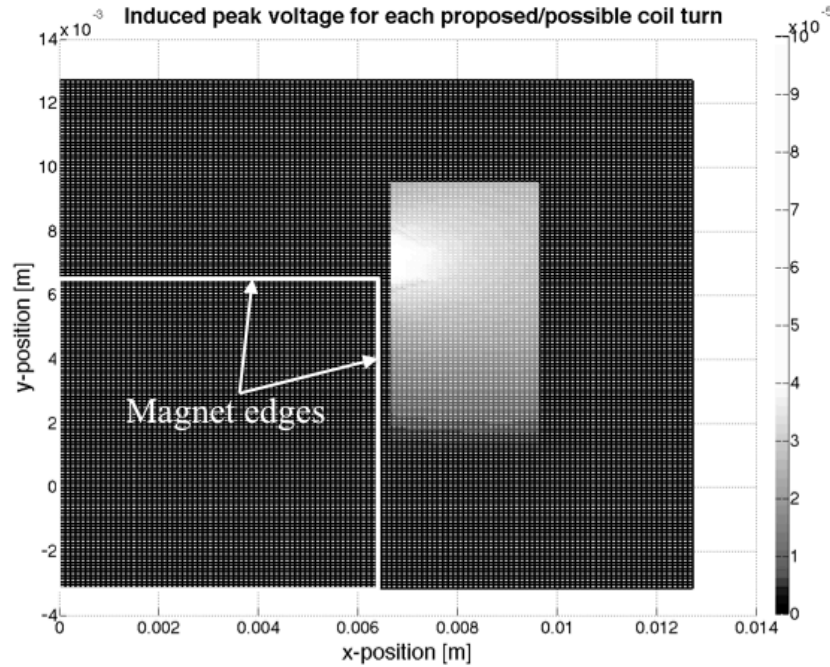


**Figure 4.8.** An example of the discretized space used to calculate voltage, power, and optimal magnet-coil configurations. The colorbar units are volts. This plot of the peak induced voltage in all the possible individual coil turns uses the x-component flux density field associated with a 12.7 mm dia. and 12.7 mm long N42 neodymium magnet. The simulated magnet motion was harmonic with a 0.6 mm amplitude at a frequency of 40 Hz. The magnet edges are overlaid as reference, and [0,0] is the center of the magnet. The plot shows all the physical bounds placed on the area where coils could be placed except the lower y-axis bound which was at  $y=0$ . That bound is not well defined by the voltage plot because the induced voltages near the middle of the magnet are small.



With a discretized flux density field map and knowing the physical bounds of the coil, the calculation for the optimum coil becomes whether the power contribution of a coil layer is worth its added resistive loss. This trade-off can be evaluated quickly with some simplifications and by assuming simple harmonic motion of an appropriate amplitude and frequency. The first simplification is to assume that the resistance dominates the inductance so that the voltage and current can be approximated as in phase, allowing power to be calculated as the square of the voltage divided by resistance. Given that the coil has an air core and that the frequencies are low, less than 150Hz, this approximation is generally reasonable. Measurements on a prototype verified that the phase difference between the voltage and current was less than 10 degrees for the frequencies that a vibration harvester would see. The second simplification is to assume the coil is ideally formed or wound. Real coils do not have 100% packing efficiency, but adding a packing factor into the discretization and simulation requires needless complexity when trying to determine the overall best magnet-coil geometry. Finally, the trade-off being evaluated only concerns the added resistance of a coil layer, so the power being calculated does not consider an external load and therefore is meaningless for a practical system.

#### *4.3.1.3. Practical considerations for the prototype within the imposed 2.5 cm cube constraint*

The physical bounds of the coil were determined by the overall device size and expected maximum travel. The maximum outer radius x-axis dimension for the coil was 1.02 cm and was determined by the assembly issue of being able to insert the coil into the overall frame. The lower bound y-axis dimension of the coil was the center of the device, which corresponded to the center of the magnet when the system was at rest. The upper y-axis coil bound was 2.5 mm below the upper spring to allow for the travel of the spring and magnet. To find the best practical magnet-coil configuration, several standard diameter magnets and two variations in magnet length were evaluated. Of the two magnet lengths, 19.05 mm and 12.7 mm, the longer magnet was less effective for a given diameter even though it put more magnetic material into the volume of the harvester. Figure 4.6 shows that the highest flux densities are near the top and bottom edges of the magnet, so, intuitively, as much of the coil as possible should be swept by the top or bottom edge of the magnet during its travel. Having a longer magnet moves those edges further from the region where coils could physically be placed in the harvester. As a result, the 12.7 mm long magnet was chosen, and the only parameter left to define was the magnet diameter.

Standard magnet diameters from 6.35–15.88 mm were evaluated. In each case, the optimal coil went up to the upper y-axis physical bound and the outer x-axis physical bound. The lower y-axis edge of the optimal coil was always offset from the lower bound of the center of the device by 2–4 mm because the x-component of the flux density in that region around the center of the magnet is very small, as figure 4.8 shows. As a result, putting coils in that region would contribute little or no induced voltage but contribute significant resistance. Given the constraints of the device, the best magnet diameter was determined to be 12.7 mm because it had the highest power potential from the set of magnet-coil configurations evaluated, as shown in figure 4.9.

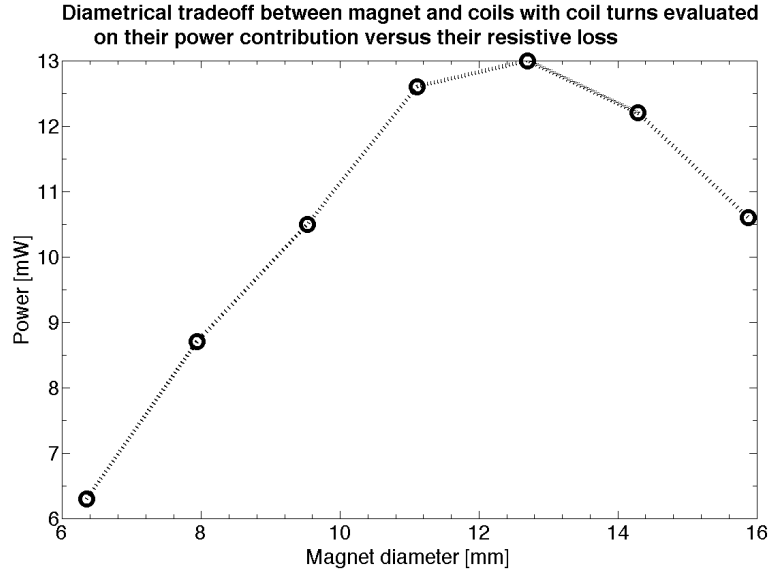


**Figure 4.9.** Plot showing the magnet diameters and associated coil configurations that were evaluated to determine the best choices, given the physical constraints imposed by the device geometry. The power shown is more a power potential for the given configuration than a power that could be delivered to a load.

The lower edge of the coil that performed best according to the power-versus-resistive loss simulation for the 12.7 mm diameter magnet configuration was approximately 3 mm from the center of the device.

Once a magnet-coil configuration had been chosen, the actual performance of the system could be modeled using the system of equations in section 3.3. Inclusion of a non-ideal coil packing efficiency was achieved by modifying the summations over the number of coil turns in equation 4.11 and the like. Packing efficiencies of 50–75% were observed for the prototypes created over the course of this work, so simply skipping every second, third, or fourth possible coil turn gave a reasonable range for the performance of a device. The only real unknown is the mechanical damping ratio,  $\zeta$ . Typical damping ratio values for a variety of devices with similar planar spiral spring structures back calculated from impulse responses or steady state displacement measurement ranged roughly from 0.02–0.001.

#### 4.3.2. Voice-coil (VC)

The standard voice-coil design presented at the end of chapter one has the added mechanical complexity of a low reluctance flux path compared to the open magnetic circuit design. The added complexity provides flux concentration. The basic mechanical structure of the magnetic circuit has the same form as that shown at the end of chapter 1, but because of the symmetry around the y or vertical axis of the cross section, only one side of the structure needs to be analyzed as shown below.

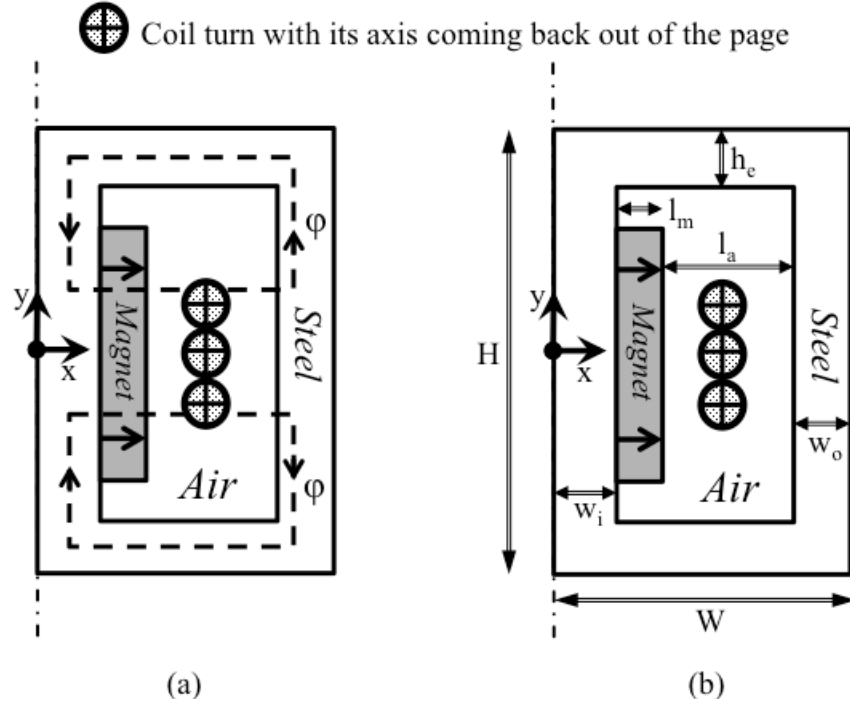


**Figure 4.10.** (a) Cross-section of the VC magnetic circuit structure, and (b) the physical dimensions to consider in the basic design.

#### 4.3.2.1. General VC design guide

The basic considerations and design steps will be very similar to those presented for the OMC system, but there are significant differences due to the steel circuit.

##### 1) **Environment:**

As with the OMC system, magnets are temperature sensitive, so high and low temperature environments may limit the choice of magnet material. Unlike the OMC system, the VC architecture does not influence the support structure material choice and is not impacted by mounting on or near ferromagnetic surfaces because the flux is contained in the low reluctance steel path.

##### 2) **Dimensional constraints:**

- a. **Overall size:** For a custom solution, the overall device size and expected motion will be determined by the environment, vibration source, power requirements of the application, and mounting. Ideally, the design target is a universal solution of compact size and high power output.
- b. **Support structure:** After settling on an overall size, the general support structure for the springs and housing should be defined because it may further restrict the size of the VC system.
- c. **Manufacturability:** The steel flux path adds manufacturing complexity, so machining choices may influence the minimum gap,  $l_m + l_a$ , in the steel structure and will also influence the overall cost and mass manufacturability of the design. Similarly, the dimensions of the steel such as  $h_c$ ,  $w_i$ , and  $w_o$  may drive manufacturing choices and cost while imposing limits on the space for coil turns.

- d. **Assembly:** Consideration should also be given to the assembly of the overall device as well as the steel-coil structure since the steel encloses the coil. Assembly procedures may further restrict or define the size of the VC system.
  - e. **Translation amplitude:** Determine the maximum translation amplitude so that proper offsets are built into the design to allow for the expected motion. The impact on the VC system is that the top of the steel flux circuit cannot collide with the springs or coil during normal operation. The translation amplitude further restricts the size of the VC circuit and coil. To simplify the analysis and guard against the steel circuit colliding with the coil, the top and bottom edges should not surpass the top and bottom edge of the magnet during operation. Imposing this limitation means the flux density can be approximated as constant for the whole coil.
  - f. **Tolerances and gaps:** Incorporate appropriate gap tolerances so that there are no interferences during device assembly and there is space to allow for the relative motion between the steel-magnet structure and coils. The area where coil turns can be placed will be further reduced by the gaps.
- 3) **Magnet size:**
- a. Custom magnet dimensions: Skip to 4.
  - b. Standard magnet sizes: Determine the set of magnets that satisfy the dimensional constraints imposed by the steel circuit. For standard magnet sizes, the set of magnets with appropriate dimensions may be small, especially for small overall device sizes.
- 4) **Evaluate the set of possible steel-magnet-coil configurations:**
- Evaluation can be carried out using an equivalent magnetic circuit method to determine the gap magnetic flux density or using a finite element analysis. Concerns over possible saturation in the steel circuit can make the finite element method more attractive.
- a. **Saturation:** The magnet dimensions may force a refinement of the dimensions of the steel circuit if saturation occurs. Generally, the only magnet dimension varying between analysis iterations will be  $l_m$ , so a set of acceptable dimensions can be found for the steel circuit such that saturation is not an issue over the range of  $l_m$  to be explored. Not having to modify the steel circuit for every magnet length simplifies the iterative evaluation process.
  - b. **Gap flux density curve:** From the equivalent magnetic circuit or finite element analysis, calculate the average gap flux density for the given magnet length and minimum gap,  $l_m + l_a$ . Calculate the average gap flux density for several points between the minimum and maximum allowable dimension for the gap,  $l_m + l_a$ , so that a curve fit can be generated.
  - c. **Coil configurations:** Determine the set coil configurations for the range of gap distances,  $l_m + l_a$ .
  - d. **Evaluation:** If an average gap flux density is assumed, it is simple enough to use the full set of differential equations to calculate the power generated for each coil configuration. Assume some appropriate harmonic motion, and a reasonable damping factor between 0.02 and 0.001. Approximate

the mass of the resonant system as the mass of the steel and magnet. A rough inductance can be calculated with the basic equivalent circuit analysis in section 3.2.2. Use the gap flux density curve to determine the power performance of the various configurations over the range of possible gaps,  $l_m + l_a$ .

- e. **Iterate:** Iterate through steps 4b to 4d for all the magnet sizes or range of magnet dimensions of interest, and pick the configuration from the set that generates the highest power.

#### 4.3.2.2. VC design case for the prototype

The overall size determined by H and W is more or less set by the design goals and constraints for the overall size of the device. Once the basic size is known, the task is to trade off the gap in the steel structure between  $l_m$  and  $l_a$  to get maximum power out of the device while maintaining enough thickness in the steel structure to avoid saturation. Since the magnet and steel are part of the resonant mass, the relative translation amplitude needs to be factored into the coil design. If the top or bottom edges of the coil approach or pass beyond the y-axis ends of the magnet, the approximation that all the coils see roughly the same magnitude flux density breaks down. For a given relative motion amplitude, an optimum coil can be designed using the method described for the open magnetic circuit analysis where summations are performed over the number of coil turns.

Ideally, the structures in figure 4.10 could be made practically such that the cross sections pictured could be revolved around the y-axis because the rotational symmetry would allow the whole length of the coil to be in the magnetic field. Several complications arise when considering that type of rotationally symmetric geometry. The first is that it would almost certainly require custom ring magnets that are radially magnetized. The second is that to avoid saturation of the steel associated with the inner radius,  $w_i$ , requires that that dimension be larger than is desirable for the small structures. The last complication for a rotationally symmetric design is how to fix the coils to the base simply when they are completely enclosed by part of the resonating structure. A rotationally symmetric design was briefly explored but quickly abandoned for practical reasons. As a result, the designs that were analyzed had cross sections like those in figure 4.10 that were then extruded out of the page to get the three-dimensional geometry. The result was that the coils have end-turns that are not in the magnetic field, causing added resistance while providing no induced voltage, but, for practical reasons, it made the design much simpler.

Similarly, a practical constraint was found for magnet dimensions. For small devices where W is roughly 10 mm or less, as was the case for the prototype, the trade-off between  $l_m$  and  $l_a$  runs into the practical reality of what magnet dimensions are readily available. Ultimately, in an effort to push for a small magnetic circuit size a magnet length,  $l_m$ , of 0.79 mm was chosen and used to carry out the analysis. The full magnet dimensions were 12.7 x 12.7 x 0.79 mm.

With the magnet chosen and the overall dimensions, H and W, defined, the next step was to analyze the structure and find the configuration that produced the highest theoretical power. The overall dimension of H was 19.05 mm, and 19.05 mm was the maximum allowable dimension for W. The dimensions of H and W were constrained by

the frame and by the travel of the resonant structure. While proposed designs could be analyzed using a more rigorous and complete equivalent magnetic circuit analysis than that introduced in chapter one, concerns about saturation led to basic design iteration using a finite element method that featured material properties for soft irons that included flux losses. The finite element method was only used to determine saturation and gap flux density.

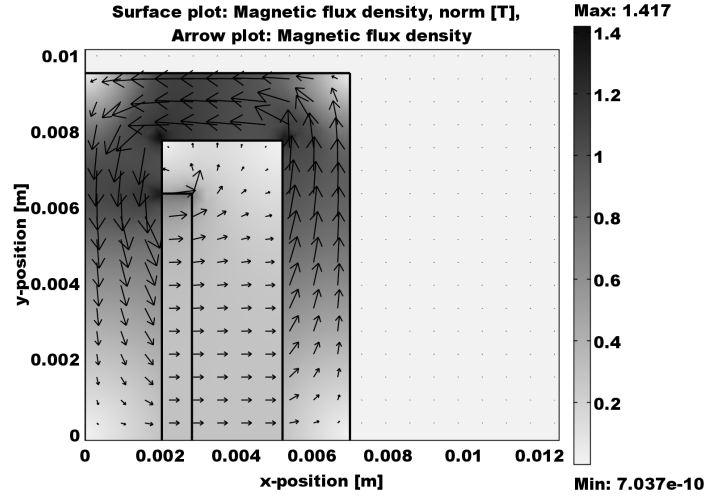


**Figure 4.11.** Quarter symmetry finite element analysis of a voice-coil magnet and steel configuration showing the magnetic flux density. The magnet is an N42 neodymium magnet. The arrows show the orientation of the magnetic flux density at their tail ends, and the arrow size is proportional to the magnitude of the field.

After finding dimensions for the steel structure that satisfied the saturation concerns for the range of possible air gaps,  $l_a$ , the gap flux density was simulated for several air gap lengths throughout the possible range. The steel structural dimensions were  $w_o = h_e = 1.78$  mm and the width of  $w_i$  was 2.03 mm. Those dimensions were settled on after iterating geometry and evaluating the effects of saturation. Using the trend shown in figure 4.12, a curve fit of the gap flux density with respect to gap length was generated and used to evaluate theoretical power outputs for the various coil configurations associated with each gap length. Thus, an optimum gap length was determined for the geometric design constraints.

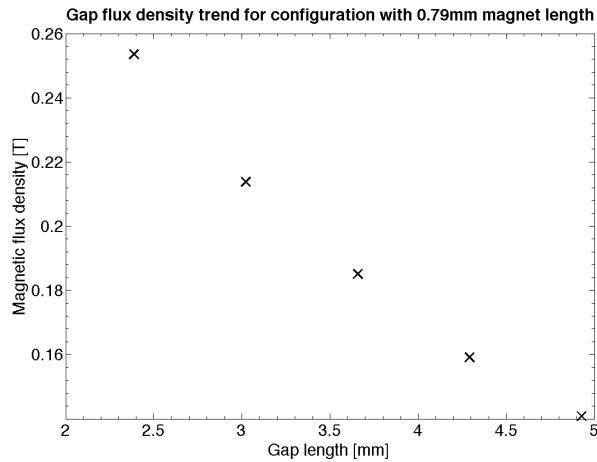


**Figure 4.12.** Average magnetic flux density trend for a range of air gap lengths,  $l_a$ .

The lower bound for the air gap length was set based on the manufacturability of the steel structural components. Ultimately, a prototype would be made, so having a theoretically optimal design that was difficult or impossible to make was undesirable. Interestingly, the optimal design was at the smallest practical gap length, about 2.4 mm.

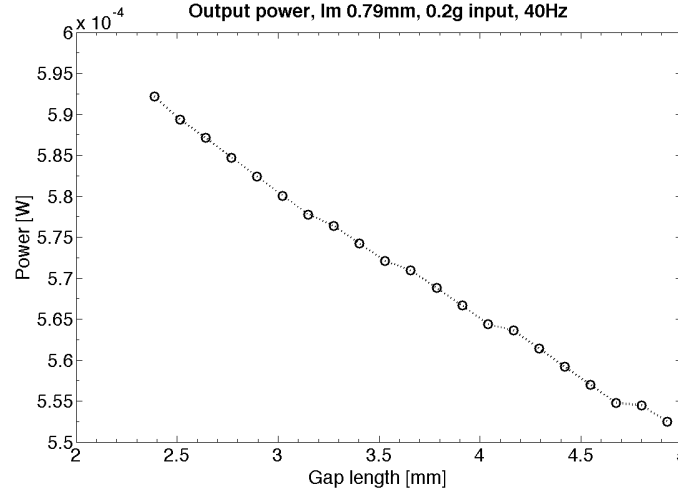


**Figure 4.13.** Theoretical power generated for the range of possible air gap lengths and the associated possible coil configurations

The simulation to calculate the power generated by the various coil configurations used the full set of equations presented in section 3.3. The inductance was approximated using the equivalent circuit method in section 3.2.2, and a conservative damping factor of 0.02 was used.

#### 4.4. Additional design constraint: Voltage

The OMC and VC prototype designs were evaluated solely on power generation potential, but for more realistic electrical loads than a simple resistor such as rectification circuitry, the output voltage becomes an additional constraint on the design. Rectification circuitry becomes significantly simpler and more efficient for voltages greater than one volt. Rectifying lower voltages is possible but the losses are greater [59][60]. The voltages produced by the OMC prototype were in excess of a volt for conditions consistent with industrial vibrations, but the VC prototype regularly generated voltages below one volt. The low voltages from the VC prototype led to the exploration of designs with the potential for higher gap flux densities.

Voltage improvements can generally be achieved by increasing the number of coil turns a device has or by increasing the magnitude of the gap magnetic flux density. Adding more coil turns can be achieved with smaller gauge wire or by increasing the gap length to accommodate more coil turns. Increasing the gap length to get more coil turns may mean sacrificing power for additional voltage. Power was a primary design goal, but it is useless if it cannot be rectified. Thus a minimum voltage constraint needs to be added to the set of design goals.

## 4.5. Possible improved magnetic circuits

The designs presented in this section are proposed as possible architectures that could produce significantly higher gap flux densities than those of the open magnetic circuit and voice-coil designs. Initial simulations indicate gap flux densities for practical geometries could possibly approach one tesla, which is standard for commercial motors and electromagnetic devices.

The initial results shown for the two proposed designs used the basic geometric and practical magnet dimension constraints that were used in the voice-coil design case, but a full design analysis was not carried out. The goal was simply to see the possible improvements in gap flux density. The next steps would be to find the best gap length based on the set of design constraints chosen.

### 4.5.1. Coreless DC motor architecture

The basic structure is shown in figure 4.14. The design is made up of two structures comprised of two oppositely energized magnets side by side bonded to a low reluctance backing plate. The structure has previously been proposed for vibration harvesting by Glynn-Jones et al. in [61]. The reported gap flux densities in [61] suggest that there is room for improvement.

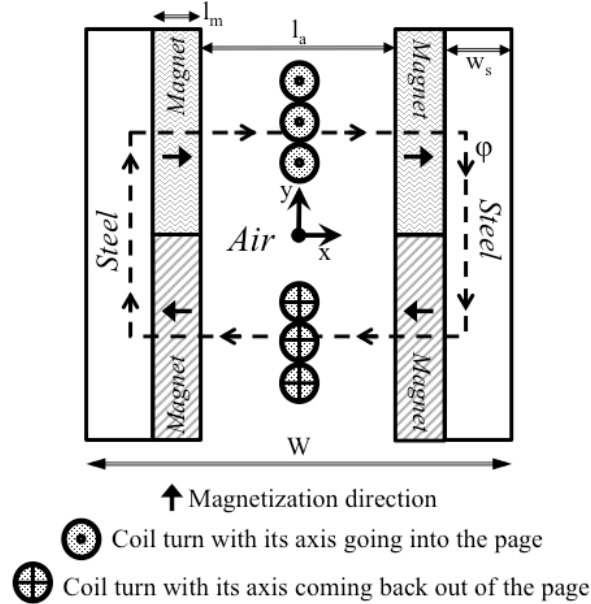


**Figure 4.14.** Cross-section of the basic structure and flux loop for the coreless DC motor-inspired magnetic circuit architecture.

Figure 4.14 just shows the magnet circuit components, and additional structural components are necessary to span the overall width,  $W$ , to maintain the air gap,  $l_a$ . That structural component resists the attractive force between the magnets on either side of the gap. This force could be quite large, especially for high gap flux densities. Using a non-ferromagnetic material for the spanning component increases the gap flux density because it eliminates the short circuit flux leakage paths that arise if the component is steel.



Except for the additional structural and dimensional considerations associated with the spanning component mentioned above, the design considerations and steps should be the same as those for the voice-coil design. A rough assessment design and simulation of the magnetic circuit was done to determine the possible potential gap flux density improvements for this type of architecture. The overall dimensional constraints on H and W were the same as those used for the OMC and VC prototypes. Similarly, only standard magnet sizes were considered. Figure 4.15 shows the finite element simulation results with the maximum allowable gap,  $l_a$ .

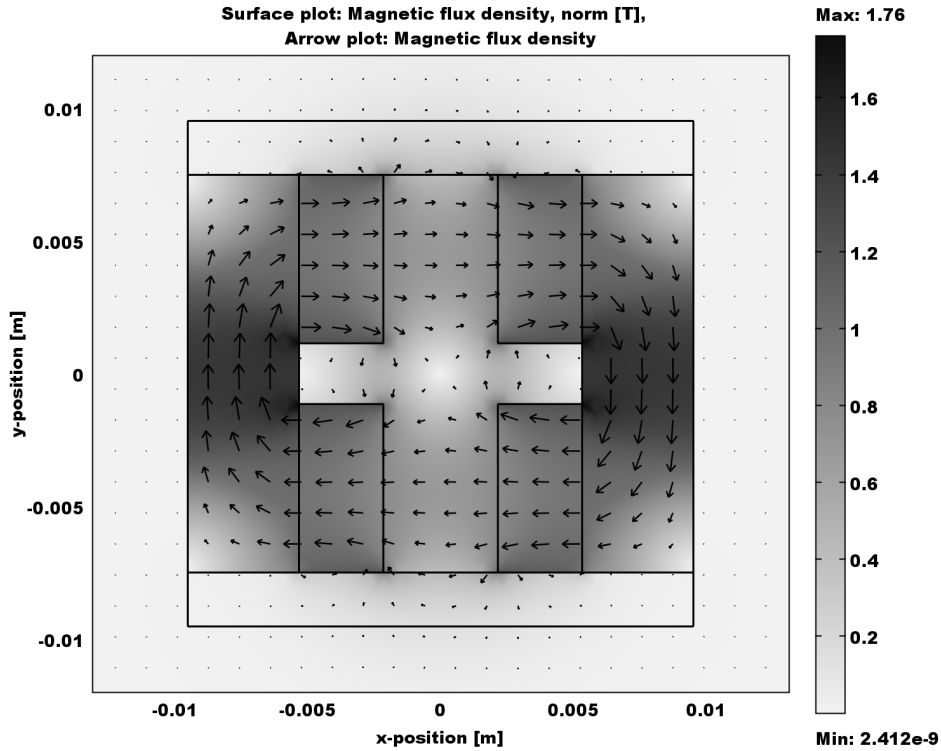


**Figure 4.15.** Assessment simulation for possible higher gap flux densities using a coreless DC motor-inspired magnetic circuit. The magnets were N52 neodymium, and the gap length was 4.32 mm. The magnets were 6.35 x 3.18 x 12.7 mm. The arrows show the orientation of the magnetic flux density at their tail ends, and arrow size is proportional to the magnitude of the field.

Even with the largest allowable gap length of 4.32 mm, given the other constraints on magnet dimensions and saturation, the average gap magnetic flux density was 0.61 T. For the VC prototype, the gap flux density was about 0.25 T, so it seems there is the possibility to increase the gap flux density significantly. The higher gap flux density would also increase the induced voltage proportionally, assuming that the gap length allowed for the same number of coil turns.

#### 4.5.2. Halbach array architecture

A Halbach array uses magnetic material or an array of magnets to steer the magnetic flux to create a loop instead of using low reluctance material. The advantage is that a larger volume of magnetic material is used while maintaining the ability to orient the flux such that the vector interactions in Lorentz's and Faraday's laws are optimal. The

basic layout of the Halbach array-inspired magnetic circuit is very similar to the DC motor-inspired circuit in section 4.5.1 except there are two additional magnets, and there is essentially no low reluctance material.

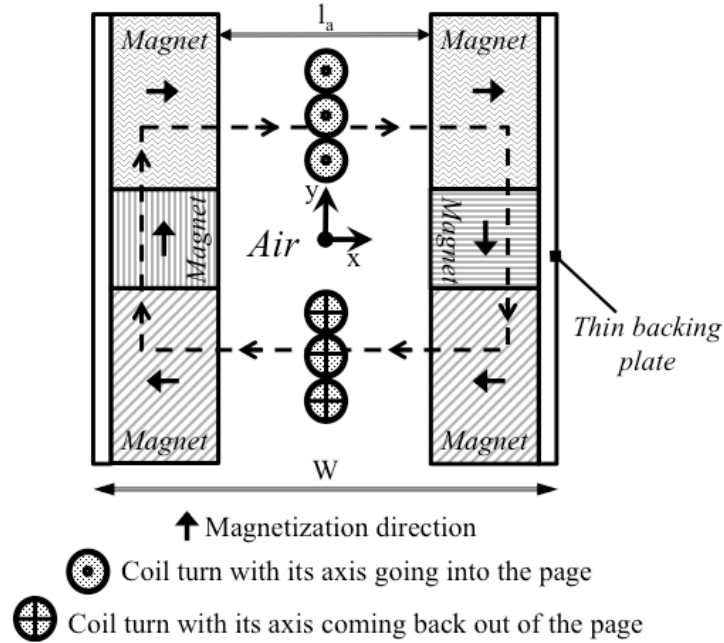


**Figure 4.16.** Cross-section of the Halbach array-inspired magnetic circuit structure

As discussed with the DC motor-inspired structure in the previous section, a structural component spanning  $W$  needs to be given consideration and will impact the space for the magnetic circuit. As before, the component spanning  $W$  should be non-ferromagnetic to minimize short circuit flux leakage paths. The thin backing plates shown in figure 4.16 are bonding surfaces for the magnets, but if they are made from steel or iron the gap flux density increases slightly. The design considerations and steps are basically the same as those presented for the voice-coil design except saturation is not a significant concern. The larger magnets and gap flux densities will require verifying that there is enough strength and stiffness in the structural components reacting the moments and attractive forces of the magnets before finalizing a design.

Assembling and bonding the Halbach-type magnet configuration will require some care because it is not a naturally stable configuration. The addition of the magnet in the middle causes unbalanced magnetic moments that will have to be dealt with during assembly. Similar to the DC motor-inspired design, the attractive force between the two halves will be quite high, only more so since there is more magnetic material and higher gap flux densities.

Standard magnet sizes were used in the assessment simulation, and the overall dimensional constraints on the magnetic circuit from the VC prototype case were used. The results from the assessment simulation are for the largest allowable gap given the dimensional constraints and magnets choices, so to get to an optimum design, the gap length would be varied over its allowable range while evaluating the expected device performance.

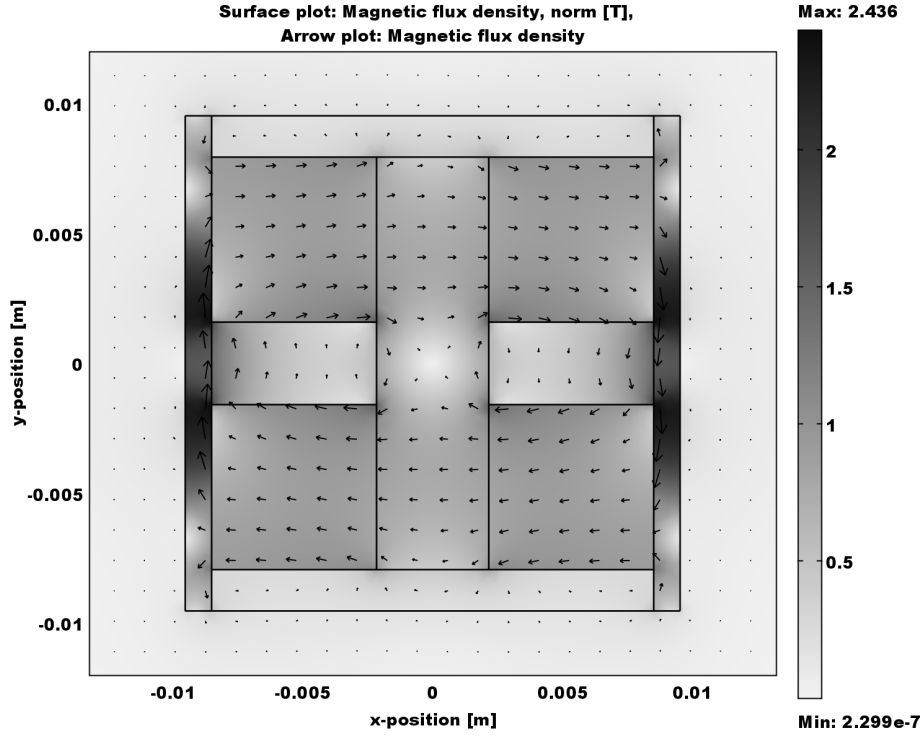


**Figure 4.17.** Assessment simulation for possible higher gap flux densities using a Halbach array-inspired magnetic circuit. The end magnets were N42 neodymium, and the center magnets were N52 neodymium. The end magnets were 6.35x6.35x12.7 mm, and the center magnets were 3.18x6.35x12.7 mm. The gap length was 4.32 mm. The arrows show the orientation of the magnetic flux density at their tail ends, and arrow size is proportional to the magnitude of the field.

The average gap flux density for the Halbach assessment simulation was 0.71 T. With the same dimensional constraints, practical constraints, and gap length of 4.32 mm, the gap flux density for the Halbach-inspired design is about 0.1 T higher than that simulated for the DC motor-inspired architecture. Both appear to be capable of producing gap flux densities that are considerably higher than those observed in the VC prototype where the gap flux density was about 0.25 T with a gap length of 3.2 mm.

Even though the Halbach-inspired design has more parts and is more complex and difficult to assemble, the potentially high gap flux densities make it attractive for vibration harvesting. The high gap flux densities would increase the induced voltage, making rectification of any harvested power easier.

## Chapter 5. Device characterization

### 5.1. Vibration platform

An electrodynamic vibration platform (colloquially henceforth described as a shaker) controlled with Labview was used to simulate vibrations. The system was capable of simulating or reproducing both ideal sinusoidal vibrations and real acceleration signals that had been measured. As can be seen in figure 4.1, a 1.8 kg block of aluminum was added to the shaker to increase the input or base mass to provide enough inertia for the resonant mass of the harvesters to react against without impacting the overall driving motion of the shaker. A Kistler  $\pm 2$  g capacitive accelerometer with a 1 kHz bandwidth was used to measure the input acceleration, and it was also used in a feedback loop to control acceleration. A Keyence LKH-087 laser displacement sensor was used to measure the displacement of the resonant mass, allowing the resonant amplification or Q of a device to be directly measured. The induced current was determined by measuring the voltage drop across a 10 ohm series resistor with an instrument op-amp chip. The resistive load seen by the harvester was varied with a resistor box. The measured acceleration, voltage, and current signals were all buffered before going into a Labworks USB DAQ to eliminate any possible charge buildup on the input channels when high sampling frequencies were used. The noise floors for the system were 0.5 mV, 3  $\mu$ A, and about 8 milli-g's for the voltage, current, and input acceleration measurements, respectively.

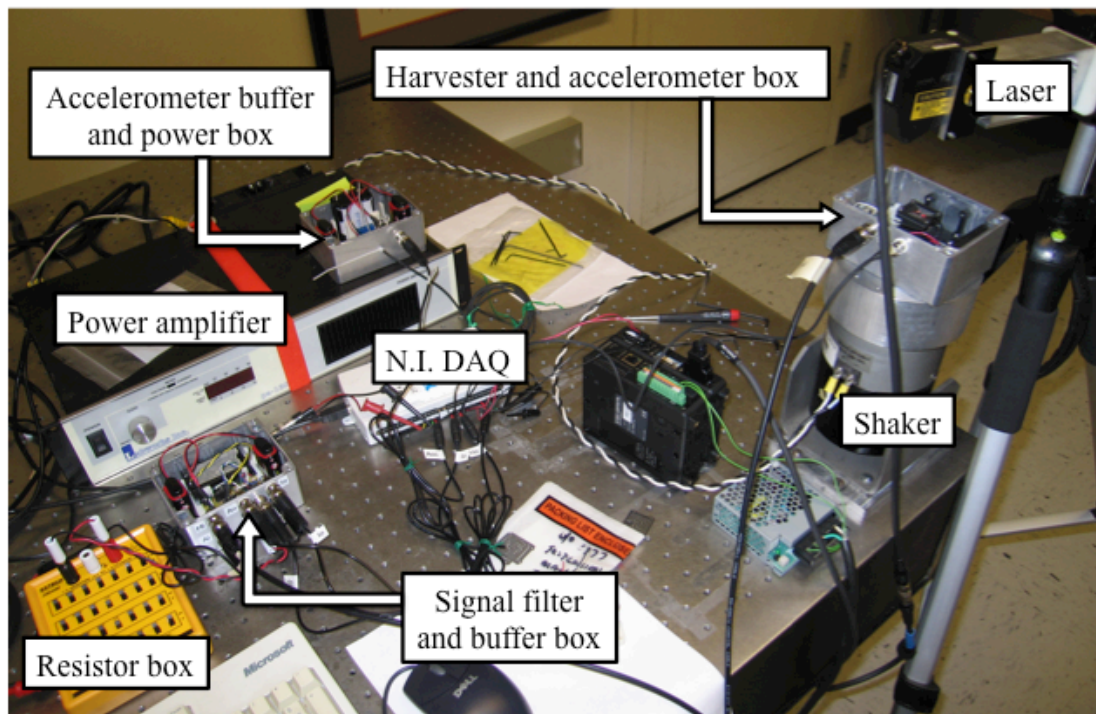


**Figure 5.1.** Electrodynamic shaker setup and signal acquisition electronics used to evaluate vibration harvesters.

The Labview programs controlling the shaker also recorded data from the accelerometer, harvester, and laser displacement sensor. The programs recorded input frequency, input acceleration amplitude, power, RMS current, RMS voltage, and amplification, also referred to as Q.

## 5.2. Prototype parameters

### 5.2.1. Resonant springs

A three-link spiral spring was used to achieve the relatively low target resonant frequencies for the OMC and VC prototypes. To change the resonant frequency quickly, different thickness springs could be installed. The planar geometry remained the same for the range of thicknesses. High strength annealed 17-4PH stainless steel was used to fabricate the springs to mitigate fatigue issues. The springs were fabricated by chemical etching. The outer edges of the springs were roughly 25 mm square, and the different thicknesses were 0.08 mm, 0.13 mm, 0.25 mm, 0.30 mm, 0.38 mm, and 0.51 mm.

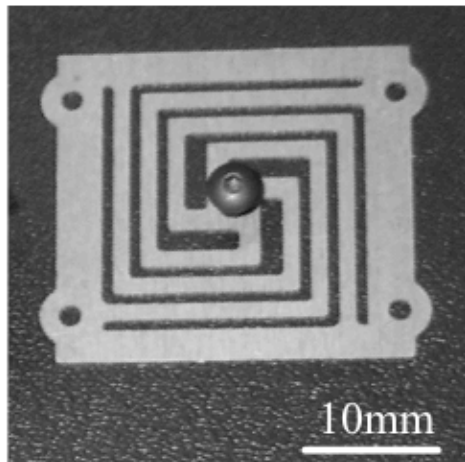


**Figure 5.2.** Stainless steel resonant spring that is 0.51 mm thick.

### 5.2.2. Open magnetic circuit (OMC) prototype

The pieces of the OMC harvester are shown in figure 5.3. The frame was made with fuse deposition ABS plastic, and its fundamental resonant frequency was over 1 kHz, which was far enough from the desired transducer resonant frequency range of 40-150 Hz that excitation of the frame was ignored. The caps on the ends of the magnet are aluminum, and non-austenitic stainless steel 2-56 fasteners thread into the caps clamping the center of the springs at either end of the magnet-cap structure. The outer edges of the springs are clamped with an ABS piece secured with 0-80 fasteners. The coil was made from 0.1 mm diameter magnet wire. Only one of the two coils was fabricated to evaluate the design.

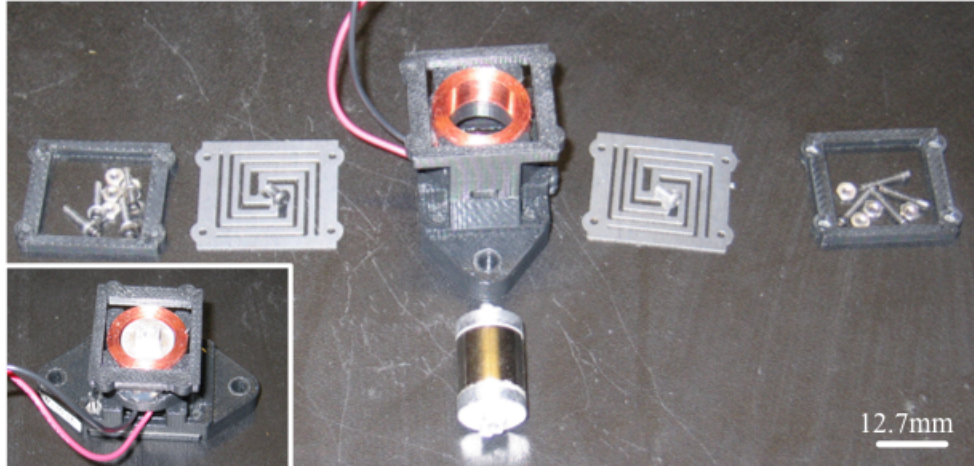


**Figure 5.3.** OMC prototype

The physical parameters of the prototype OMC system corresponding to the design case in section 3.5.1 are summarized in table 5.1. The parameters were used to evaluate the model presented in section 3.3 when characterizing the device on the shaker with harmonic input motion.

**Table 5.1.** OMC prototype parameters

Parameter	Value
# of coil turns, $N$	1530
Coil packing efficiency	72%
Mass of resonant system, $m$ [kg]	0.019
Coil resistance, $R_c$ [ohms]	168
Self-inductance, $L$ [mH]	33.4
Average flux density, $B$ , @ rest [T]	0.178*
Average length of a coil turn, $l_w$	0.0511*
	*simulated or calculated

### 5.2.3. Voice-coil (VC) prototype

The pieces of the VC prototype are shown in figure 5.4. The basic layout is the same as that for the OMC prototype, with springs clamped to the top and bottom of the magnetic circuit. The steel magnetic circuit has two parts. An inner part shaped like a capital T with the magnets bonded to either side of the column of the T. The inner T-shaped part fits into the outer U-shaped part. It is a very close slip-fit so that it maintains the proper shape and so that there are no gaps in the magnetic circuit. One of the fasteners clamping the center of one of the springs goes through the U-shaped part and threads into the base of the T-shaped part, thus securing the two pieces of the magnetic circuit. The T- and U-shaped parts are assembled around the coil that is wound onto the base frame. As with the OMC prototype, the frame is ABS plastic and 0.1 mm magnet wire was used for the coil.



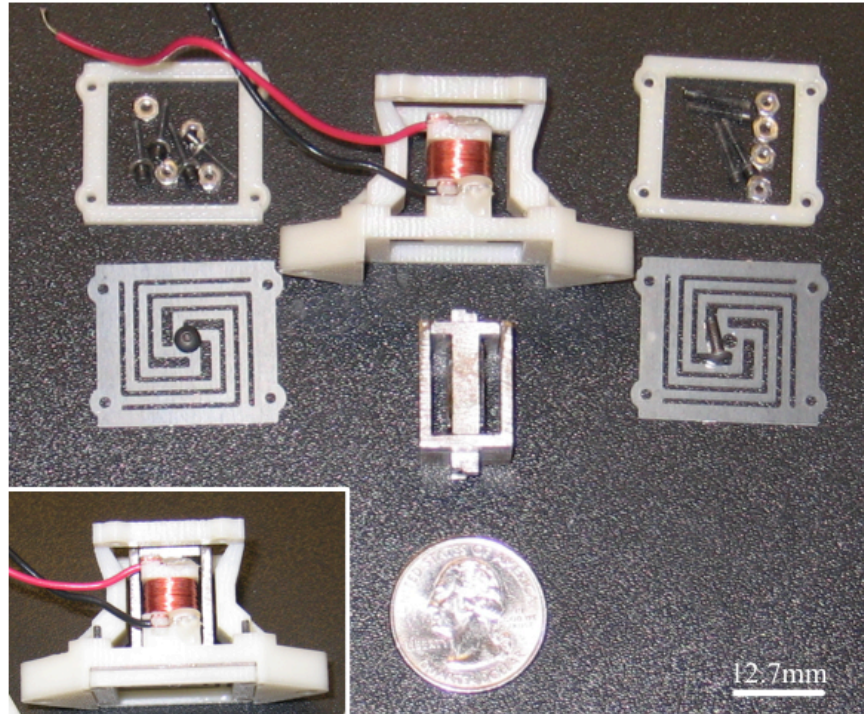


**Figure 5.4.** VC prototype

The physical parameters of the VC prototype are summarized in table 5.2.

**Table 5.2.** VC prototype parameters

Parameter	Value
# of coil turns, $N$	660
Coil packing efficiency	60%
Mass of resonant system, $m$ [kg]	0.027
Coil resistance, $R_c$ [ohms]	76
Self-inductance, $L$ [mH]	50
Average flux density, $B$ , @ rest [T]	0.25*
Average length of a coil turn, $l_w$	0.0254
	*simulated

### 5.3. Vibration platform evaluation of prototypes

The evaluations were performed with a sinusoidal input acceleration with a peak amplitude of 0.1 g or  $0.981 \text{ ms}^{-2}$ . Each prototype was evaluated for two spring thicknesses. Thinner springs were used to show performance at the low end of the target frequency range, 40-60 Hz, and thicker springs were used to show performance at the high end of the target frequency range, greater than 100 Hz.

### 5.3.1. OMC evaluation

With 0.30 mm thick springs, the OMC prototype resonated at about 58 Hz. The resonant frequency was initially found by recording the impulse response of the harvester and performing an FFT. Frequencies on either side of the result from the FFT impulse response were swept to determine the bandwidth and verify the actual resonant frequency. The shaker was stopped between frequency steps to eliminate dynamic sweep effects. A relatively low load resistance was used during initial sweeps trying to confirm the resonant frequency. A low load resistance allows for higher induced currents, so the Lorentz force is higher, reducing the resonant motion. Effectively, the lower resistance makes controlling the resonant system slightly easier. An initial load resistance of 1510 ohms was used to confirm the resonant frequency near 58 Hz.

With the resonant frequency confirmed, the load resistance was varied while forcing the device at its resonant frequency. The optimum load occurs when the maximum power is transferred to or, in this case, dissipated in the load resistor. If the Lorentz force is considered to act as a damping force, as in [26], [51], [62], and others, then the optimum load causes the transduction damping to equal the mechanical and parasitic damping for the system, assuming linear spring stiffness [54]. Since  $Q$  is measured by comparing the accelerometer and laser sensor readings, the mechanical damping,  $\zeta$  in section 3.2, can be estimated as

$$\zeta = \frac{1}{2Q}, \quad (5.1)$$

where  $Q$  is the measured motion amplification due to resonance. The  $Q$  of just the mechanical system was measured by driving the harvester while maintaining an open electrical circuit so that there was no Lorentz force. This open-circuit measurement could be compromised if the translation was large enough for mechanical hardening or nonlinear spring effects to occur. Similarly, the mechanical  $Q$  under operating conditions could be estimated by multiplying the  $Q$  in equation 5.1 by two, using the fact that mechanical and transduction damping should be equal for optimum electrical load conditions. Therefore, the mechanical  $Q$  was approximated to be twice the measured  $Q$  under optimal electrical load conditions for a system with a linear spring stiffness.

For the low end of the target frequency range, the translation amplitudes were large enough to cause nonlinear stiffness in the springs, causing the basic model to inaccurately represent the experimental results. As can be seen in figure 5.5, the same nonlinear spring effects were observed at low frequencies for the VC prototype as well, but the VC system shows the characteristic frequency response for a system with a nonlinear stiffness. The effect is muted in the OMC system, but still present. The power-versus-frequency curve for a linear system is symmetric about the resonant frequency, but for nonlinear systems, higher than expected power will be generated on one side of the resonant frequency until a sudden drop back to the linear power curve occurs at a frequency sufficiently far from the resonant frequency that the phenomenon cannot be excited.



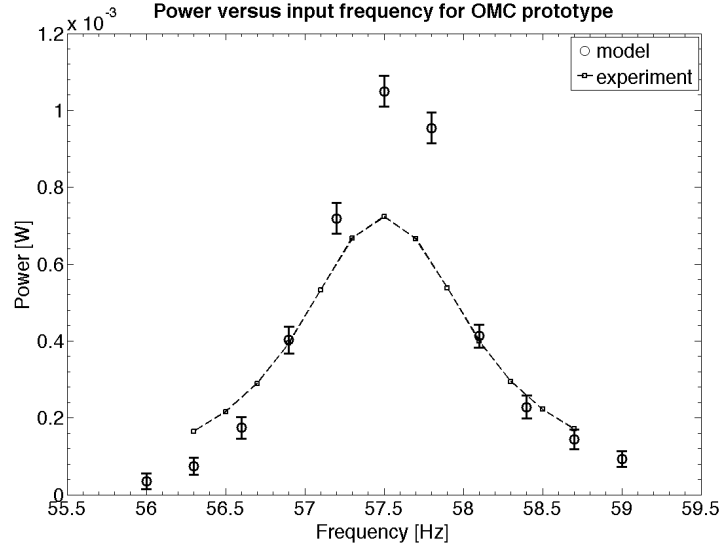


**Figure 5.5.** OMC frequency sweep around the resonant frequency with a 0.1 g input acceleration amplitude and a 4010 ohm load resistance. The mechanical damping factor used in the model was 0.0036, and it was backed out from the measured Q under optimal electrical load conditions. The deviation from the model was due to the spring stiffness becoming nonlinear for the larger translation amplitudes at lower frequencies.

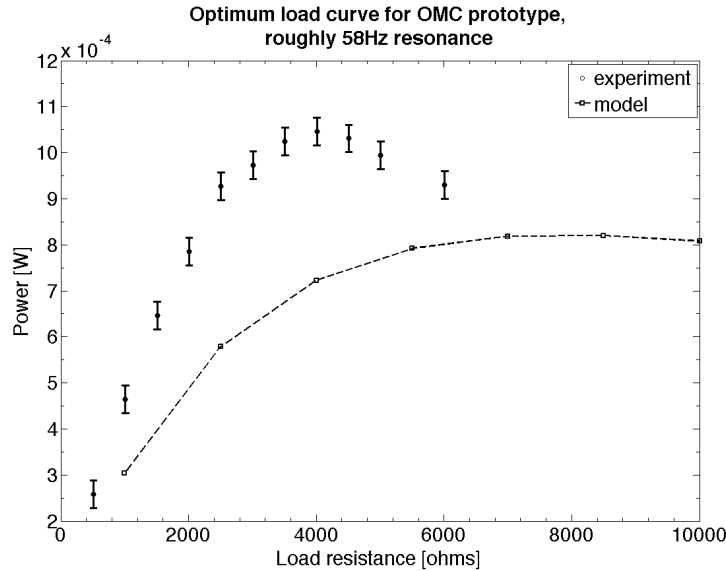


**Figure 5.6.** Optimum load evaluation for OMC prototype at resonance of 57.5 Hz with an input acceleration amplitude of 0.1 g

The OMC prototype generated about 1.1 mW at the optimum experimental load of 4010 ohms. The RMS voltage across the load resistance was about 2.0 V, and the RMS current was about 0.51 mA.

The beam nonlinearity trend was confirmed, as can be seen in table 5.3, by determining the Q of the device with an open electrical circuit for several input acceleration amplitudes.

**Table 5.3.** Mechanical Q of OMC prototype with 57.5 Hz resonant frequency

Frequency [Hz]	Acceleration amplitude [g's]	Translation amplification, Q
57.5	0.025	217
57.5	0.049	144
57.5	0.099	88

The amplification and associated mechanical damping were changing dramatically with input acceleration even for very low input accelerations, so the model breaks down at the low end of the frequency range for the chosen spring geometry. A nonlinear stiffness would need to be incorporated into the model to more accurately represent the lower frequency performance of the harvester with this three-link beam spiral spring geometry. Alternatively, a spring geometry with more links in the spiral pattern could be designed so that the stiffness was linear over the desired displacement range.

The spring nonlinearity causes the optimum load to be lower than expected, possibly because the translation becomes restricted. Consider the worst-case scenario where the system collides with a hard mechanical stop. The stiffness essentially becomes very nonlinear. For this case, the optimum electrical load seems to be lower than expected because the increased Lorentz force associated with the lower load resistance limits or eliminates the collision, effectively keeping the resonant system moving regularly. This regular motion possibly leads to higher velocities than the case where collisions are allowed to occur, increasing the induced voltage from Faraday's law. Similarly, any nonlinear hardening effect would shift the resonant frequency, but further work is necessary to confirm or characterize this speculative explanation.

At the high end of the frequency range, the stiffness for the springs was essentially linear. Thus, the basic model matched the experimental data reasonably well, as seen in figures 5.7 and 5.8, and the standard symmetrical resonant behavior was observed. The OMC prototype resonated at about 131 Hz with 0.51 mm thick springs installed. The mechanical damping factor of 0.0011 was calculated from the Q with the optimum load resistance.

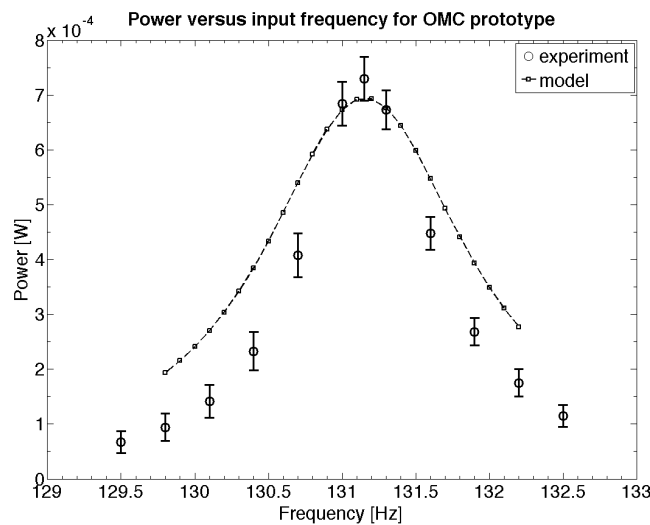


**Figure 5.7.** OMC frequency sweep around resonant frequency with 0.51 mm thick springs. The input acceleration amplitude was 0.1 g and a 2510 ohm load resistor was used. The mechanical damping factor, 0.0011, was calculated from the Q under optimal load conditions.

At resonance, the model and experimental powers are within 6% of one another. The experimental resonant power at the optimum load resistance of about 9000 ohms was about 1.1 mW. The RMS voltage across the load resistance was about 3.2 V, and the RMS current was about 0.36 mA.

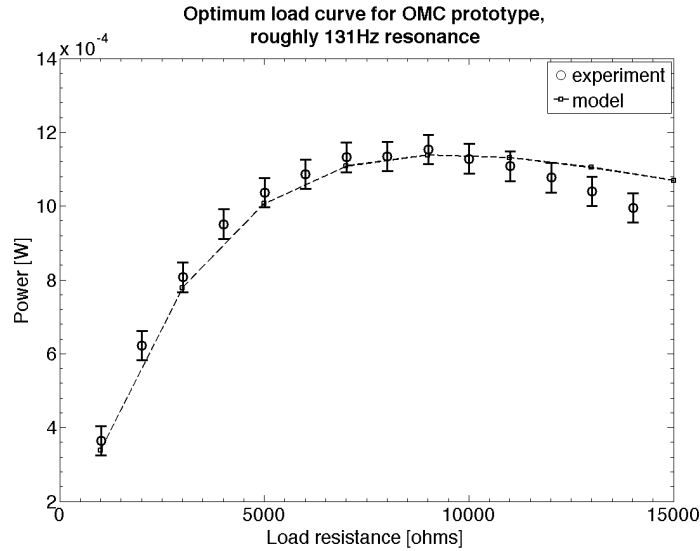


**Figure 5.8.** Optimum load evaluation for OMC prototype with 131.15 Hz resonant frequency and an input acceleration amplitude of 0.1 g.

The mechanical  $Q$  was also evaluated using the laser sensor and input accelerometer with an open electrical circuit condition. Table 5.4 shows that the change in  $Q$  is not as drastic as the 58 Hz case. With a normal electrical load, the translation amplitude is in the linear range for the spring.

**Table 5.4.** Mechanical  $Q$  of OMC prototype with 131.15 Hz resonant frequency

Frequency [Hz]	Acceleration amplitude [g's]	Translation amplification, $Q$
131.15	0.025	512
131.15	0.050	481
131.15	0.100	307

The results of the experimental characterization of the OMC prototype show that the device can be made to resonate at both the high and low ends of the target frequency range. The prototype generated over 1 mW at 58 Hz and 131 Hz for a sinusoidal input vibration signal with an acceleration amplitude of 0.1 g. A nonlinear spring stiffness at lower frequencies caused the basic model to break down, but the model accurately represented the experimental data at higher frequencies where the spring stiffness was more linear. Further work is needed to determine whether the nonlinear stiffness improves or degrades performance.

One major drawback for the OMC prototype was that it cannot be mounted on or very near a steel or iron surface. The attraction between the magnet and a ferromagnetic surface caused it to pull down to the bottom travel limit, effectively killing the generator because no relative motion could be induced. This problem could be eliminated by maintaining a proper standoff distance from any iron surface, but that would increase the overall size of the device. So the OMC design may only be attractive in specific

situations, but it is not a universal solution, especially since most deployments in industrial settings will be on or near large iron surfaces.

### 5.3.2. VC evaluation

The VC prototype was also evaluated using a 0.1 g sinusoidal input acceleration amplitude. With 0.25 mm thick springs installed, the prototype resonated at about 41 Hz. Just like the OMC prototype, the springs exhibited nonlinear stiffness at this low frequency, but as figure 5.9 shows, a more characteristic hardening stiffness behavior was observed [63].

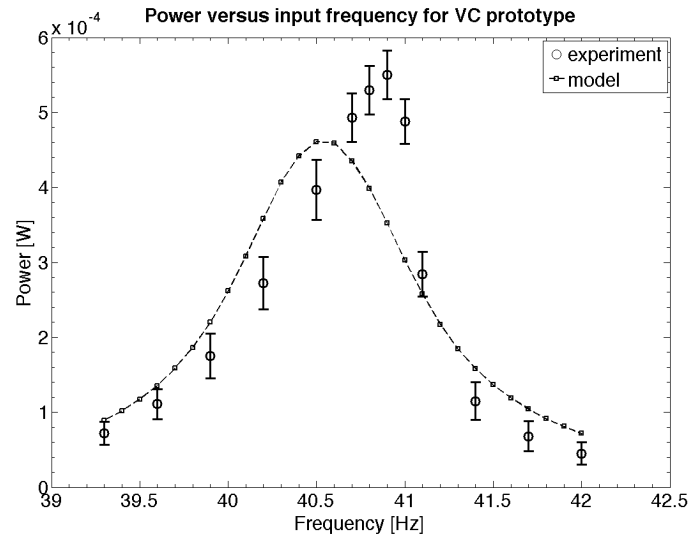


**Figure 5.9.** Frequency sweep around the resonant frequency for the VC prototype. A 0.1 g input acceleration amplitude and a 50 ohm load resistance were used. The mechanical damping factor used in the model was 0.005, and it was backed out from the measured Q under optimal electrical load conditions.

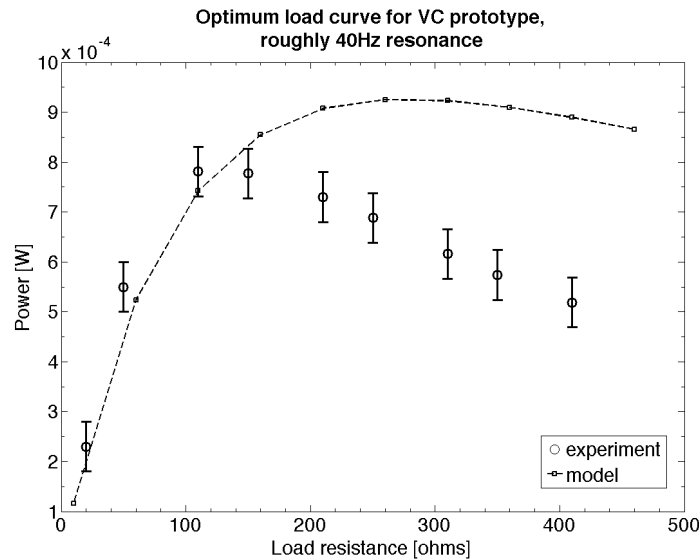


**Figure 5.10.** Optimum load evaluation of VC prototype with a 40.5 Hz resonant frequency. The evaluation was done with a 0.1 g input acceleration amplitude.

The nonlinear behavior was essentially the same as that of the OMC prototype at 58 Hz. Table 5.5 shows how the mechanical Q changed with input acceleration amplitude.

**Table 5.5.** Mechanical Q of VC prototype with a 40.5 Hz resonant frequency

Frequency [Hz]	Acceleration amplitude [g's]	Translation amplification, Q
40.85	0.026	177
40.85	0.050	98
40.85	0.100	54

Due to the nonlinear behavior, the experimental maximum power was about 1 mW at 41.1 Hz with a 110 ohm load resistance. The RMS voltage across the load was 0.33 V, and the RMS current was about 3 mA. As figure 5.10 shows, the nonlinear stiffness shifted the optimum load to be lower than expected as was observed with the OMC prototype at 58 Hz. This shift in the optimum load curve could be compensation for restricted motion due to the nonlinearity, as was discussed in the OMC evaluation section.

As with the OMC prototype, the springs had a linear stiffness for the smaller translation amplitudes at higher frequencies, and typical resonant behavior was observed. With 0.51 mm thick springs installed, the VC system resonated at 108.85 Hz.

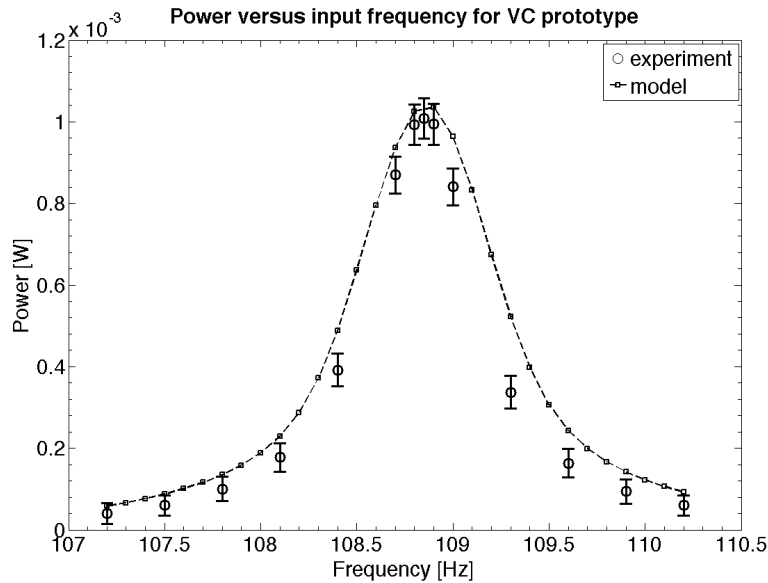


**Figure 5.11.** Frequency sweep for the VC prototype around the 108.85 Hz resonant frequency with 0.51 mm thick springs installed. An input acceleration amplitude of 0.1 g was used, and the electrical load was a 90 ohm resistor. The mechanical damping factor used in the model was 0.0009, and it was backed out from the measured Q under optimal electrical load conditions.

The model accurately simulated the experimental data with less than a 5% deviation in generated power between model and experiment at resonance when the spring stiffness was linear. The VC prototype generated about 2 mW with an optimum load of 350 ohms. The RMS voltage across the load resistance was 0.83 V, and the RMS current was 2.3 mA.

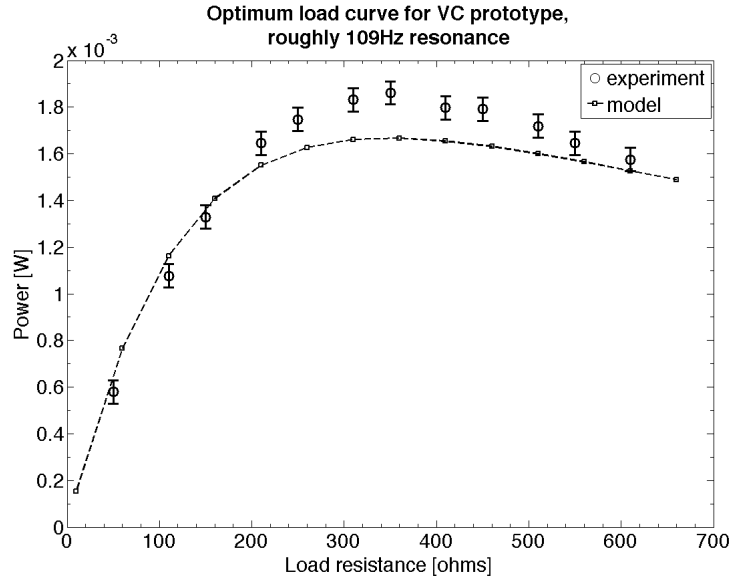


**Figure 5.12.** Optimum load evaluation of VC prototype with a 108.85 Hz resonant frequency. The evaluation was done with a 0.1 g input acceleration amplitude.

The results of the experimental characterization of the VC prototype show that the device architecture can be made to resonate at both the high and low ends of the target frequency range. The prototype generated almost 1 mW at 41 Hz and almost 2 mW at 109 Hz for a sinusoidal input vibration signal with an acceleration amplitude of 0.1 g. The model accurately represented the experimental data at higher frequencies where the spring stiffness is linear, but it broke down at lower frequencies because the spring stiffness became nonlinear.

### 5.3.3. Summary of experimental characterization of prototypes

The experimental results of the characterization are summarized in table 5.6. For higher resonant frequency configurations, the analytic analysis for each system modeled the experimental data accurately, but for lower frequencies the models became inaccurate because the springs became nonlinear.

**Table 5.6.** Summary of experimental prototype performance evaluated with a sinusoidal 0.1 g input acceleration amplitude signal

OMC prototype			
Frequency [Hz]	Power [mW]	RMS voltage [V]	RMS current [mA]
57.5	1.05	2.04	0.51
131.15	1.14	3.17	0.36
VC prototype			
41.1	0.97	0.33	2.96
108.9	2.00	0.84	2.39

Creating a model that included spring nonlinearities is possible, as [64] and others have shown. Practically, the only reason to use nonlinear springs is for situations where more bandwidth is needed. Using nonlinear springs appears to limit the amount of power

that can be generated because the resonant motion is restricted. The nonlinearity observed in the prototypes suggests that a spring structure with more beam links in the spiral are needed, allowing more translation while maintaining a linear stiffness.

The evaluated OMC and VC prototypes can be compared to the vibration harvesters reviewed in chapter 2 in terms of power density. The prototypes were each 18 cm<sup>3</sup>. Table 5.7 adds the experimental evaluations of the prototypes to table 2.1. Since only one of the two coils was fabricated for the OMC prototype, the power for the power density calculation was assumed to be double as a rough approximation. Even with harvesters that are not fully optimized but only intended to show proof of concept, the experimental power densities are on par with what is commercially available. The major drawbacks are the low output voltages for the VC prototype and the strong magnetic attraction force observed when mounting the OMC prototype near a steel structure.

**Table 5.7.** Normalized power for vibration harvester using electromagnetic transduction

Author, Reference	Frequency [Hz]	Acceleration [g]	Size [cm <sup>3</sup> ]	Power density [mW•cm <sup>-3</sup> •g <sup>-2</sup> ]
Amirtharajah, [47]	2	0.3	24	0.19
Lee, [48]	85	4.3	7.3	0.0061
Waters, [49]	50-60	0.1	27	4.44
El-hami, [51]	322	5.0	0.84	0.0019
Beeby, [52]	350	0.3	0.06	0.56
Perpetuum, [28]	100	0.1	131	2.67
Ferro-solutions, [28]	60	0.1	133	8.12
<b>OMC prototype</b>	58	0.1	18	<b>11.67</b>
<b>OMC prototype</b>	131	0.1	18	<b>12.67</b>
<b>VC prototype</b>	41	0.1	18	<b>5.39</b>
<b>VC prototype</b>	109	0.1	18	<b>11.11</b>

## Chapter 6. Applications to asset monitoring

---

Three real world or simulated deployments were done using the VC prototype to evaluate the performance of the harvester with real input vibrations. Only the VC prototype was used because most of the deployments were on large iron structures that were problematic for the OMC prototype, as discussed at the end of section 5.3.1. The goal was also to target potentially high value applications where the installation of a wireless sensor is potentially compelling; applications associated with condition monitoring of industrial equipment, improving productivity, and asset monitoring were targeted. The first deployment was on large industrial pump motors in the Nanolab machine room in Sutardja Dai Hall on the UC Berkeley campus. The second deployment assessed harvesting machine tool vibrations associated with metal cutting and rapid axis motion. The third and last deployment was aimed at trying to harvest unsprung vehicle suspension vibrations. In each case, harvester performance was evaluated simply by dissipating the induced power in a load resistance.

Obviously, the VC prototype was not optimized for any particular vibration situation, but it was used as a benchmark for showing what is possible. Revised or fully optimized designs would almost certainly have improved performance over that reported in this chapter. The deployments spanned a frequency range of 10-120 Hz, so for the lower frequency configurations, the spring nonlinearities are present. Otherwise, future designs could evaluate their performance using a slightly modified form of the model presented by Miller et al. in [65]. That model has the same basic form as the model in chapter three, but it has been modified to accept random or measured acceleration inputs. It also assumes a linear spring behavior.

### 6.1. Large industrial motor deployment

Three large industrial pump motors running support systems for the microfabrication equipment in the UC Berkeley Nanolab were identified as possible assets that might be found in industry where there could potentially be added value from condition monitoring sensors. The added value would be realized by eliminating unscheduled down time and only doing maintenance when necessary, as indicated by the sensors. Beyond scheduled down time, condition monitoring eliminates failures that could lead to damaging very expensive microfabrication equipment or ruining a fabrication run. The conditioning monitor could be as simple as an accelerometer, but it could include other sensors. Large motors always have some level of vibration associated with them, so surveys of the vibration spectrum of each motor were carried out. Target frequencies from the surveys were then harvested using the VC prototype to determine whether or not significant power could be generated. Table 6.1 summarizes the characteristics of each motor.



**Table 6.1.** Nanolab pump motors

	Function	Power [kW]
Motor #1	Chilled water supply	29.8
Motor #2	Process cooling water supply	14.9
Motor #3	Condenser water supply	29.8

Motor #1 and motor #3 were horizontally mounted on large vibration-isolating slabs, and motor #2 was vertically mounted with no vibration isolation, as figure 6.1 shows.



**Figure 6.1.** Nanolab motors described in table 6.1. The white circles indicate where acceleration surveys were carried out.

### 6.1.1. Motor vibration harvesting survey

The acceleration surveys were performed with a Kistler 3-axis  $\pm 10$  g capacitive accelerometer with 1 kHz bandwidth. A magnetic mount was used to attach the accelerometer to the various motor surfaces.

The raw acceleration data and corresponding frequency spectrum for motor #1 are shown in figures 6.2 and 6.3.

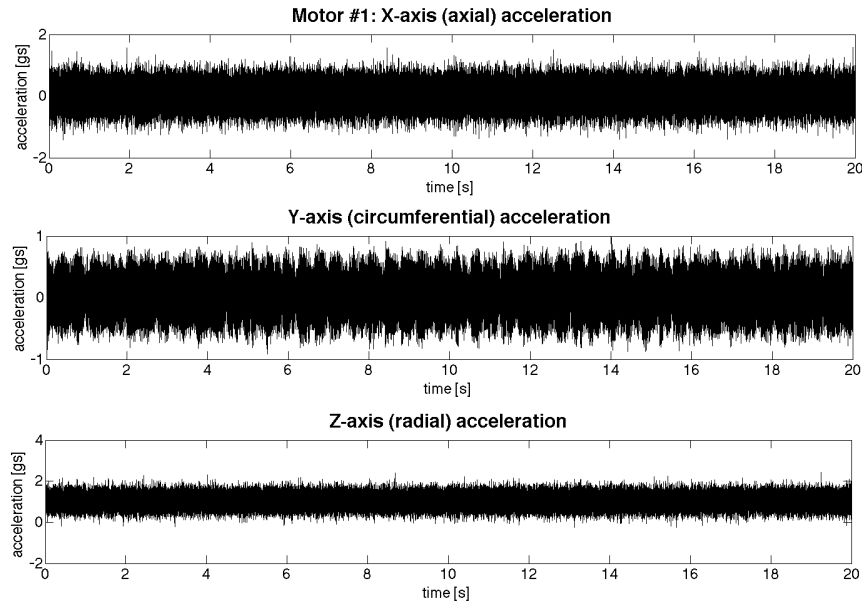


**Figure 6.2.** Raw acceleration data for survey of motor #1.

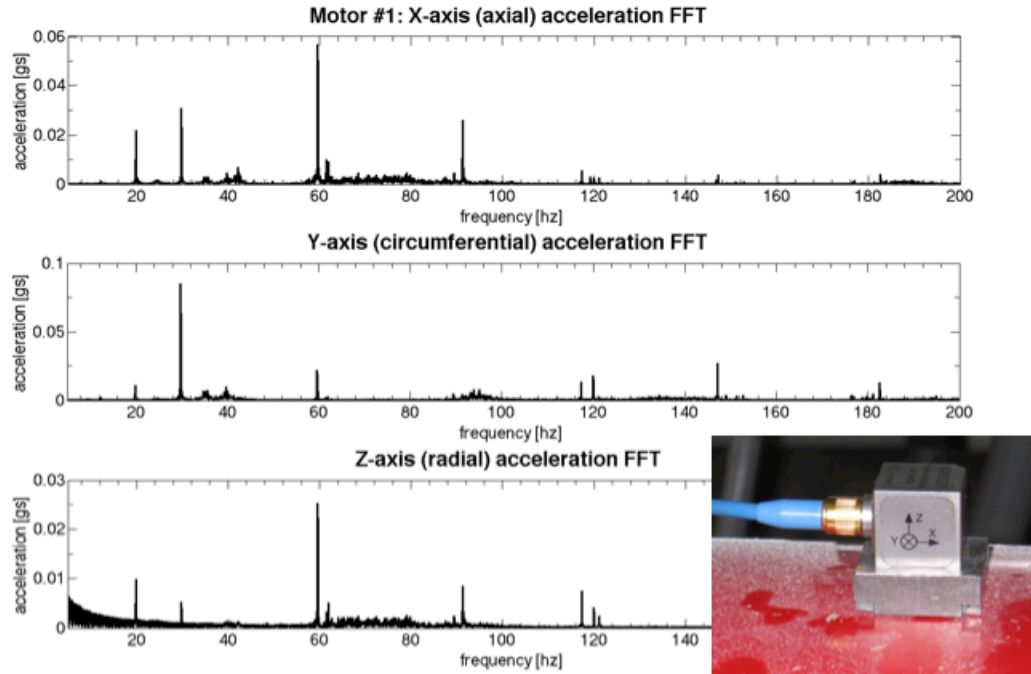


**Figure 6.3.** Frequency spectrum of raw acceleration data for motor #1 in figure 6.2.

The acceleration peaks at 60 Hz and its harmonics are typical for an electrically powered machine. Ultimately, the 60 Hz x-axis peak and the 30 Hz y-axis peak were selected as potentially harvestable.

The raw acceleration data and corresponding frequency spectrum for motor #2 are shown in figures 6.4 and 6.5.

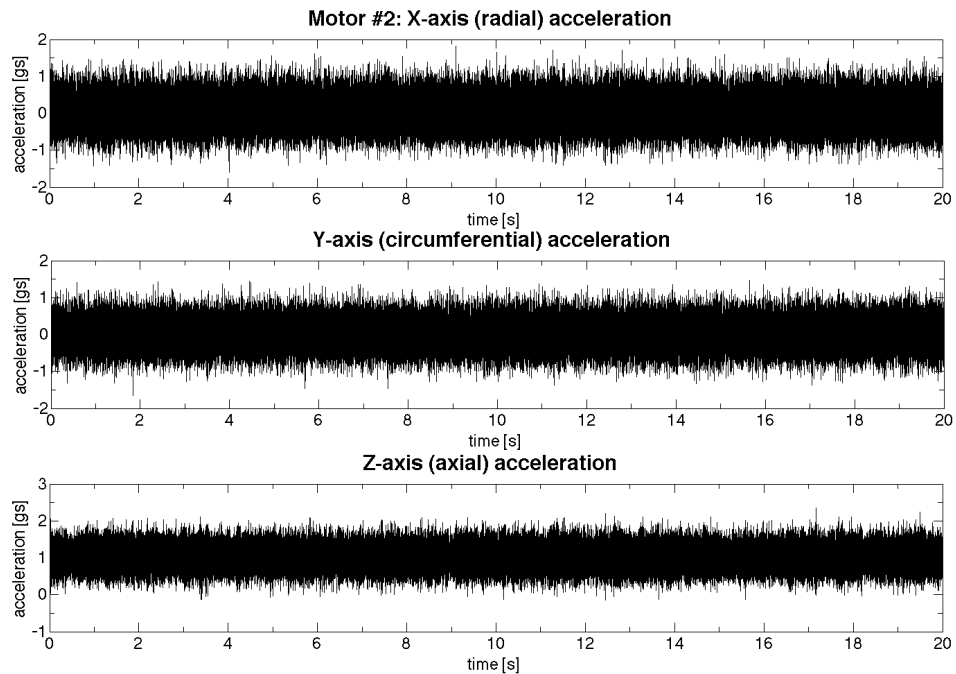


**Figure 6.4.** Raw acceleration data for survey of motor #2.

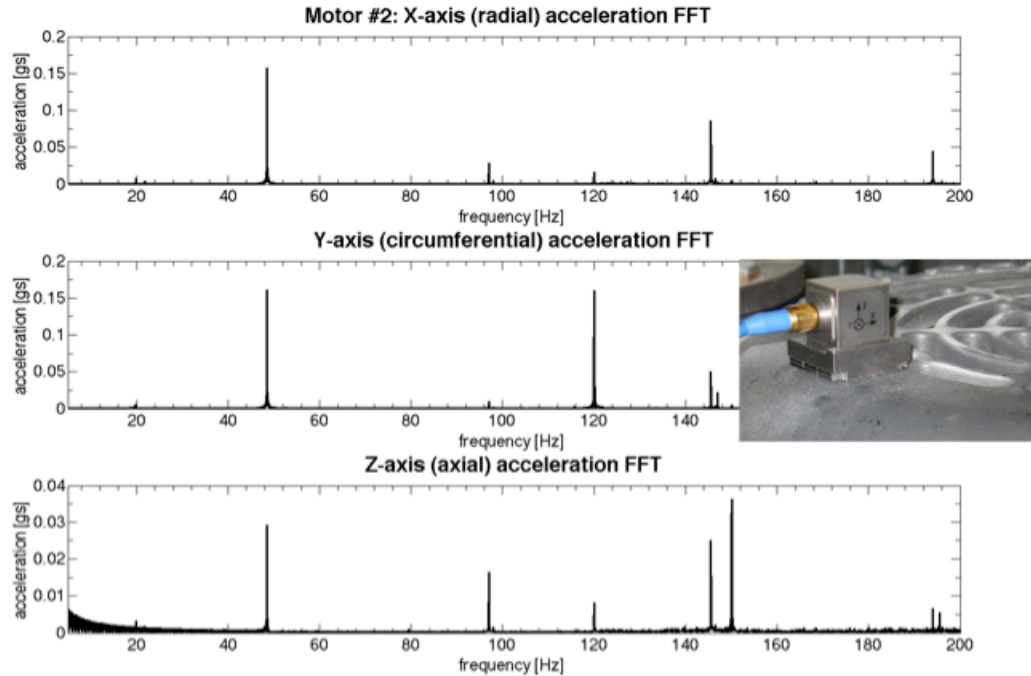


**Figure 6.5.** Frequency spectrum of raw acceleration data for motor #2 in figure 6.4.

While peaks occur at 120 Hz, there is nothing present at the fundamental line frequency of 60 Hz, and the other peaks are likely associated with mounting resonances. Attempts were made to harvest the vibration peak at 50 Hz in the x-axis and the peak at 120 Hz in the y-axis.

Figures 6.6 and 6.7 show the raw acceleration and corresponding frequency spectrum for the survey of motor #3.

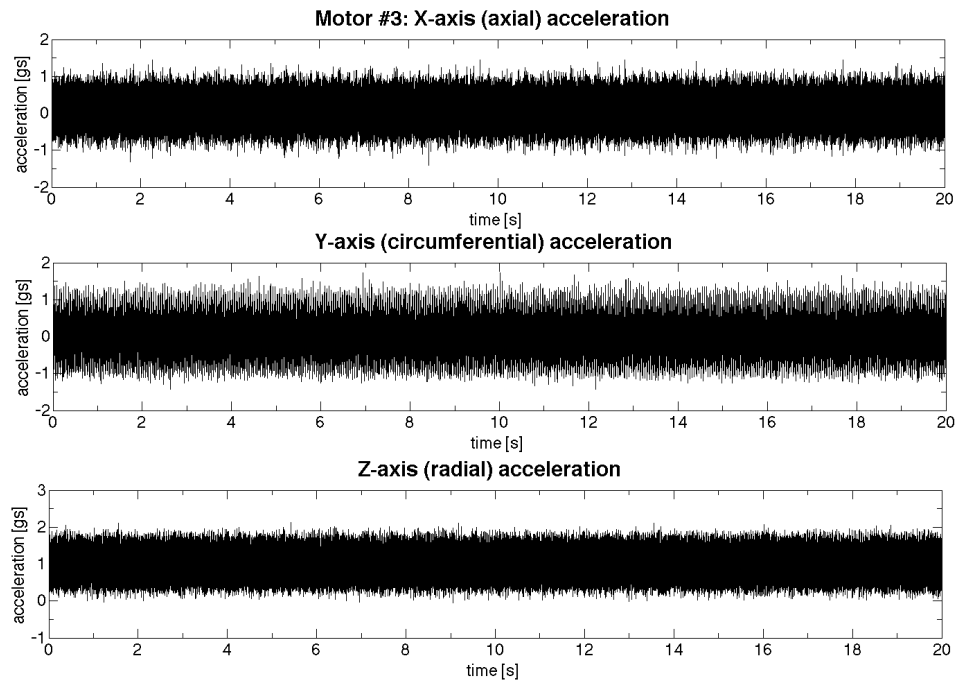


**Figure 6.6.** Raw acceleration data for survey of motor #3.

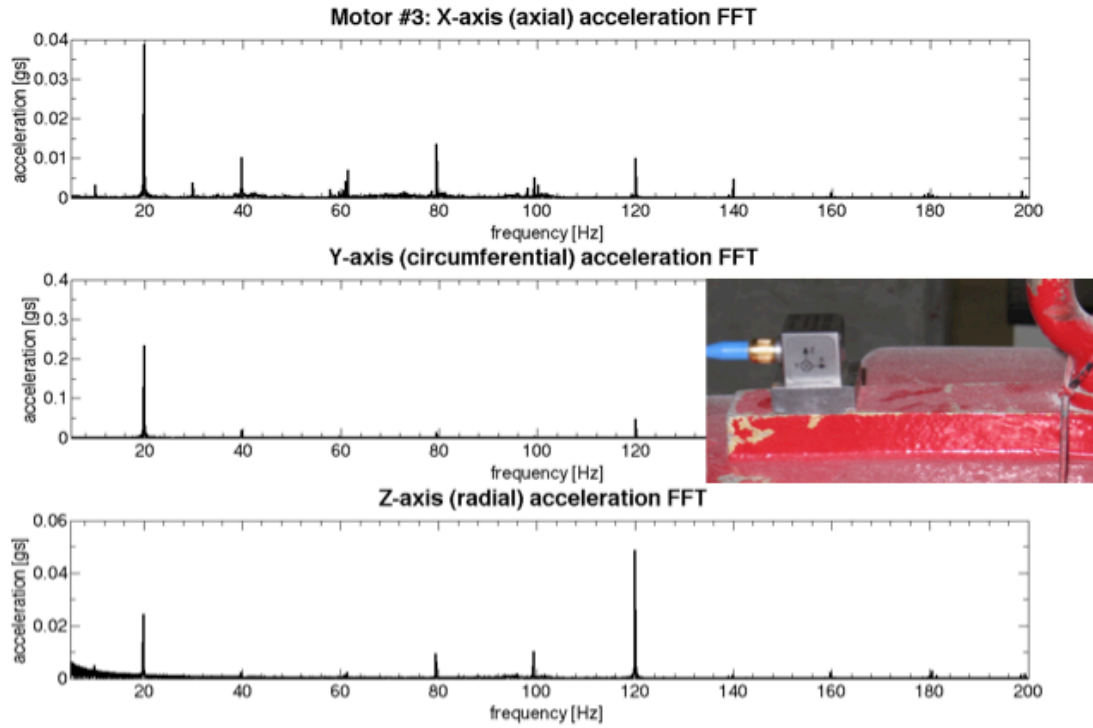


**Figure 6.7.** Frequency spectrum of raw acceleration data in figure 6.6 for motor #3.

Once again there were peaks at 120 Hz, but there is almost nothing at 60 Hz. Harvesting the strong peak at 20 Hz was attempted. In hindsight, *the strong peak at 20 Hz was likely indicative of an unhealthy motor.*

Five peaks from the survey were selected to try and harvest using the VC prototype. The characteristics of the five target vibration peaks are summarized in table 6.2. In general, the most attractive or highest magnitude peaks were selected for the harvesting attempts because changing the springs and thereby the resonant frequency of the prototype was quick and easy. If a possible universal solution fixed frequency device were desired, a resonant frequency of 120 Hz would likely be attractive because a peak was generally present at 120 Hz on one axis for all three motors, even if the magnitude was very low. Commercial vibration harvesters like Perpetuum have chosen to target this second harmonic of the line frequency, but only once in this survey was it found to be the most desirable peak to harvest. It is also worth noting that the highest magnitude peaks never occurred on the axis normal to the mounting surface, so any vibration harvester should to be mounted perpendicular to the surface of the motor. A right angle bracket with a magnetic mount was created for the VC prototype so that the most attractive peaks could be harvested.

**Table 6.2.** Characteristics of the vibration peaks selected for harvesting attempts

<b>Motor #1</b>		
	X-axis (axial)	Y-axis (circumferential)
Frequency [Hz]	59.7	29.8
Acceleration [gs]	0.061	0.082
<b>Motor #2</b>		
	X-axis (radial)	Y-axis (circumferential)
Frequency [Hz]	48.5	120
Acceleration [gs]	0.170	0.060
<b>Motor #3</b>		
	Y-axis (circumferential)	
Frequency [Hz]	19.8	
Acceleration [gs]	0.291	

### 6.1.2. Motor vibration harvesting results

The resonant frequency of the VC prototype was modified by using various combinations of spring thicknesses. To fine-tune the resonant frequency, small magnets were attached to the top spring fastener, adding mass to the resonant system. The impulse response of the harvester was used to evaluate the resonant frequency of the prototype setup. Once the desired resonant frequency was achieved, the prototype was mounted on the motor, and the load resistance was varied until a roughly optimum load was determined. Table 6.3 summarizes the overall results of the harvesting attempts for the three motors.

**Table 6.3.** Harvesting results from large pump motors

	<b>Motor #1</b>		<b>Motor #2</b>		<b>Motor #3</b>
Axis	X	Y	X	Y	Y
Resonant frequency [Hz]	59.9	29.6	49.1	119.9	20.4
Optimum load [Ohms]	210	110	110	210	80
RMS voltage [V]	0.345	0.194	0.404	0.197	0.281
RMS current [mA]	1.64	1.75	3.65	0.94	3.48
Power [uW]	566	342	1477	185	976

Figure 6.8 shows the VC prototype harvesting the target vibration peaks on the x and y axes of motor #1, and figure 6.9 shows the voltage drop across the load resistance for the x-axis vibration target. A reasonably clean signal was generated from a relatively noisy input signal. Similar signals were generated for each harvesting case summarized in table 6.3.

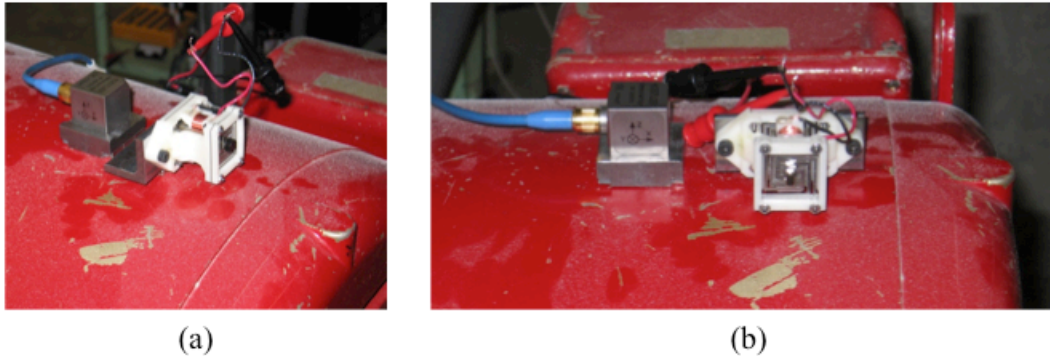


**Figure 6.8.** VC prototype mounted on motor #1 harvesting vibrations along the (a) axial and (b) circumferential directions of the motor.

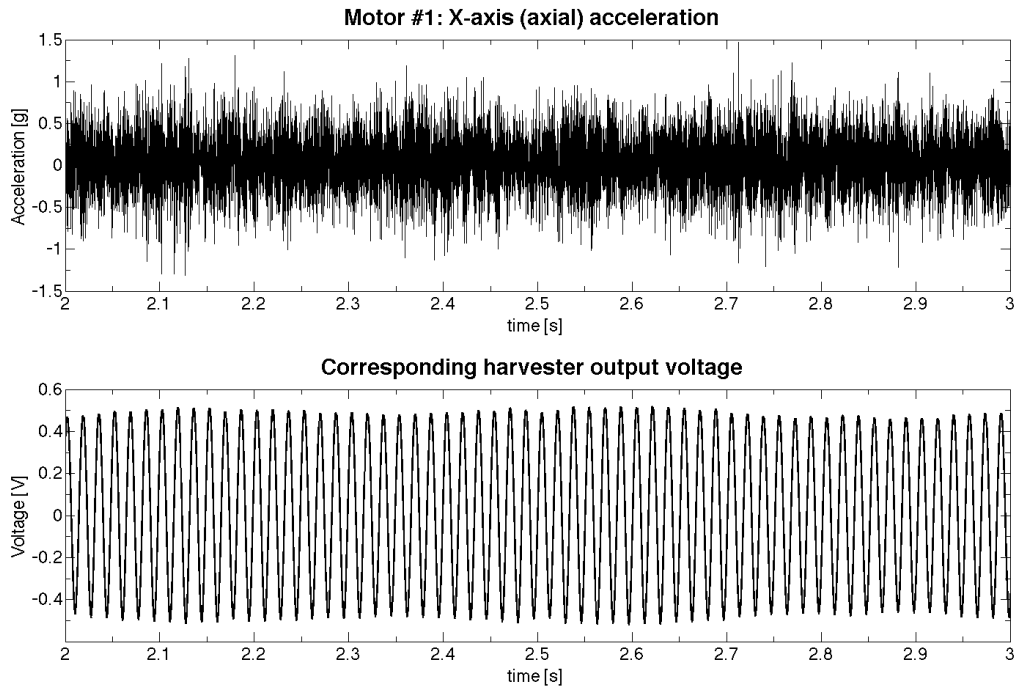


**Figure 6.9.** Input acceleration signal for x-axis of motor #1 and the voltage signal across the load resistance generated by the VC prototype

The power harvested from the real and relatively low magnitude vibrations are very promising. It was also encouraging that the resonant frequency was quickly and easily adjusted to several values between 20 Hz and 200 Hz in a matter of minutes. The voltages generated are low for a practical system, but given that the prototype was only intended to evaluate the proof of concept design and was not designed for the specific application space, the voltage levels are more than tolerable. With knowledge and survey data from this experimental deployment, future designs should be able to produce higher voltage levels.

### 6.1.3. Experimental prediction of failure

Motor #3 failed about a month after the survey and the harvesting experiment were carried out. The motor was shut down before it failed catastrophically because someone happened to enter the machine room for an unrelated reason. Before being shut down it was shaking so violently that the vibration-isolated slab it was mounted on was colliding with the floor, causing the whole room to shake. The water pipes it was connected to were also subject to the severe oscillation. Had it not been shut down when it was motor and pump would have been destroyed and possibly two floors of a brand new building would have flooded.

The strong 20 Hz y-axis rocking on motor #3 was indicative of an unhealthy motor and the impending failure. Figure 6.10 shows the underlying 20 Hz signal. This type of failure would be easily detectable with an accelerometer sensor node, and it indicates the value of this harvesting technology for continuously powering sensor nodes.

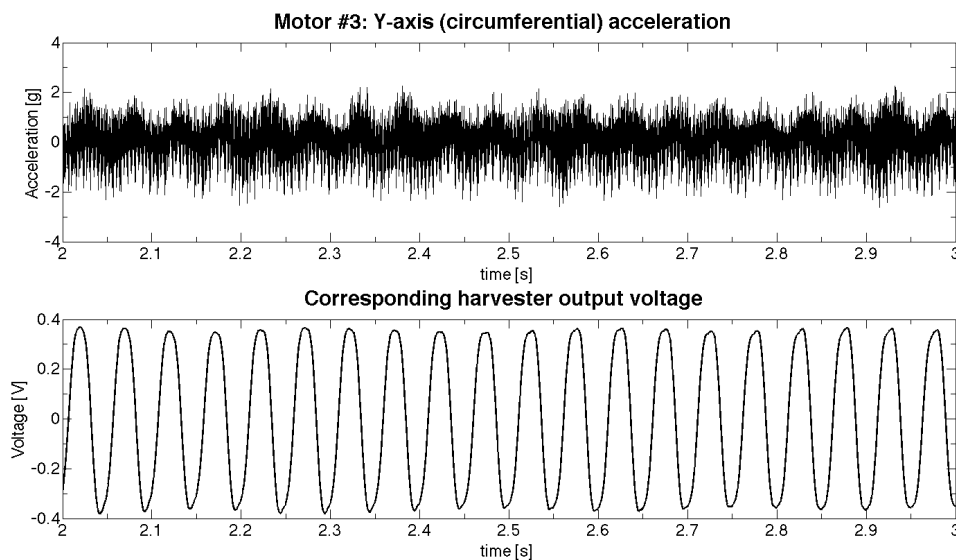


**Figure 6.10.** Dominant 20 Hz acceleration signal from motor #3 that was likely indicative of its impending failure

## 6.2. Machine tool deployment

A Haas VF-0 20 HP three axis machine tool was used to evaluate the possibility of harvesting metal cutting vibrations as well as the rapid axis motion of the machine in order to power on-machine sensors. The target application is condition monitoring but with the potential to improve productivity and reduce tooling costs. A sensor that could evaluate cutter performance would allow replacement of cutting inserts on an as-needed basis instead of being based on some duration of spindle on-time that was determined by some empirical initial evaluation when the process was set up, or a best guess. Unnecessary downtime and insert cost would be eliminated from conservatively changing out inserts, and bad parts or machine damage would be avoided by eliminating insert failure. Similarly, routine maintenance could be carried out on an as-needed basis instead of as a function of spindle on-time.

### 6.2.1. Harvesting metal cutting vibrations

The *Machining Data Handbook* that suggests industry standard cutting rates was used to calculate appropriate spindle speeds and feed rates for a simple facemilling operation in 304 stainless steel, gray cast iron, and 6061-T6 aluminum. A Sandvik Coromant 65 mm diameter facemill with 5 cutting inserts was used for the cuts in all three materials. The stainless steel and cast iron were cut dry, and the aluminum was cut using a general purpose synthetic cutting fluid. Table 6.4 contains the cutting parameters used for each material.

**Table 6.4.** Facemilling cutting parameters

Parameter	Cast iron	Stainless	Aluminum
Depth of cut [mm]	1.02	1.02	1.02
Feed per tooth [mm]	0.18	0.20	0.25
Surface meters per min	134.1	144.8	609.6
Spindle RPM	646	698	2938
Feed rate [mm/min]	574	709	3731

The blocks of material measured 50.8 x 76.2 x 152.4 mm, and the cuts were made along the 152.4 mm dimension, which corresponded with the x-axis of the machine tool. The fundamental cutting vibration frequency is proportional to the spindle rpm and the number of cutting teeth, and it is calculated as

$$f(\text{Hz}) = \frac{\text{RPM} \cdot (\# \text{ of cutting teeth})}{60}. \quad (6.1)$$

For each of the three materials used in the experiment, the second harmonic was of roughly equal or higher magnitude, making them the more attractive frequency peak to try and harvest. The same three-axis Kistler accelerometer used for the pump motor deployments was used here, and the axes of the accelerometer corresponded to the axes of the machine tool. The experimental setup can be seen in figure 6.11.

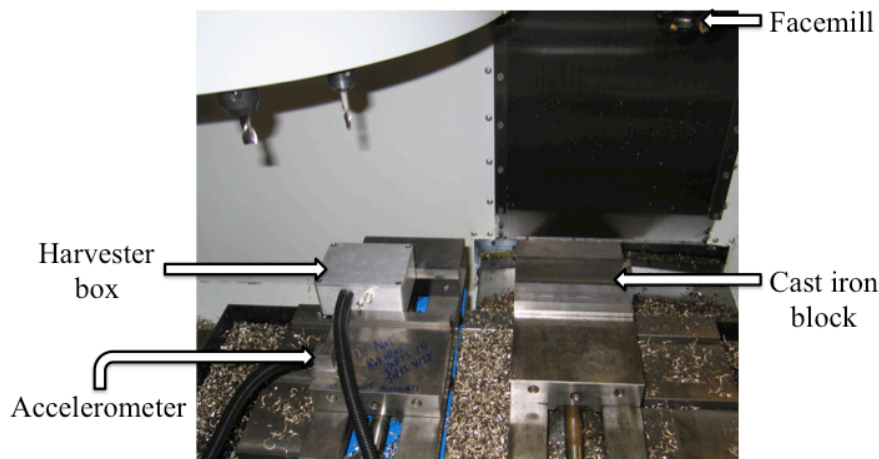


**Figure 6.11.** Facemilling setup. The resonant axis of the harvester was aligned with the x-axis of the machine tool.

The resonant frequency of the VC prototype was broadly tuned by using various spring thicknesses, and it was fine-tuned by attaching magnets to the fastener securing the



center of the top spring for added mass. Once the desired resonant frequency was reached, the harvester was installed in a second vice in the machine. Cuts were taken at various load resistances to find an approximate optimum load, and with the optimum load determined, 5–10 cuts were made.

#### 6.2.1.1. Facemilling vibrations and harvesting results from cutting cast iron

From equation 6.1, the expected fundamental cutting vibration frequency for cast iron was 53.8 Hz. The frequency spectrum of the cutting vibration acceleration in figure 6.13 indicated a fundamental cutting frequency of 53.7 Hz.

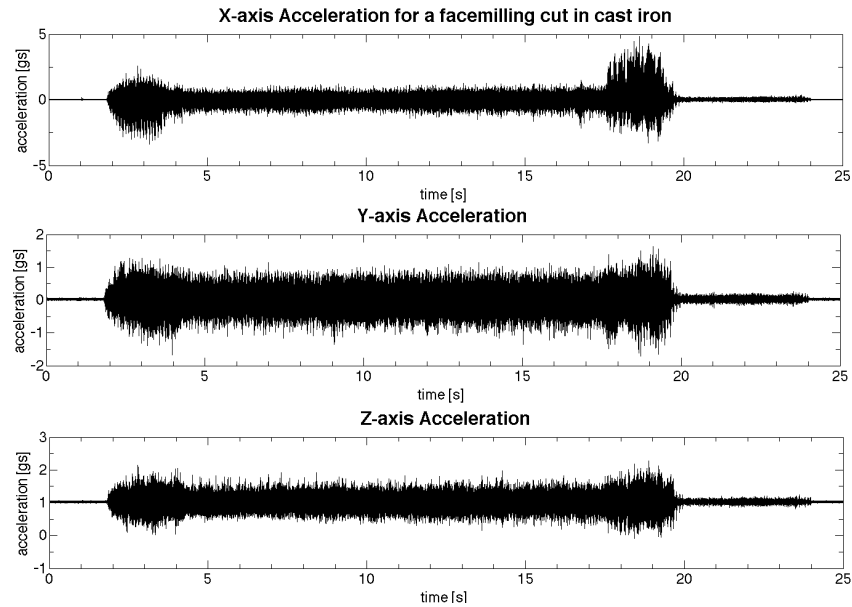


**Figure 6.12.** Raw cutting vibration acceleration for a facemilling cut in gray cast iron.

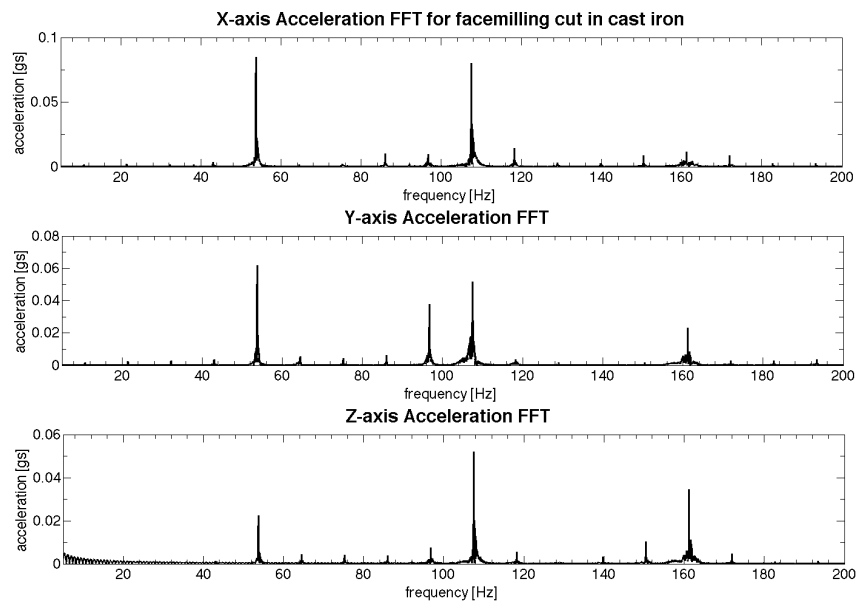


**Figure 6.13.** Frequency spectrum of the raw acceleration data in figure 6.12. The fundamental cutting frequency was 53.7 Hz.

The facemill was centered on the block so the acceleration seen in figure 6.12 increased upon the cutter's exiting the part because two essentially diminishing islands at the corners of the part caused interrupted cuts.

Both the first and second x-axis cutting harmonics were targeted for harvesting. An average of 1.65 mW was generated during cuts when the first harmonic was targeted. The average RMS voltage drop across the 310 ohm optimum load was 0.717 V for the first harmonic. The average power generated during a cut for the second harmonic was 1.88 mW, and the average RMS voltage across the 210 ohm load resistor was 0.631 V. Figures 6.14 and 6.15 show examples of the input acceleration and corresponding harvester output voltage for the first and second harmonic cases.

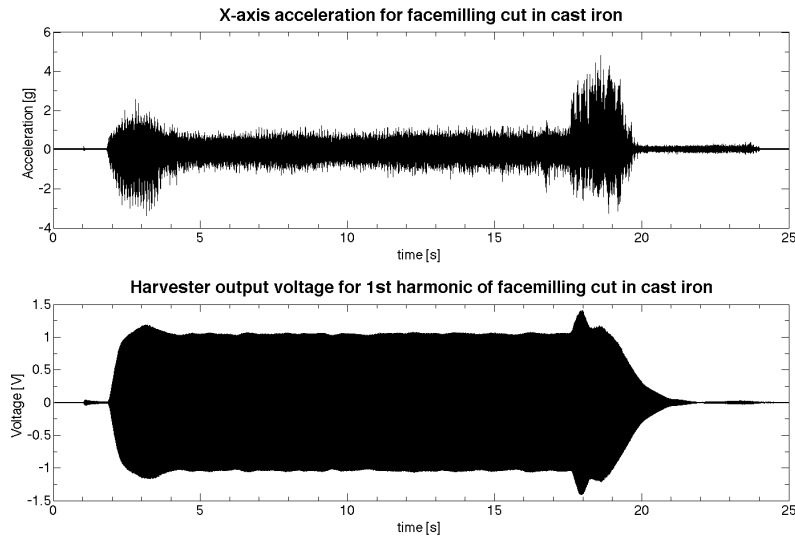


**Figure 6.14.** Raw cutting acceleration and corresponding harvester voltage drop across the load resistance when the fundamental cutting frequency was targeted.

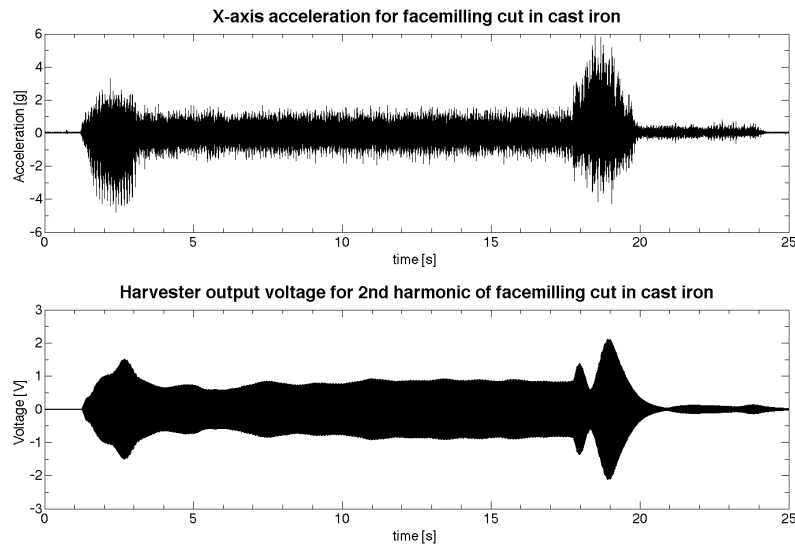


**Figure 6.15.** Raw cutting acceleration and corresponding harvester voltage drop across the load resistance when the second cutting harmonic was targeted.

As an interesting side note, the heat generated from facemilling the cast iron was much higher than that observed for the stainless steel. The accelerometer used had temperature compensation, so it measured and reported temperature. No significant temperature increases were observed while machining the stainless steel that forms continuous chips. In contrast, each cut in cast iron raised the temperature inside the machine by about  $0.1^{\circ}\text{C}$ , possibly because of the small interrupted chips that form and higher cutter tip forces, as suggested by Trent and Wright in [66].

#### 6.2.1.2. Facemilling vibrations and harvesting results from cutting stainless steel

The acceleration magnitude for the second cutting harmonic peak in stainless steel was significantly higher than the fundamental frequency, as figure 6.17 shows, so only the second harmonic was targeted for harvesting. The expected fundamental cutting vibration frequency using equation 6.1 was 58.2 Hz, and the experimental fundamental frequency peak occurred at 58.1 Hz. The raw and frequency spectrum acceleration data for a cut in stainless steel are shown in figures 6.16 and 6.17.

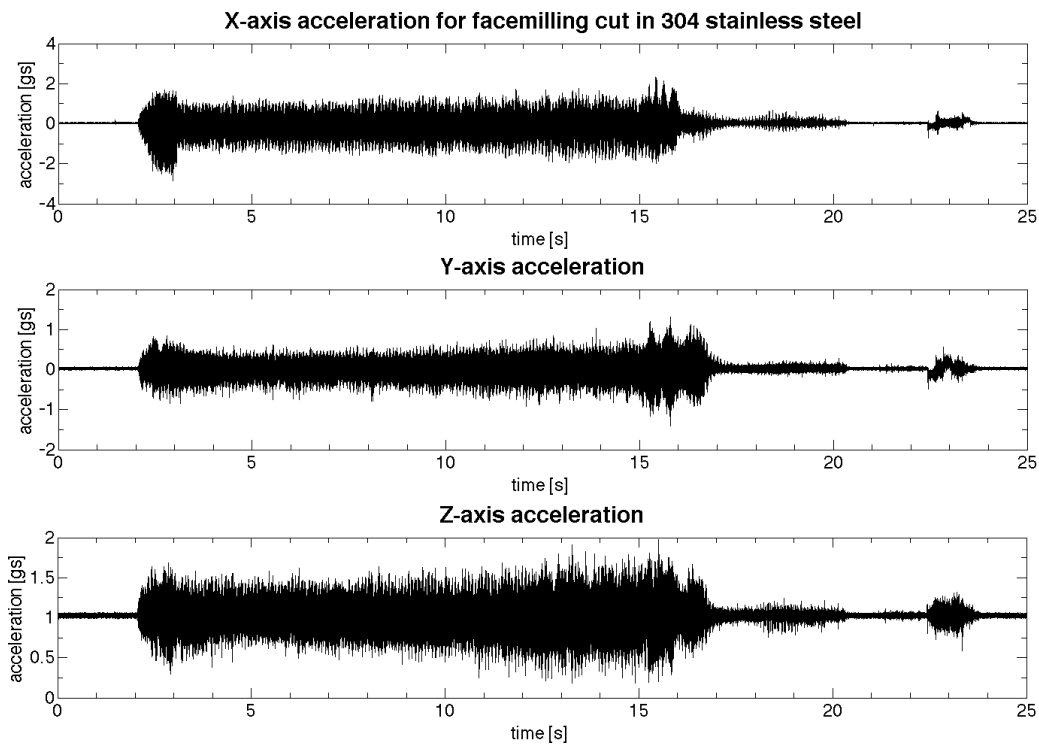


**Figure 6.16.** Raw cutting vibration acceleration for a facemilling cut in 304 stainless steel. The axes correspond to the axes of the machine tool

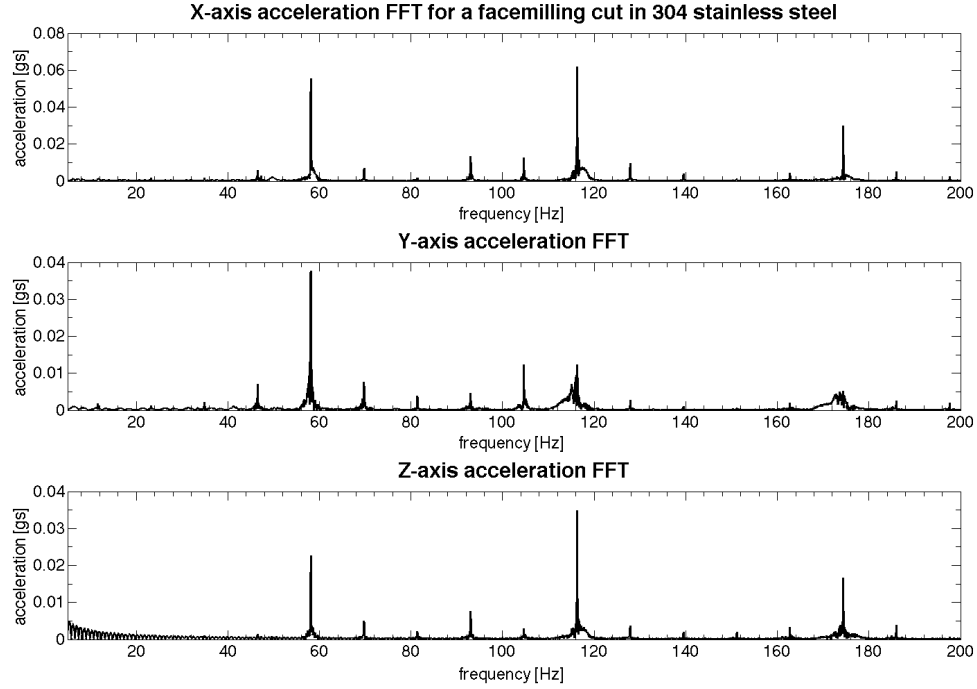


**Figure 6.17.** Frequency spectrum of the raw acceleration data in figure 6.16. The fundamental cutting frequency was 58.1 Hz.

The second cutting harmonic at 116.2 Hz was the harvesting target, and an average of 0.88 mW was generated during a cut. The average RMS voltage drop across the optimum load resistance of 410 ohms was 0.601 V. Figure 6.18 shows an example of the input cutting acceleration and corresponding voltage generated by the VC prototype across the load resistance.

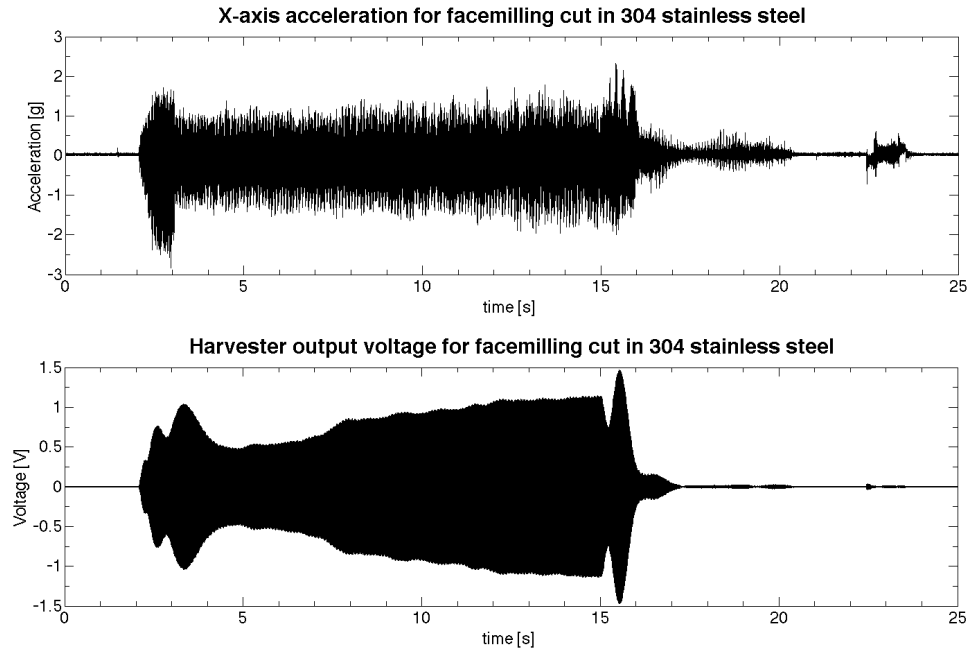


**Figure 6.18.** Raw cutting acceleration and corresponding harvester voltage drop across the load resistance for the second cutting harmonic when facemilling stainless steel.

#### 6.2.1.3. Facemilling vibrations survey for cutting 6061-T6 aluminum

Using equation 6.1, the fundamental cutting frequency was calculated to be 244 Hz, which was too high to try and harvest with the available springs for the VC prototype. As a result, a few cuts were taken to characterize the cutting vibrations associated with the facemilling operation in aluminum. Figure 6.19 shows the frequency spectrum for an acceleration measurement for a cut. The x-axis second cutting harmonic at a peak of 489.4 Hz appeared to be harvestable, so machining aluminum may be an attractive environment for higher frequency vibration harvester designs. Interestingly, the dominant peak for aluminum occurs on the y-axis at the fundamental cutting frequency and would also be very attractive for vibration harvesting.

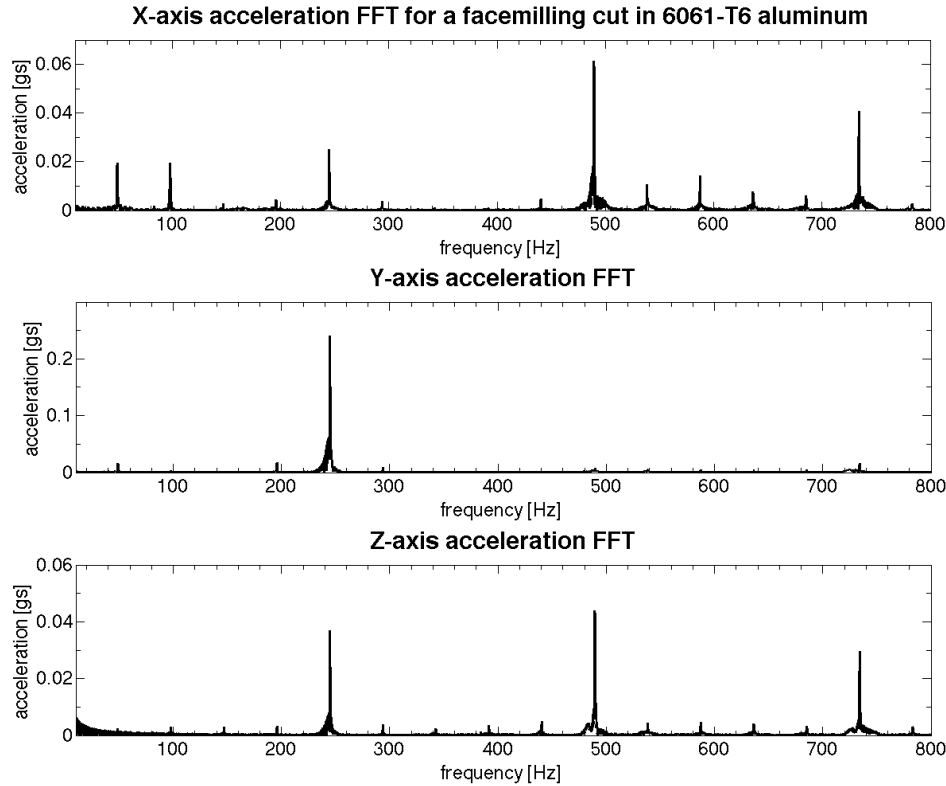


**Figure 6.19.** Cutting vibration acceleration frequency spectrum for a facemilling cut in aluminum. The axes correspond to the axes of the machine tool.

#### 6.2.1.4. Summary of metal cutting vibration harvesting

The 0.88–1.88 mW harvested from cutting vibrations while facemilling stainless steel and cast iron indicate that significant power can potentially be harvested from industry standard metal cutting operations. Considering that the harvester used was not designed with a machine tool and metal cutting environment in mind, the results are very encouraging. Even the output voltages while still on the low side at 0.6–0.7 volts RMS are promising. The major drawback is that the harvester must be configured for each material to be cut and possibly for each cutting operation, but in an industrial setting, it is common to have a machine run the same operation or program using the same material

for long periods of time, making this harvesting idea potentially attractive nevertheless. Tables 6.5 and 6.6 summarize the harvesting results for the facemilling experiments.

**Table 6.5.** Facemilling vibration characteristics

<b>304 stainless steel</b>		
Harmonic	1st	2nd
Frequency [Hz]	58.1	116.2
Acceleration [gs]	0.056	0.062
<b>Cast iron</b>		
Frequency [Hz]	53.8	107.5
Acceleration [gs]	0.085	0.08
<b>Aluminum 6061-T6</b>		
Frequency [Hz]	244.8	489.4
Acceleration [gs]	0.025	0.061

**Table 6.6.** Facemilling metal cutting vibration harvesting results

	<b>Stainless steel</b>		<b>Cast iron</b>			
Resonant frequency [Hz]	116.3		54		107.6	
	<b>Mean</b>	<b>STD</b>	<b>Mean</b>	<b>STD</b>	<b>Mean</b>	<b>STD</b>
RMS voltage [V]	0.601	0.013	0.717	0.002	0.631	0.008
Power [uW]	883	38	1654	11	1878	68
Optimum load [ohm]	410		310		210	

### 6.2.2. Harvesting machine tool rapid axis motion

Another machine tool operation that could potentially be used as input for a vibration harvester is the rapid motion of the axes. A rapid jog and stop while repositioning or changing tools can induce an impulse response in a vibration harvester, generating some small amount of energy. The advantage to this source of potentially harvestable energy is that it is no longer dependent on the material or the cutting operation. The Haas VF-0 rapids at 12.7 meters per minute. More modern machines rapid at twice that rate. As with the metal cutting experiments, the harvester box was held as shown in figure 6.11, and the resonant axis of the harvester was aligned with the axis of rapid motion for the machine tool.

After confirming a rapid-stop event could induce an impulse response in the VC prototype as figure 6.20 shows, the dependence on jog length and device resonant frequency was explored. Optimum load resistances were determined by evaluating the power performance of a load resistance for a 5 mm rapid jog.

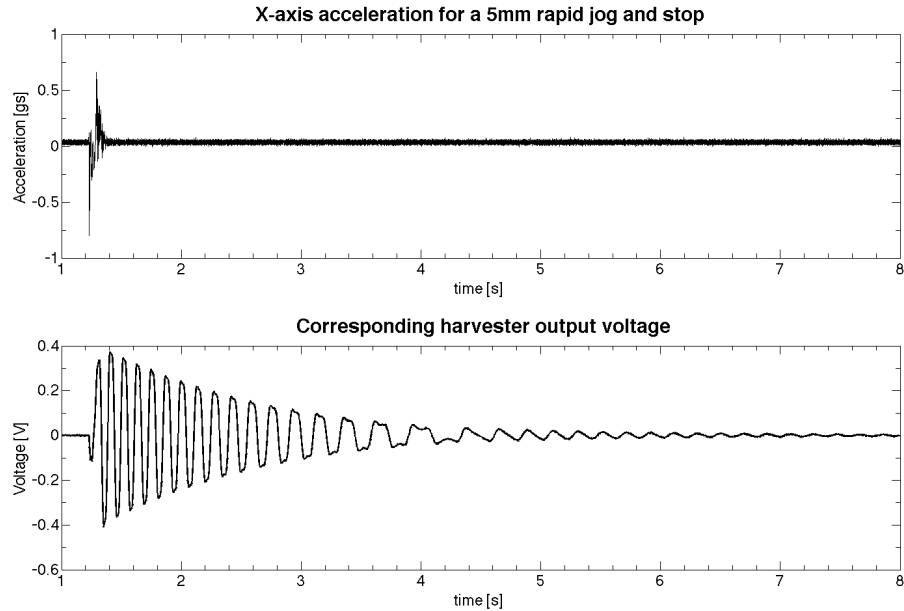


**Figure 6.20.** Impulse response of the VC prototype induced by a 5 mm long rapid move and stop. The prototype had the 0.08 mm thick springs installed, making the resonant frequency of the device about 8 Hz.

Depending on the resonant frequency and jog length, destructive interference was possible. Essentially, the acceleration at the start of the rapid motion caused the resonant mass to start moving, and if the acceleration of the stop event caught the mass moving in the opposite direction, the motion of the resonant mass was diminished. But if the acceleration of the stop event and motion of the resonant mass were in the same direction, then the motion was amplified. Table 6.7 shows this phenomenon as jog length was varied for four device configurations and thereby resonant frequencies. The energy produced was calculated by integrating the area under the instantaneous power curve of voltage multiplied by current.

**Table 6.7.** Energy produced, in micro-Joules, for a rapid jog and stop event as a function of jog length and device resonant frequency

micro-Joules	Rapid jog length				
Resonant $f$	5mm	10mm	50mm	100mm	200mm
8 Hz	116	44	61	64	57
12 Hz	34	2	38	22	42
32 Hz	4	12	2	11	5
42 Hz	10	5	12	10	14

Based on table 6.7 data, a lower resonant frequency appeared to be beneficial, and this trend is illustrated more clearly in figure 6.21. The trend of a lower resonant frequency performing better was not entirely surprising, given the relatively small magnitude of the input acceleration impulses. The small impulse was basically not large enough to displace the stiffer higher resonant frequency configurations and generate significant relative motion.

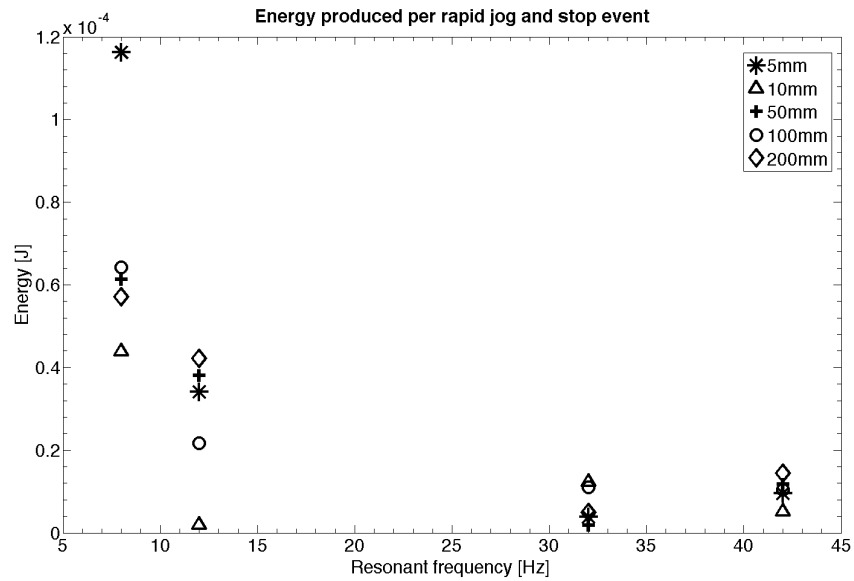


**Figure 6.21.** Trend of energy produced per rapid jog and stop as a function of harvester resonant frequency.

A test part was designed and machined to show the potential viability of the rapid motion harvesting under more realistic circumstances. The part was machined from 6061 aluminum and consisted of a facemilling operation, two shallow pockets, and five shallow holes. The test part is shown in figure 6.22. The facemilling operation was done in one pass, and the pockets had roughing and finishing passes. The rapid motions came from tool changes and positioning for operations.

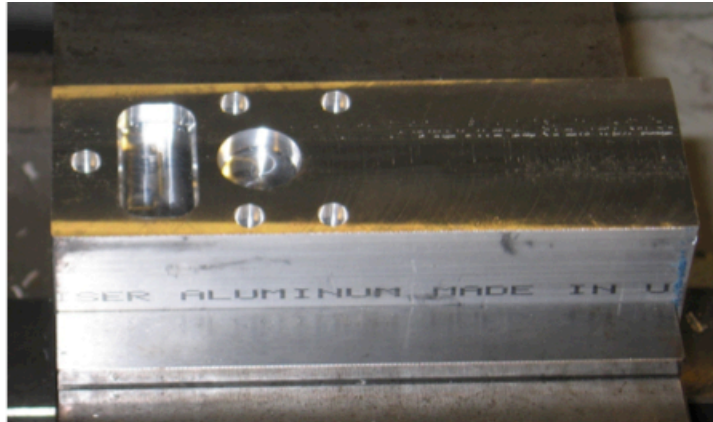


**Figure 6.22.** Test part in the vice of the machine tool.

The VC prototype configured for the 8 Hz resonant frequency was aligned both along the x-axis and the y-axis of the machine while test parts were cut with similar results. The x-axis acceleration and corresponding generated voltages of the harvester are shown in figure 6.23.



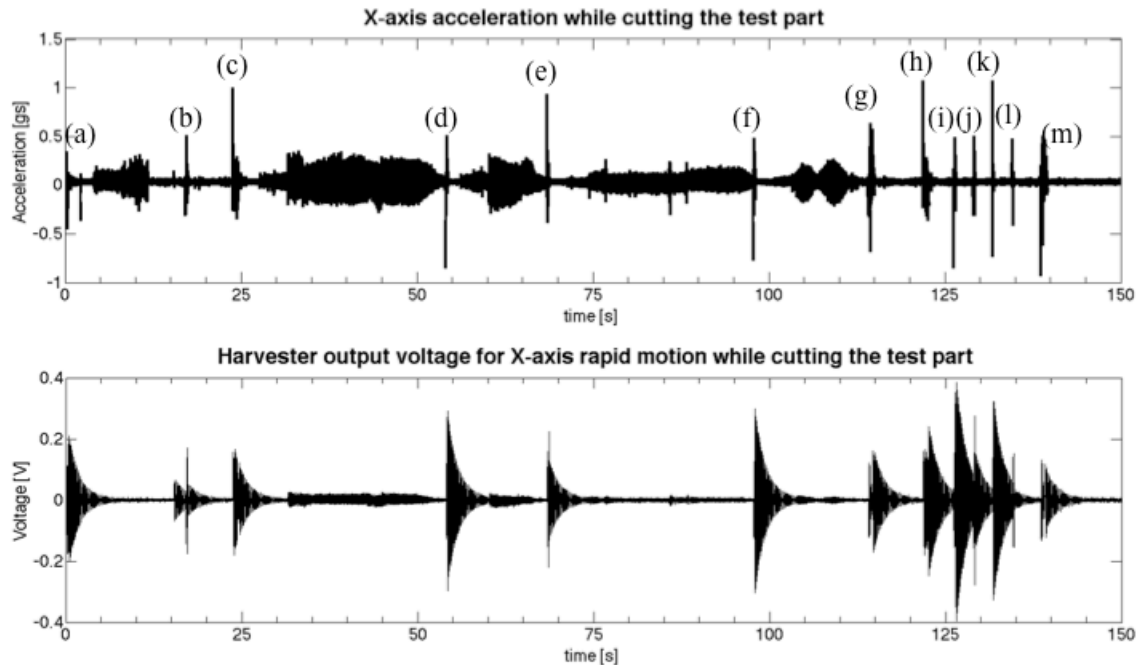


**Figure 6.23.** Acceleration and induced harvester response from rapid events while cutting a test widget. Refer to table 6.8 for descriptions of the jog events associated with the bracketed letters.

Interesting data on the impulse responses of the harvester occurs from 120–140 seconds in figure 6.23, when the five holes were being drilled, because it suggests that with a modern machine that rapids faster and cuts faster, a continuous set of dense impulse responses might emerge. At that point, it might be possible to refer to the average power of the signal instead of the energy generated per event. It is also worth noting that the machine was not pushed during the machining of the widget, and high-speed steel tooling was used, so the feeds and speeds were relatively low, causing longer pauses between rapid motion events.

The harvesting results for the test part experiment for both x-axis and y-axis motions are summarized in table 6.8. In this table, pocket 1 is the rectangular pocket, and pocket 2 is the circular pocket. TC is used as shorthand for tool change, and home refers to the machine home, which corresponds to absolute zero for the various machine tool axes. In total, eight widgets were cut.

The energy harvested from the rapid motion events was very small, but it serves as a reasonable proof of concept. At the very least, it would be interesting to explore what might be possible on a modern machine tool with a harvester designed with this application in mind. The VC prototype is not at all well suited for this harvesting situation because the minimum operating frequency considered during its design was around 40 Hz. While it clearly can resonate at 8 Hz, it does not do so very effectively, and the mechanical translation limits are often encountered at resonant frequencies below 20 Hz. Given the limitations of the prototype and machine tool, the conclusions drawn from this rapid motion harvesting experiment should be high level and focus on the proof of concept.

**Table 6.8.** Harvesting results for rapid jog events while machining the test parts

	Units = micro-Joules	X-axis	X-axis	Y-axis	Y-axis
	Rapid moves	Mean	STD	Mean	STD
(a)	1st position	38.2	1.3	24.6	0.1
(b)	Home for TC	9.6	0.0	21.5	0.1
(c)	Position of pocket 1	26.6	0.2	11.0	0.6
(d)	Position of pocket 2	61.9	0.1	21.0	0.0
(e)	Finish cut pocket 1	18.9	0.0	15.5	0.0
(f)	Finish cut pocket 2	68.1	0.2	18.9	0.1
(g)	Home for TC	25.7	0.1	22.8	0.1
(h)	Position hole 1	60.0	0.6	23.0	0.1
(i)	Position hole 2	125.7	5.6	4.4	0.0
(j)	Position hole 3	14.9	10.8	No Y-move	No Y-move
(k)	Position hole 4	81.1	6.2	129.0	0.0
(l)	Position hole 5	5.7	1.0	No Y-move	No Y-move
(m)	Return to home	15.2	2.8	58.6	0.2
	<b>Total Energy</b>	<b>551.8</b>	16.4	<b>350.3</b>	0.1
	<b>Energy per rapid</b>	<b>42.5</b>	35.1	<b>31.8</b>	35.0

### 6.3. Simulated vehicle suspension deployment

The final application area explored was vehicle or asset monitoring or tracking where the vibrations from the unsprung suspension of vehicles could potentially be an appreciable source of harvestable energy. The specific applications include tracking semi trailers and thereby shipping containers, tracking military vehicles or heavy equipment assets, or tracking personal vehicles which the FBI and homeland security currently accomplish with a GPS transmitter and a large tube of six or more D-cell batteries magnetically attached to the underside of the car of a person of interest.

A previous project in the lab carried out an energy harvesting audit of a car for Bosch. Researchers Andrew Pullin and Dan Stiengardt generated a large amount of data classifying vibrations, thermal gradients, and solar insolation throughout a car, and the vibrations associated with the unsprung suspension of a Mazda rx7 were among the vibration sources characterized. The two data sets used in this work were logged on a trip from San Mateo, CA, to Berkeley, CA, and on a trip from Berkeley, CA, to Los Angeles, CA, as shown in figure 6.24. GPS locations were recorded each time acceleration data was captured, with 2.5 seconds of acceleration data recorded for each location. Acceleration data was logged at 164 points along the trip from San Mateo to Berkeley and at 769 points along the trip from Berkeley to LA.

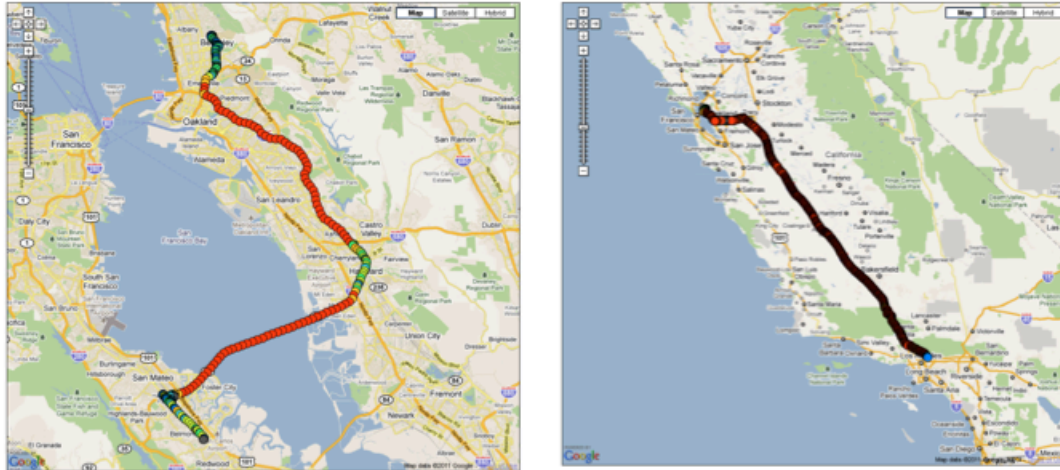


**Figure 6.24.** Google maps indicating where acceleration data was taken during the trips in from San Mateo to Berkeley and Berkeley to Los Angeles, California

As might be expected because of varying vehicle speeds and road condition, there were no reoccurring specific acceleration peaks at specific frequencies. Instead, most of the energy is concentrated low in the frequency spectrum. Essentially, no significant accelerations occur above 150 Hz, and most of the accelerations of reasonable magnitude typically occur below 50 Hz. Figure 6.25 shows an example acceleration spectrum for the trip from Berkeley to LA.

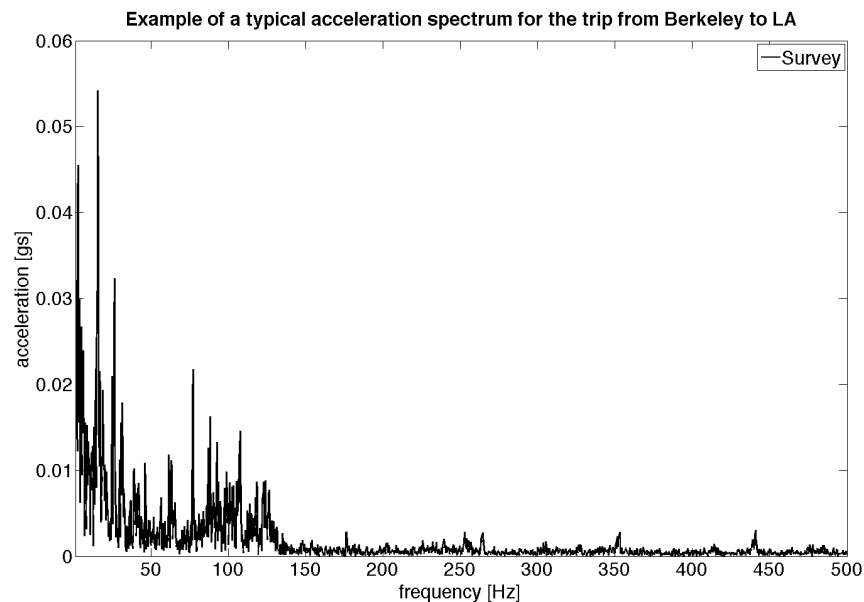


**Figure 6.25.** Example acceleration spectrum for the unsprung suspension of an rx7 travelling south on Interstate 5 in California at over 97 kph.

A Labview program was created using the acceleration data as input for the electrodynamic vibration platform setup described in section 4.1. The VC prototype was then shaken with every data set indicated by a dot on the maps in figure 6.24. Since the energy is at low frequency, a spring configuration with a resonant frequency of 19 Hz was used. The experiment was repeated with a spring configuration that resonated at 93

Hz to show that the harvested power at higher frequencies was minimal. The configurations were evaluated with a single frequency sinusoidal signal with a 0.1 g acceleration amplitude to determine an optimum load. For the 19 Hz configuration, the optimum load was about 100 ohms, and for the 93 Hz configuration, the optimum load was about 310 ohms. Tables 6.9, 6.10, and 6.11 summarize the results of the experiment.

**Table 6.9.** Results for VC prototype with a 19 Hz resonant frequency on the drive from San Mateo, CA, to Berkeley, CA

	0–48.3 kph		48.3–96.6 kph		96.6+ kph	
	Mean	STD	Mean	STD	Mean	STD
RMS voltage [V]	0.071	0.074	0.191	0.064	0.228	0.078
Power [uW]	104	181	399	267	574	343
Maximum Power [uW]	824		964		1290	

**Table 6.10.** Results for the VC prototype with a 19 Hz resonant frequency on the drive from Berkeley, CA, to Los Angeles, CA

	0–48.3 kph		48.3–96.6 kph		96.6+ kph	
	Mean	STD	Mean	STD	Mean	STD
RMS voltage [V]	0.039	0.042	0.062	0.034	0.061	0.038
Power [uW]	32	79	50	57	51	76
Maximum Power [uW]	534		361		788	

**Table 6.11.** Results for VC prototype with a 93 Hz resonant frequency on the drive from Berkeley, CA, to Los Angeles, CA

	0–48.3 kph		48.3–96.6 kph		96.6+ kph	
	Mean	STD	Mean	STD	Mean	STD
RMS voltage [V]	0.010	0.014	0.022	0.015	0.023	0.016
Power [uW]	1	4	2	4	3	5
Maximum Power [uW]	32		27		62	

The results from the San Mateo to Berkeley trip in table 6.9 were promising, but may be more of an indictment of the roads in the San Francisco Bay area in light of the results for the Berkeley to LA trip. The results from the two trips suggest that for vibration harvesting on vehicle suspensions it's likely that the most desirable situation is to have rough road surfaces, low profile tires, and high travelling speeds. A signal representative of the average power harvested at 96.6+ kph for the trip from San Mateo to Berkeley is shown in figure 6.26.

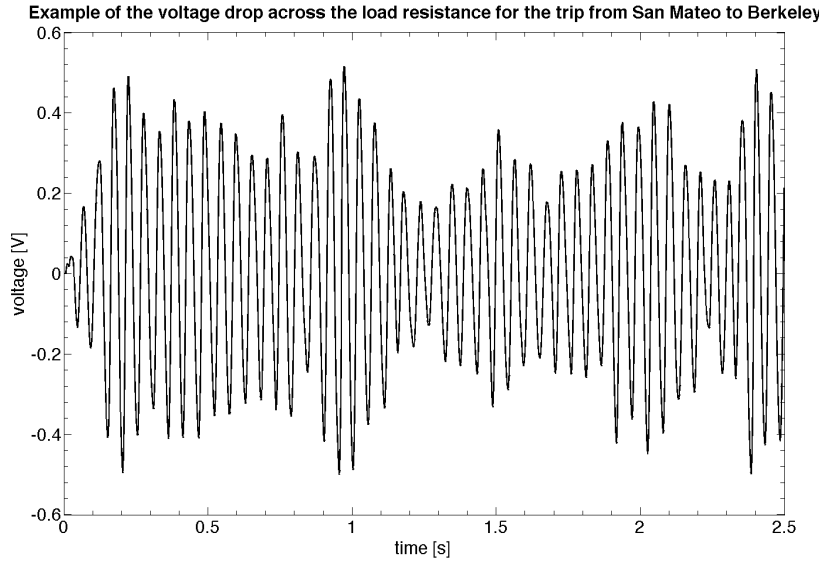


**Figure 6.26.** Voltage signal representative of the average power harvested for the 96.6+ kph category on the trip from San Mateo to Berkeley in table 6.9. The signal corresponds to the 19 Hz resonant frequency configuration of the VC prototype.

The almost 0.6 mW at highway speed in table 6.9 was encouraging, and it suggests that future work in this area may be worth exploring. With a harvester designed for the low frequencies associated with vehicle suspensions, more reasonable performance and at least higher output voltages could be achieved even for smoother roads like those encountered on the trip from Berkeley to LA. This application space is further complicated considering that it would be relatively power intensive because any GPS tracking would be relayed over a cell phone network, meaning that the transmit power would be about one watt instead of the tens of milliwatts that is standard for wireless sensor nodes.

The power numbers presented here were not cherry picked from acceleration spectra but rather are statistically relevant and representative of a real world situation, albeit with a harvester never intended for this application and poorly suited to it. From a high level perspective, the findings show that a reasonable amount of power can be harvested from the vibrations of vehicle suspensions even with a resonant device, and while the powers derived in this work are low for the target application, future devices designed with this environment and base knowledge in mind might yield a viable solution. Also, the results do show that targeting low frequencies below 30 Hz produces significantly more power than targeting higher frequencies, as indicated by comparing the results in table 6.10 and table 6.11.

## Chapter 7. Design discussion and future outlook

---

- 1) Voltage Constraint: A voltage constraint needs to be added to the design evaluation and optimization so that it is as easy as possible to rectify and store the power that is harvested. While rectification of voltages less than one volt has been demonstrated for vibration harvesters in [59][60], the losses for rectifying lower voltages become large.
- 2) Add the second coil to the OMC prototype: Since only a proof of concept of the modeling and evaluation of the general performance of the system was desired, only one of the two coils for the full device was fabricated. Adding the second coil and characterizing it would provide insight into how accurate the approximation of doubling the generated power was, and it would provide useful data on the travel of the system during operation. The travel numbers would enable further optimization of the device as well as improved power density.
- 3) Linear springs: The current spring geometry was linear for higher frequencies, in excess of about 90 Hz, but the larger deflections at lower frequencies caused stiffness hardening nonlinearity. Adding more turns to the spiral beam pattern would likely address this issue, but it could explore the geometry changes necessary to get a linear stiffness from the planar springs at lower frequencies.
- 4) Prototype proposed Halbach design: Higher gap flux densities would lead to higher output voltages and possibly enable smaller harvesters. Building and evaluating the Halbach array-inspired design to verify the significantly higher gap flux density and improved voltages could lead to much improved vibration harvesters. Gap flux densities approaching one tesla have not been reported in previous vibration harvester research.
- 5) Add rectification circuitry: Rectified power is what is important, and for a system to be useful, the harvested power needs to be rectified so that it can be stored in an appropriate battery or capacitor. Adding rectification would allow for full sensor node demonstrations in realistic environments for the condition-monitoring systems that motivated this research.
- 6) Break up the target frequency range: The target vibration frequency range expanded from 40–150 Hz to 5–150 Hz or higher if vibrations from machining aluminum are included. Given the large difference in the travel of the device over this frequency range, a one-size-fits-all design imposes unnecessary restrictions that lead to unused volume at higher frequencies. Investigating the optimum designs for 20–30 Hz segments of the total resonant frequency range seems worth exploring further.
- 7) Rapid-stop motion revisited: While it was demonstrated that energy can be harvested from a rapid-stop type impulse event, the VC prototype was poorly

suited for this effort. It may turn out that the extremely low resonant frequencies and low output voltages observed might make this a source that could be better harvested by a meso piezoelectric vibration harvester.

- 8) Hybrid scavenger: A package that combines energy harvesting sources could be of tremendous value. Adding small photovoltaic panels to an outer surface of one of the prototype harvesters would be relatively easy and would allow a single device to scavenge energy from two very common sources.
- 9) Full condition monitoring sensor node on a machine tool: Assembling a condition monitoring node that both monitors a metal cutting operation and is powered from the metal cutting vibrations, rapid-stop motion of the axes, and possibly some small photovoltaic cells would fully demonstrate the potential impact of the vibration harvesting technologies explored in this work while directly addressing the goals that motivated this research. The condition monitoring sensor could be a MEMS accelerometer, and the communication could periodically provide status updates to a base station connected to the internet. Use of a commercial wireless sensor node would provide the greatest impact.

## Chapter 8. Conclusions

---

- 1) The VC prototype was deployed on several 15–30 kW pump motors in the machine room of the University of California, Berkeley microfabrication laboratory, where it harvested 0.19–1.48 mW for the various input acceleration peaks selected. The full results are summarized in tables 6.2 and 6.3. One of the three motors used during this experiment failed unexpectedly a month later, indicating the potential importance of condition monitoring of high value equipment to eliminate unanticipated failure and unscheduled down time. The vibration characteristic of the eventual failure was present during the experiment and could have been easily detected a month before the failure.
- 2) It was shown that metal cutting vibrations can be successfully harvested, and the cutting vibration frequency can be characterized by the number of cutting teeth and the spindle RPM. Facemilling operations were performed on cast iron, stainless steel, and aluminum blocks with industry standard cutting parameters. The second harmonic of cutting vibration frequency was consistently the most attractive vibration peak to try and harvest. The VC prototype harvested 0.88 mW at 116 Hz while facemilling stainless steel, and it harvested 1.88 mW at 108 Hz while facemilling cast iron.
- 3) The unrectified power densities of the OMC and VC prototypes were comparable to the rectified power densities of the commercially available vibration harvesters, as table 8.1 shows. The power density numbers were very encouraging given that the prototypes were built more for proof of concept purposes and could be further optimized.

**Table 8.1.** Power density comparison to commercially available harvesters

Author, Reference	Frequency [Hz]	Acceleration [g]	Size [cm <sup>3</sup> ]	Power density [mW•cm <sup>-3</sup> •g <sup>-2</sup> ]
Perpetuum, [28]	100	0.1	131	2.67
Ferro-solutions, [28]	60	0.1	133	8.12
<b>OMC prototype</b>	58	0.1	18	<b>11.67</b>
<b>OMC prototype</b>	131	0.1	18	<b>12.67</b>
<b>VC prototype</b>	41	0.1	18	<b>5.39</b>
<b>VC prototype</b>	109	0.1	18	<b>11.11</b>

- 4) It was shown that it is possible to harvest energy from the impulse associated with the rapid-stop axis motion of a machine tool. The VC prototype was poorly suited for harvesting the small 0.4–1.0 g acceleration impulses associated with rapid axis motion, but demonstrated that it is possible. Lower resonant frequencies generated more energy for a rapid-stop event. While machining a test part, an average of 43 microjoules was generated for each rapid event to change tools or reposition. The low frequency and small magnitude acceleration impulses may make this a source better suited for a piezoelectric transducer because it will likely be difficult for an



electromagnetic transducer to get a large enough inertial mass velocity to generate voltages that can be easily rectified.

- 5) The experimental characterization of the OMC and VC prototypes showed that small unoptimized devices can harvest power on par with the average power requirements of commercial wireless sensor nodes for input accelerations and frequencies similar in magnitude to those associated with large motors and machine tool environments. During characterization on a vibration platform with a 0.1 g input acceleration amplitude, the OMC prototype produced 1.05 mW at 58 Hz and 1.14 mW at 131 Hz. For the same input parameters, the VC prototype produced 0.97 mW at 41 Hz and 2 mW at 109 Hz.
- 6) The prototype designs allowed the resonant frequency to be modified relatively quickly and easily by changing the planar springs. The OMC prototype was made to resonate at 58 Hz and 131 Hz while characterizing the device. The VC prototype was made to resonate at a number of frequencies between 8 Hz and 120 Hz while characterizing the device and running realistic evaluations on large motors and a machine tool. While changing the springs and matching a target frequency took perhaps ten minutes, leaving significant room for improvement, the devices were not locked into a single stiffness. Devices whose stiffness cannot be modified are limited to a small target frequency range because the resonant frequency can only be adjusted by changing the mass of the resonant system. While the prototypes were designed with a rather simplistic method for modifying their stiffness, their performances showed that a single transducer design could harvest from a large frequency range if its stiffness can be modified.
- 7) The higher output voltages across the load resistances of the OMC prototype make it more attractive than the VC prototype from a rectification standpoint because well over one volt was developed at both ends of the target frequency range. For an input acceleration amplitude of 0.1 g, the OMC prototype generated an RMS voltage of 2 V at 58 Hz and almost 3.2 V at 131 Hz. The output voltages from the VC prototype were consistently lower than a volt for both the characterization on the vibration platform and the more realistic application deployments on the large motors and machine tool. For a 0.1 g input acceleration amplitude on the vibration platform, the VC prototype generated an RMS voltage of 0.33 V at 41 Hz and 0.84 V at 109 Hz. The low output voltages indicate that a voltage constraint needs to be included in design analysis for these devices.
- 8) As a possible way of addressing the low output voltages from the VC prototype, the coreless DC motor- and Halbach array-inspired designs were proposed as possibly being capable of significantly higher gap flux densities. Initial analysis of the proposed designs with the same basic design constraints used to create the OMC and VC prototypes showed that average gap flux densities of 0.6–0.7 T and possibly higher were achievable, representing a possible 140% or more improvement over the 0.25 T gap flux density of the VC prototype. The initial

analysis suggests gap flux density could potentially approach the one tesla level that is common for most electromagnetic machines.

- 9) The performance evaluation of the two prototypes showed that the OMC design performs better at lower frequencies than the VC design. The power generated at the low end of the frequency range by the OMC prototype, 1.05 mW at 58 Hz for a 0.1 g input acceleration, was almost the same as for the high end of the frequency range, 1.14 mW at 131 Hz for a 0.1 g input acceleration. The consistent power performance across the frequency range may be explained by the intense zone of high flux density near the edge of the cylindrical magnet at the top and bottom surfaces. At lower frequencies, the distance travelled by the magnet is larger, causing the intense flux density region to interact with more of the coil and compensate for the lower magnet velocity. The performance trends of the coreless DC motor- and Halbach array-inspired designs would be like that of the VC prototype because the magnitude of the gap flux density would be independent of frequency, making them better suited for harvesting higher frequency vibration sources.
- 10) It was shown that reasonable power can be harvested from the unsprung suspension of a vehicle. Vehicle suspension acceleration data was simulated with a vibration platform. With a low resonant frequency of about 18 Hz, the VC prototype was able to harvest an average of 0.57 mW for speeds of 96 kph and higher on roads with rougher surfaces. However, on smoother roads, only an average of 0.05 mW was harvested for vehicle speeds of 96 kph and higher. Again the VC prototype was poorly suited for this vibration source, but it does show that it might be possible to power an asset tracking or monitoring system for tractor trailers or large equipment. The results suggested that rougher roads and likely lower profile tires would lead to higher harvested powers.
- 11) If it is assumed that all four architectures proposed in the device designs chapter will work for a given application, some high level conclusions can be drawn about choosing between the designs. The simplicity of the OMC design is compelling, and should be used if the mounting environment allows it. The added assembly complexity and use of multiple magnet sizes may make the Halbach array-inspired design unattractive when all the designs could satisfy the application requirements. One asset that could impact the architecture choice is the price of magnetic material. If rare earth materials became significantly more expensive than steel, the VC and coreless DC motor-inspired design may become more attractive than the OMC and Halbach array designs.

## Appendix A. Electromagnetics

---

### A.1. Maxwell's equations

Maxell's equations are a set of partial differential equations that govern all electromagnetic systems, and in full form, they are known as Ampere's law, Gauss' law, Gauss' law for magnetism, and Faraday's law [67]. Respectively, the macroscopic equations are as follows

$$\nabla \times \vec{H} = \vec{J} + \frac{\partial \vec{D}}{\partial t}, \quad (\text{A.1})$$

$$\nabla \cdot \vec{D} = \rho, \quad (\text{A.2})$$

$$\nabla \cdot \vec{B} = 0, \quad (\text{A.3})$$

$$\nabla \times \vec{E} = -\frac{\partial \vec{B}}{\partial t}, \quad (\text{A.4})$$

where  $\mathbf{H}$  represents the magnetic field intensity and  $\mathbf{J}$  current density.  $\mathbf{D}$  is the electric flux density, and  $\rho$  is the charge density.  $\mathbf{B}$  is magnetic flux density, and  $\mathbf{E}$  is the electric field intensity. The fields  $\mathbf{H}$ ,  $\mathbf{D}$ ,  $\mathbf{B}$ , and  $\mathbf{E}$  are all time varying as are  $\mathbf{J}$  and  $\rho$ . For magnetic devices, it's assumed that there are no external electric fields. Thus, Gauss' law, equation A.2 is eliminated, and the remaining set of equations simplify to

$$\nabla \times \vec{H} = \vec{J}, \quad (\text{A.5})$$

$$\nabla \cdot \vec{B} = 0, \quad (\text{A.6})$$

$$\nabla \times \vec{E} = -\frac{\partial \vec{B}}{\partial t}. \quad (\text{A.7})$$

The integral forms of Maxwell's equations are more useful than the differential forms when analyzing practical physical systems with defined geometry. By applying Stokes' theorem,

$$\int_s [\nabla \times \vec{A}] \cdot d\vec{a} = \oint_c \vec{A} \cdot d\vec{l}, \quad (\text{A.8})$$

and the divergence theorem,

$$\int_v [\nabla \cdot \vec{A}] \cdot dv = \oint_s \vec{A} \cdot d\vec{a}, \quad (\text{A.9})$$

the integral forms are obtained. Stokes' theorem states that the integral of the curl of vector  $\mathbf{A}$  over a given surface,  $s$ , equals the integral of vector  $\mathbf{A}$  over the loop,  $c$ , that encloses the area of  $s$ . The divergence theorem states that the integral of the divergence of vector  $\mathbf{A}$  over a volume,  $v$ , equals the integral of the vector  $\mathbf{A}$  over the surface,  $s$ , enclosing volume  $v$ .

Applying equation A.8 to equations A.5 and A.7 and applying equation A.9 to equation A.6 yields

$$\oint_c \vec{H} \cdot d\vec{l} = \int_s \vec{J} \cdot d\vec{a}, \quad (\text{A.10})$$

$$\oint_s \vec{B} \cdot d\vec{a} = 0 , \quad (\text{A.11})$$

$$\oint_c \vec{E} \cdot d\vec{l} = -\frac{\partial}{\partial t} \int_s \vec{B} \cdot d\vec{a} . \quad (\text{A.12})$$

Equations A.10–A.12 can now be used to analyze devices or systems with defined surfaces and path lengths. Section 1.6.1 starts with the above three integral forms of the relevant Maxwell’s equations for analyzing magnetic devices.

## Appendix B. Cored vibration harvester designs

As mentioned at the beginning of chapter four, cored magnetic circuit architectures were explored, and it was determined that they were unsuitable for harvesting the very small input accelerations associated with the vibration sources of interest. This section serves to summarize the findings from designing, building, and testing two cored variable reluctance devices. The full magnetic circuit analyses of the devices will not be presented since it is unnecessary for showing the challenges of harvesting vibrations with these types of device designs.

The idea behind a cored design is to have very short flux path lengths through air in an effort to minimize reluctance losses in order to maintain large magnitude magnetic fields. In the voice-coil type architectures, the flux concentration of the low reluctance iron circuit is somewhat undermined by the large air gap and associated reluctance loss.

The two cored designs that were explored were variable reluctance devices, meaning the relative motion between the halves of the magnetic circuit modified the reluctance of the flux path. The change in reluctance was due to the flux path length through air increasing or decreasing. The change in reluctance was the cause of the change in flux that could be exploited to generate a voltage.

The first design was a toothed variable reluctance device. When the teeth were aligned, the magnetic circuit was at its minimum reluctance, and as the relative motion forced the teeth out of alignment, the flux path length through air increased, causing a change in flux. Figure B.1 shows a picture of the toothed variable reluctance prototype. Overall the prototype was 5 x 5 x 9 cm, and the air gap length with the teeth aligned was 0.13–0.25 mm.

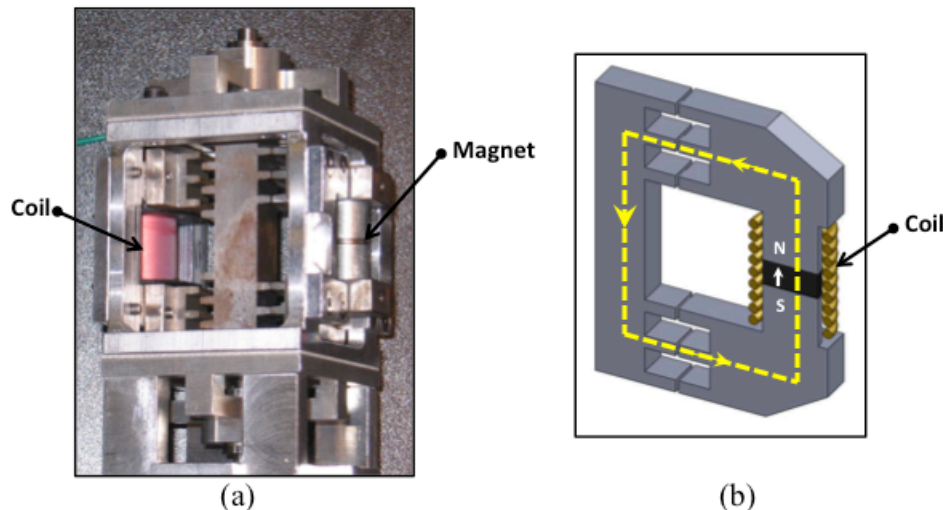


**Figure B.1.** (a) toothed variable reluctance prototype. (b) illustrated cross-section of the toothed variable reluctance magnetic circuit.

The second variable reluctance design attempted to get the flux to reverse direction in an effort to achieve a very large change in flux. The design used two oppositely oriented magnets. The magnet completing the magnetic circuit depended on the relative position of the two halves of the circuit. At the top of the translation amplitude, the bottom magnet completed the flux loop, and the top magnet short-circuited

as can be seen in figure B.2(b). Thus at the top of the translation amplitude the flux flow direction through the coil was positive, and at the bottom of the translation amplitude, the top magnet completed the flux loop, causing the flux direction to be negative. Figure B.2 shows the flux reversing variable reluctance design.

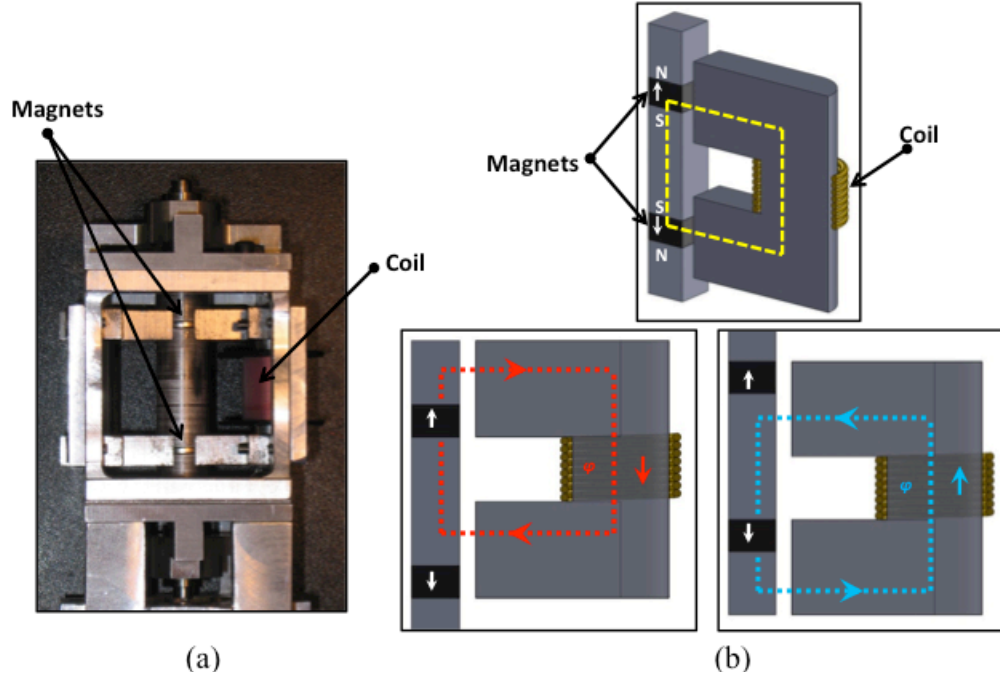


**Figure B.2.** (a) Flux reversing variable reluctance prototype. (b) illustrated cross-sections of the flux reversing design showing basic layout and reversing flux loops.

There were design oversights with the two devices. To minimize flux leakage paths and losses, the magnets should have been placed at the air gaps instead of being embedded in the circuits as they were. With cored devices, there are additional flux losses due to eddy currents and hysteresis. Since the core is also a conductive material voltages are induced in it as well as the coil according to Faraday's law. The voltages and associated currents induced in the core are dissipated as heat. Thin insulated laminations of core material can be used to minimize eddy current losses in one direction [38][37], but laminations were not used in the prototypes. Hysteresis losses are the result of the changing flux reorienting the magnetic domains of the core material. The design issues and additional losses contributed to the cored prototypes not being suitable for vibration harvesting but were secondary issues compared to the gap and cogging forces.

The very small air gaps in reluctance circuits enable high gap magnetic flux densities, but high flux densities cause a large attractive magnetic force trying to close the gap. The gap closing force can be approximated as

$$F = \frac{B^2 A}{2\mu_0}, \quad (\text{B.1})$$

where B is the gap magnetic flux density, and A is gap area normal to the flux path [38][37]. Equation B.1 assumes that the permeability of the material in the flux loop is linear. The in-plane stiffness of the spiral resonant springs was not high enough to counteract the high gap closing forces observed in the prototypes. As a result, the added

complexity of linear bearings was required to maintain the air gaps that enabled the relative motion and associated changes in flux. The need for the linear bearings severely limited how small the prototypes could be constructed.

Cogging forces were a second problematic force for cored designs. A cogging point occurs when the magnetic forces in the system are balanced. Cogging forces are the restoring forces that arise when a translation is imposed on the reluctance circuit, disrupting the balance. For the toothed variable reluctance design, the cog point was when the teeth were aligned. When the relative motion tried to misalign the teeth a restoring force opposing the motion arose. Similarly, for the flux reversing design, the cog point occurred when the magnets were centered in the air gaps as can be seen in figure B.2(a). The cogging forces were large enough to severely limit the relative motion for input accelerations up to 1 g.

With the toothed variable reluctance design, an effort was made to cancel the cogging forces with tooth shaping and phase shifted magnetic circuits. As can be seen in figure B.1(a), the teeth on the left side are misaligned and the teeth on the right side are aligned, so the two magnetic circuits are 180 degrees out of phase. Figure B.3 shows the cancelling effect of the phase shifted magnetic circuits. The peak cogging force was reduced by about 50% as a result of the phase shift.

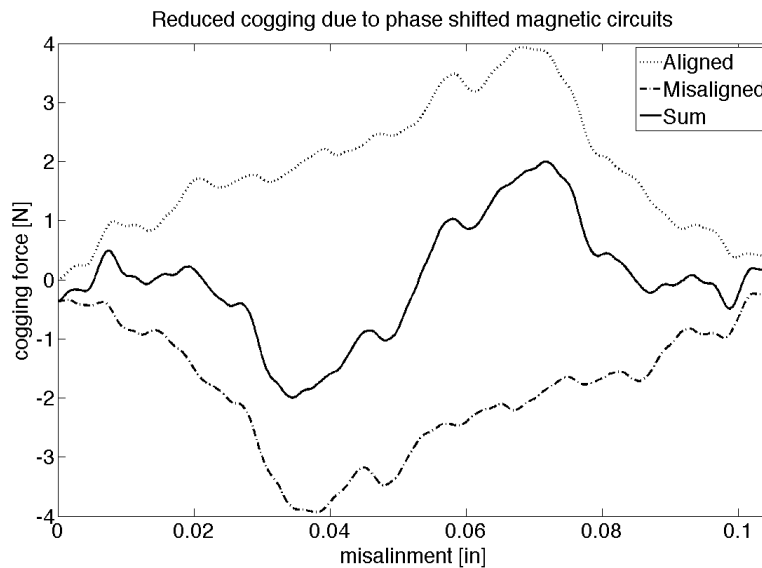


**Figure B.3.** Reduced cogging force due to phase shifted magnetic circuits. The force curves were measured using a dynamometer, and actuation was done with the z-axis of a CNC milling machine.

Tooth shaping was used to further reduce or cancel the cogging force. Adding a slight chamfer to the edges of the teeth resulted in greater cancelling because the chamfering shifted the peak of the cogging force curve to the center of the translation amplitude. The cogging force curve could have been further modified with more complex tooth shaping, but scaling and manufacturability concerns made further tooth shaping difficult.

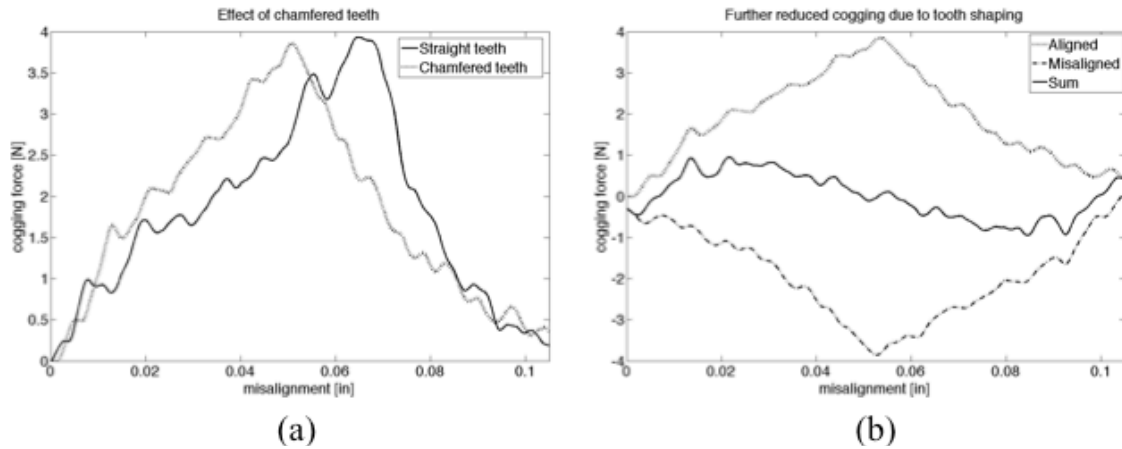


**Figure B.4.** (a) Shift in cogging force curve due to tooth shaping. (b) increased cancelling of the cogging forces as a result of the tooth shaping. The force curves were measured on a Kistler dynamometer.

The relative motion increased after implementing the phase shift and tooth shaping, but significant relative motion only occurred at higher input accelerations where the inertial force of the moving mass dominated the cogging forces.

The flux reversing design had even higher cogging forces, but the cogging force curves were symmetric and fairly linear.

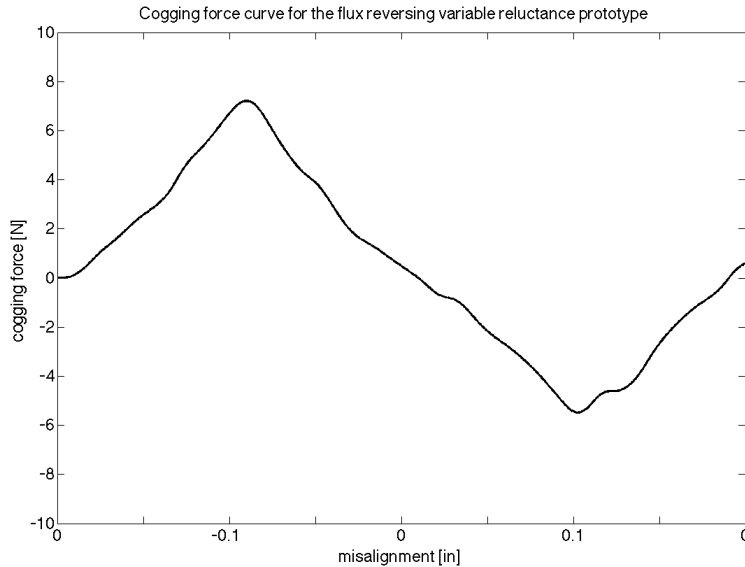


**Figure B.5.** Cogging force curve for the flux reversing variable reluctance design. The force curve was measured with a Kistler dynamometer.

Ultimately, it may be possible to cancel the cogging forces with phase shifts and geometric effects, but the complexity of the device would likely be high. The added complexity would likely impact the cost of the device and how small it can be made. Even if the cogging issues were eliminated the high gap forces would still require bearings, adding a parasitic loss to the resonant system that would reduce any relative motion.



Another approach would be to treat the cogging forces as spring forces. Cogging forces are a function of position [38], so it could be treated as an additional stiffness term in the equation of motion. Thus the cogging force would increase the resonant frequency of the system, and it would be reasonably easy to account for especially if the cogging force is linear like that for flux reversing prototype. The added stiffness would likely make it difficult to get low enough resonant frequencies to be useful for vibration harvesting. Efforts to build a viable cored harvester were abandoned before exploring the possibility of using cogging as additional stiffness.

In any event, several issues limit the attractiveness of cored designs. The first issue is the overall complexity of the system especially given the high gap forces requiring the use of bearings. The second issue is the cogging forces. Attempting to cancel the cogging forces increases the complexity of the devices, and treating the cogging as additional stiffness increases the resonant frequency of the device. It may also become difficult to account for the added stiffness from cogging if the cogging force curve is nonlinear. The last issue is that the attractiveness of a cored device is the possibility to have high magnetic flux densities that might approach one tesla, but section 4.5 shows that high gap flux densities are possible for simple voice-coil type architectures that do not have cogging, bearing, eddy current, or hysteresis problems.

## References

---

- [1] *geaviation.com*, *geaviation.com*. [Online]. Available: <http://www.geaviation.com>. [Accessed: 03-Nov.-2011].
- [2] Derby, "Manufacturing: A tale of two industries | The Economist," *economist.com*, 30-Jul.-2011. [Online]. Available: <http://www.economist.com/node/21524937>. [Accessed: 02-Nov.-2011].
- [3] J. Kahn, R. Katz, and K. Pister, "Next Century Challenges: Mobile Networking for 'Smart Dust'," 1999.
- [4] B. Warneke, M. Last, B. Liebowitz, and K. S. J. Pister, "Smart Dust: communicating with a cubic-millimeter computer," *Computer*, vol. 34, no. 1, pp. 44–51, 2001.
- [5] J. Hill and D. Culler, "MICA: A wireless platform for deeply embedded networks," *Ieee Micro*, vol. 22, no. 6, pp. 12–24, 2002.
- [6] B. Warneke, "Exploring the limits of system integration with smart dust," ... *Congress & Exposition*, 2002.
- [7] Y. H. Chee et al., "PicoCube: A 1cm<sup>3</sup> sensor node powered by harvested energy," in *Design Automation Conference, 2008. DAC 2008. 45th ACM/IEEE*, 2008, pp. 114–119.
- [8] *Data sheet for SmartmeshIP DN6000/M600x*, *Data sheet for SmartmeshIP DN6000/M600x*. [Online]. Available: [http://www.dustnetworks.com/products/list/?field\\_product\\_type\\_value\\_many\\_to\\_one=Mote-on-Chip](http://www.dustnetworks.com/products/list/?field_product_type_value_many_to_one=Mote-on-Chip). [Accessed: 25-Oct.-2011].
- [9] W. Dargie and C. Poellabauer, *Fundamentals of Wireless Sensor Networks: Theory and Practice*. Singapore: John Wiley & Sons Ltd., 2010.
- [10] *Data sheet for LIS3L02As4 MEMS inertial sensor*, *Data sheet for LIS3L02As4 MEMS inertial sensor*. [Online]. Available: [http://www.st.com/internet/com/TECHNICAL\\_RESOURCES/TECHNICAL\\_LITERATURE/DATASHEET/CD00005153.pdf](http://www.st.com/internet/com/TECHNICAL_RESOURCES/TECHNICAL_LITERATURE/DATASHEET/CD00005153.pdf). [Accessed: 25-Oct.-2011].
- [11] K. Pister, "Smart dust-hardware limits to wireless sensor networks," in *Distributed Computing Systems, 2003. Proceedings. 23rd International Conference on*, 2003.
- [12] C. S. Raghavendra, K. M. Sivalingam, and T. Znati, Eds. *Wireless Sensor Networks*. New York: Springer, 2004.
- [13] M. Green, *Solar cells: operating principles, technology and system applications*. Engleod Cliffs, NJ: Prentice-Hall, 1982, p. 274.
- [14] R. Vyas, V. Lakafosis, and M. Tentzeris, "Wireless Remote Localization System utilizing Ambient RF/Solar Power Scavenging RFID Tags," in *2010 IEEE/MTT-S International Microwave Symposium - MTT 2010*, 2010, pp. 1764–1767.
- [15] D. Carli, D. Brunelli, D. Bertozzi, and L. Benini, "A high-efficiency wind-flow energy harvester using micro turbine," *Power Electronics Electrical Drives Automation and Motion (SPEEDAM), 2010 International Symposium on*, pp. 778–783, 2010.
- [16] A. Bansal, D. A. Howey, and A. S. Holmes, "CM-scale air turbine and generator for energy harvesting from low-speed flows," in *Solid-State Sensors, Actuators and Microsystems Conference, 2009. TRANSDUCERS 2009. International*, 2009, pp. 529–532.
- [17] S. Priya, "Modeling of electric energy harvesting using piezoelectric windmill," *Applied Physics Letters*, vol. 87, no. 18, p. 184101, 2005.
- [18] M. Sanchez-Sanz, B. Fernandez, and A. Velazquez, "Energy-Harvesting Microresonator Based on the Forces Generated by the Karman Street Around a Rectangular Prism," *Journal of Microelectromechanical Systems*, vol. 18, no. 2, pp. 449–457, 2009.
- [19] R. Venkatasubramanian, C. Watkins, D. Stokes, J. Posthill, and C. Caylor, "Energy Harvesting for Electronics with Thermoelectric Devices using Nanoscale Materials,"

- Electron Devices Meeting, 2007. IEDM 2007. IEEE International*, pp. 367–370, 2007.
- [20] S. Dalola et al., “Autonomous Sensor System With Power Harvesting for Telemetric Temperature Measurements of Pipes,” *Instrumentation and Measurement, IEEE Transactions on*, vol. 58, no. 5, pp. 1471–1478, 2009.
- [21] V. Jovanovic, “Design, Fabrication and Testing of Energy-Harvesting Thermoelectric Generator,” in *Smart Structures and Materials 2006: Smart Structures and Integrated Systems*, 2006, vol. 6173, no. 1, pp. 61730G–61730G–8.
- [22] H. Nishimoto, Y. Kawahara, and T. Asami, “Prototype implementation of ambient RF energy harvesting wireless sensor networks,” *Sensors, 2010 IEEE*, pp. 1282–1287, 2010.
- [23] M. Arrawatia, M. S. Baghini, and G. Kumar, “RF energy harvesting system from cell towers in 900MHz band,” in *Communications (NCC), 2011 National Conference on*, 2011, pp. 1–5.
- [24] R. Vyas, V. Lakafosis, M. Tentzeris, H. Nishimoto, and Y. Kawahara, “A Battery-less, Wireless Mote for Scavenging Wireless Power at UHF (470-570 MHz) Frequencies,” in *2011 IEEE Antennas and Propagation Society International Symposium and USNC/URSI National Radio Science Meeting*, 2011, pp. 1069–1072.
- [25] M. Mark et al., “A 1mm<sup>3</sup> 2Mbps 330fJ/b transponder for implanted neural sensors,” *2011 Symposium on VLSI circuits digest of technical papers*, pp. 168–169, 2011.
- [26] C. B. Williams and R. B. Yates, “Analysis Of A Micro-electric Generator For Microsystems,” in *Solid-State Sensors and Actuators, 1995 and Eurosensors IX. Transducers '95. The 8th International Conference on*, 1995, vol. 1, pp. 369–372.
- [27] S. Roundy, *Energy scavenging for wireless sensor nodes with a focus on vibration to electricity conversion*, University of California, Berkeley, 2003.
- [28] P. D. Mitcheson, E. M. Yeatman, G. K. Rao, A. S. Holmes, and T. C. Green, “Energy Harvesting From Human and Machine Motion for Wireless Electronic Devices,” *Proceedings of the IEEE*, vol. 96, no. 9, pp. 1457–1486, 2008.
- [29] Z. Hadas, M. Kluge, V. Singule, and C. Ondrusek, “Electromagnetic Vibration Power Generator,” *Diagnostics for Electric Machines, Power Electronics and Drives, 2007. SDEMPED 2007. IEEE International Symposium on*, pp. 451–455, 2007.
- [30] K. Vijayaraghavan and R. Rajamani, “Novel Batteryless Wireless Sensor for Traffic-Flow Measurement,” *Vehicular Technology, IEEE Transactions on*, vol. 59, no. 7, pp. 3249–3260, 2010.
- [31] D. J. Inman, *Engineering vibration*, 2nd ed. Englewood Cliffs, NJ: books.google.com, p. 560.
- [32] S. Meninger, J. O. Mur-Miranda, R. Amirtharajah, A. Chandrakasan, and J. H. Lang, “Vibration-to-electric energy conversion,” *IEEE Transactions on Very Large Scale Integration (VLSI) Systems*, vol. 9, no. 1, pp. 64–76, 2001.
- [33] R. Tashiro, N. Kabei, K. Katayama, E. Tsuboi, and K. Tsuchiya, “Development of an electrostatic generator for a cardiac pacemaker that harnesses the ventricular wall motion,” *Journal of Artificial Organs*, vol. 5, no. 4, pp. 239–245, Dec. 2002.
- [34] P. Miao, P. D. Mitcheson, A. S. Holmes, E. M. Yeatman, T. C. Green, and B. H. Stark, “Mems inertial power generators for biomedical applications,” *Microsystem Technologies*, vol. 12, no. 10, pp. 1079–1083, Apr. 2006.
- [35] T. Sterken, P. Fiorini, G. Altena, C. Van Hoof, and R. Puers, “Harvesting Energy from Vibrations by a Micromachined Electret Generator,” in *Solid-State Sensors, Actuators and Microsystems Conference, 2007. TRANSDUCERS 2007. International*, 2007, pp. 129–132.
- [36] M. Edamoto et al., “Low-Resonant-Frequency Micro Electret Generator for Energy Harvesting Application,” in *Micro Electro Mechanical Systems, 2009. MEMS 2009. IEEE 22nd International Conference on*, 2009, pp. 1059–1062.
- [37] H-D. Chai, *Electromechanical motion devices*. Upper Saddle River, NJ: Prentice Hall

- PTR, 1998.
- [38] D. K. Lieu, *ME 229: Design of basic electro-mechanical devices*. Berkeley, CA.; 2005.
  - [39] E. Leland, "Resonance tuning of piezoelectric vibration energy scavenging generators using compressive axial preload," *Smart Materials and Structures*, 2006.
  - [40] I. Sari, T. Balkan, and H. Kulah, "An electromagnetic micro power generator for wideband environmental vibrations," *Sensors and Actuators A: Physical*, vol. 145, pp. 405–413, Jul. 2008.
  - [41] V. R. Challa, M. G. Prasad, Y. Shi, and F. T. Fisher, "A vibration energy harvesting device with bidirectional resonance frequency tunability," *Smart Materials and Structures*, vol. 17, no. 1, p. 015035, Jan. 2008.
  - [42] B. Marinkovic and H. Koser, "Smart Sand—a wide bandwidth vibration energy harvesting platform," *Applied Physics Letters*, vol. 94, no. 10, pp. 103505–103505, 2009.
  - [43] M. Marzencki, M. Defosseux, and S. Basrour, "MEMS Vibration Energy Harvesting Devices With Passive Resonance Frequency Adaptation Capability," *Microelectromechanical Systems, Journal of*, vol. 18, no. 6, pp. 1444–1453, 2009.
  - [44] S. D. Nguyen and E. Halvorsen, "Nonlinear Springs for Bandwidth-Tolerant Vibration Energy Harvesting," *Microelectromechanical Systems, Journal of*, no. 99, pp. 1–3, 2011.
  - [45] S. P. Beeby, M. J. Tudor, and N. M. White, "Energy harvesting vibration sources for microsystems applications," *Measurement Science and Technology*, vol. 17, no. 12, pp. R175–R195, Oct. 2006.
  - [46] D. P. Arnold, "Review of Microscale Magnetic Power Generation," *IEEE Transactions on Magnetics*, vol. 43, no. 11, pp. 3940–3951, 2007.
  - [47] R. Amiritharajah and A. P. Chandrakasan, "Self-powered signal processing using vibration-based power generation," *Solid-State Circuits, IEEE Journal of*, vol. 33, no. 5, pp. 687–695, 1998.
  - [48] J. M. H. Lee, S. C. L. Yuen, W. J. Li, and P. H. W. Leong, "Development of an AA size energy transducer with micro resonators," in *Circuits and Systems, 2003. ISCAS '03. Proceedings of the 2003 International Symposium on*, 2003, vol. 4.
  - [49] R. Waters, B. Chisum, and H. Jazo, "Development of an electro-magnetic transducer for energy harvesting of kinetic energy and its' applicability to a MEMS-scale device," *Proc nanoPower ...*, 2008.
  - [50] E. Dallago, M. Marchesi, and G. Venchi, "Analytical Model of a Vibrating Electromagnetic Harvester Considering Nonlinear Effects," *IEEE Transactions on Power Electronics*, vol. 25, no. 8, pp. 1989–1997, Aug. 2010.
  - [51] M. El-hami et al., "Design and fabrication of a new vibration-based electromechanical power generator," in *Sensors and Actuators a-Physical*, 2001, vol. 92, pp. 335–342.
  - [52] S. P. Beeby, M. J. Tudor, R. N. Torah, S. Roberts, T. O'Donnell, and S. Roy, "Experimental comparison of macro and micro scale electromagnetic vibration powered generators," *Microsystem Technologies*, vol. 13, no. 11, pp. 1647–1653, Jan. 2007.
  - [53] P. GlynneJones, "An electromagnetic, vibration-powered generator for intelligent sensor systems," *Sensors and Actuators A: Physical*, vol. 110, no. 1, pp. 344–349, Feb. 2004.
  - [54] C. R. Saha, T. O'Donnell, H. Loder, S. Beeby, and J. Tudor, "Optimization of an Electromagnetic Energy Harvesting Device," *IEEE Transactions on Magnetics*, vol. 42, no. 10, pp. 3509–3511, Oct. 2006.
  - [55] S. P. Beeby et al., "Design and performance of a microelectromagnetic vibration powered generator," in *Solid-State Sensors, Actuators and Microsystems, 2005. Digest of Technical Papers. TRANSDUCERS '05. The 13th International Conference on*, 2005, vol. 1, pp. 780–783.
  - [56] H. Nagaoka, "The inductance coefficients of solenoids," *J Coll Sci*, 1909.
  - [57] H. A. Wheeler, "Simple Inductance Formulas for Radio Coils," in *Proceedings of the*

- Institute of Radio Engineers*, 1928, vol. 16, no. 10, pp. 1398–1400.
- [58] G. K. Fedder, *Simulation of Microelectromechanical systems*, Berkeley, CA: University of California, Berkeley, 1994.
  - [59] M. D. Seeman, S. R. Sanders, and J. M. Rabaey, “An Ultra-Low-Power Power Management IC for Wireless Sensor Nodes,” in *Custom Integrated Circuits Conference, 2007. CICC '07. IEEE*, 2007, pp. 567–570.
  - [60] M. D. Seeman, S. R. Sanders, and J. M. Rabaey, “An ultra-low-power power management IC for energy-scavenged Wireless Sensor Nodes,” in *Power Electronics Specialists Conference, 2008. PESC 2008. IEEE*, 2008, pp. 925–931.
  - [61] P. Glynne-Jones, “An electromagnetic, vibration-powered generator for intelligent sensor systems,” *Sensors and Actuators A: Physical*, vol. 110, no. 1, pp. 344–349, Feb. 2004.
  - [62] S. P. Beeby et al., “A micro electromagnetic generator for vibration energy harvesting,” *Journal of Micromechanics and Microengineering*, vol. 17, no. 7, pp. 1257–1265, Jun. 2007.
  - [63] A. Hajati and S.-G. Kim, “Ultra-wide bandwidth piezoelectric energy harvesting,” *Applied Physics Letters*, vol. 99, no. 8, p. 083105, 2011.
  - [64] M. S. M. Soliman, E. M. Abdel-Rahman, E. F. El-Saadany, and R. R. Mansour, “A wideband vibration-based energy harvester,” *Journal of Micromechanics and Microengineering*, vol. 18, no. 11, p. 115021, Oct. 2008.
  - [65] L. M. Miller, E. Halvorsen, T. Dong, and P. K. Wright, “Modeling and experimental verification of low-frequency MEMS energy harvesting from ambient vibrations,” *Journal of Micromechanics and Microengineering*, vol. 21, no. 4, pp. –, 2011.
  - [66] E. M. Trent and P. K. Wright, *Metal Cutting*, Fourth. Boston: Butterworth-Heinemann, 2000, p. 446.
  - [67] R. S. Elliott, *Electromagnetics: History, Theory, and Applications*. New York: John Wiley & Sons, 1999, p. 660.